Design of a Microgrid for Bukunor Water Treatment Plant

Control Design and Simulation of Grid-Following Inverters in a Renewable Microgrid

Marcel Hass, Rajarshi Mukherjee, Nika Juričić, Morgan Bigej, Kofi Appiah-Nkansah and Yuvraj Upadhyay

HWPS1-750, December 2025

1. Semester Master Project

AALBORG UNIVERSITY

STUDENT REPORT

AAU Energy
Aalborg University
Aalborg
Pontoppidanstræde 105, 9220 Aalborg Øst
http://www.energi.aau.dk/

Title:
Design of Microgrid for B-WTP

Theme:
Dynamics in Electrical Energy Engineering

Project Period:
1. Semester Master

Project Group:
HWPS1-750

Participant(s):
Marcel Hass
Rajarshi Mukherjee
Nika Juričić
Morgan Bigej
Kofi Appiah-Nkansah
Yuvraj Upadhyay

Supervisor(s):
Tamas Kerekes

Copies: 1

Page Numbers: 101

Date of Completion:
19. December 2025

Abstract:

Microgrids rely on power electronic converters to integrate renewable energy sources in a controlled and reliable way. This project focuses on the design and evaluation of grid-following inverters for a microgrid comprising wind power, photovoltaic generation, and battery energy storage.

An energy-based model of the microgrid is developed to describe the interaction between generation units, storage, and the load. Based on this model, grid-following control structures for the wind and solar inverters are implemented in MATLAB/Simulink and assessed through simulation. The evaluation focuses on active power reference tracking, current control behavior, and power quality, with particular emphasis on current reference tracking and harmonic distortion.

The results show that the inverters can track their power references with stable dynamics and low steady-state error. The injected currents remain balanced and close to sinusoidal, with total harmonic distortion within commonly accepted limits. A limited set of HIL tests is included to provide initial insight into practical implementation aspects.

Preface

This Master's project was carried out during the autumn semester of 2025 as part of the first semester of the Master's at Aalborg University.

We want to thank our supervisor, Tamas Kerekes, for valuable guidance and constructive feedback throughout the project period.

All parts of the report have been prepared jointly and collaboratively, unless otherwise stated. The text has been linguistically polished using the software tool Grammarly to improve clarity and readability. No automated tools have been used to generate technical content, analyses, or results.

Aalborg, December 2025

Marcel Hass	Rajarshi Mukherjee	Nika Juričić
Morgan Bigej	Kofi Appiah-Nkansah	Yuvraj Upadhyay

Abbreviations

Abbreviation	Explanation
AC	Alternating Current
BESS	Battery Energy Storage System
B-WTP	Bukunor Water Treatment Plant
CAPEX	Capital Expenditure
DC	Direct Current
DER	Distributed Energy Resource
ECG	Electricity Company of Ghana
ESS	Energy Storage Systems
GFL	Grid-following
GRIDCo	Ghana Grid Company
HIL	Hardware-in-the-Loop
IEA	International Energy Agency
IEC	International Electrotechnical Commission
IGBT	Insulated Gate Bipolar Transistor
LA	Lightning Surge Arrestor
LCL	Inductor-Capacitor-Inductor
OPEX	Operational Expenditure
PCC	Point of Common Coupling
PFD	Phase/Frequency Detector
PI	Proportional Integral
PLC	Programmable Logic Controller
PLL	Phase-Locked Loop
PQ	Power Quality
PV	Photovoltaic
PWM	Pulse-Width Modulation
RES	Renewable Energy Source
SOC	State of Charge
SPWM	Sinusoidal Pulse Width Modulation
VFD	Variable Frequency Drive
VCO	Voltage Controlled Oscillator
VSC	Voltage Source Converter
VSI	Voltage Source Inverter
WAPCo	West African Pipeline Company
WT	Wind Turbine

Nomenclature

Symbol	**Explanation**	**Unit**
A	Area	m^2
C	Capacitance	F
f	Frequency	Hz
G	Solar irradiation	W/m^2
L	Inductance	H
P	Active Power	W
R	Resistance	Ω
T	Temperature	°C
V	Voltage	V
ρ	Air Density	kg/m^3

Contents

1 Introduction

The global energy sector is transitioning toward sustainable, low-carbon, and reliable power systems. Driven by growing concerns about climate change, resource depletion, and energy security, nations worldwide are transitioning from fossil-fuel-based generation to renewable energy systems that integrate solar, wind, and energy storage technologies. These systems not only reduce greenhouse gas emissions but also enhance power reliability and flexibility. This is becoming increasingly critical for essential infrastructure and modern societies. The lessons and technologies emerging from this global shift form the foundation for similar transitions in developing economies such as Ghana.

Despite significant progress in expanding its generation capacity, Ghana continues to face challenges of power reliability and cost. The country's dependence on hydrothermal generation and grid-based distribution has exposed critical infrastructure to unstable voltage profiles and frequent supply interruptions.

A significant challenge within Ghana's energy sector is the imbalance between limited power generation and the growing dependence on electricity-driven infrastructure, including factories, water treatment facilities, and urban services. This imbalance has resulted in frequent power outages, voltage fluctuations, and rising energy costs, all of which threaten the continuous operation and reliability of essential facilities and services. For critical installations such as water treatment plants (WTPs), where uninterrupted power is vital to sustaining water supply and quality, these energy challenges directly translate into operational inefficiencies, increased maintenance costs, and reduced service reliability.

The Bukunor Water Treatment Plant (B-WTP) is one of these facilities that continues to experience disruptions due to unstable grid supply and high energy costs. The plant's sole dependence on the national grid exposes it to frequent power outages and poor power quality, characterized by large voltage fluctuations and recurring frequency drops.

In 2024, B-WTP experienced 764,84 hours of power outages, of which the unreliable grid caused 576,69 hours. Figure 1.1 shows the breakdown of the causes of B-WTP power interruptions.

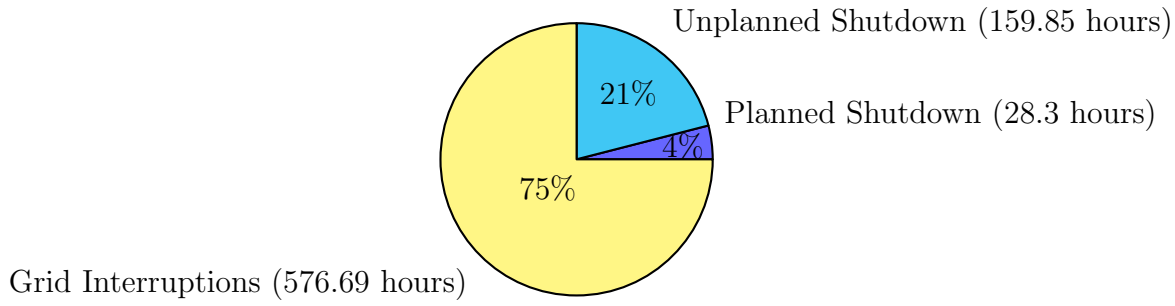

Figure 1.1. Breakdown of total no-production hours at the B-WTP, showing contributions from the grid interruptions, planned shutdowns, and unplanned shutdowns.

The use of diesel generators as a backup could reduce such interruptions. However, the high and unstable cost of fossil fuels results in significantly higher operational expenses, increased emissions, and accelerated equipment degradation. This situation reflects a larger national challenge of maintaining energy reliability and sustainability for critical infrastructure within an increasingly constrained and evolving power system.

To address these challenges, this project investigates the **design and implementation of grid following inverters to form a microgrid** that integrates **photovoltaic (PV) generation**, **a wind turbine (WT) system**, and **a battery energy storage system (BESS)** as a backup. The proposed system aims to provide a reliable and cost-effective energy supply to the B-WTP while reducing dependence on the national grid and simultaneously minimizing carbon emissions. The hybrid configuration leverages the complementary advantages of renewable and conventional sources; PV provides the primary energy during daylight hours, the WT contributes additional power generation, particularly at night, and the BESS smooths fluctuations and maintains energy balance.

Central to the project is the development of an energy management system (EMS) capable of coordinating power flow among the different subsystems. Given the variability of solar irradiance, wind speed, plant load, and battery state of charge (SOC), an optimized control framework is required to maintain power balance, efficiency, and system longevity. To achieve this, a control strategy is implemented in MATLAB/Simulink.

Simulation studies are conducted under varying solar, wind, and load conditions to evaluate system performance with respect to power reliability, renewable energy utilization, and operational efficiency. The design also accounts for modularity and compatibility with hardware-in-the-loop (HIL) testing on the real-time dSPACE controller and PLECS RT Box, enabling experimental validation and practical deployment.

Overall, this project aims to develop a flexible, and scalable microgrid adjusted to the operational requirements of the B-WTP. The results are expected to support Ghana Water Limited's broader efforts to ensure energy-secure and sustainable water supply while contributing to Ghana's national transition toward resilient, low-carbon power systems.

1.1 Problem Analysis

1.1.1 Global and Local Energy Context

The Global Imperative for Sustainable and Resilient Power Systems

The 21st century is characterized by accelerating global electricity demand, driven largely by industrial development, population growth, and digital advances. This significant increase is projected to continue, with the International Energy Agency (IEA) estimating that global electricity demand will rise by an average of 4% per year through 2027. This increasing consumption puts significant pressure on existing power infrastructure.[1]

Simultaneously, the global climate crisis demands a transition to Renewable Energy Sources (RES), such as solar and wind. This shift introduces grid challenges because the natural inconsistency of RES can cause voltage instability and frequency fluctuations if sufficient grid inertia and balancing mechanisms are not properly integrated. The challenge involves two main aspects: increasing capacity sustainably and improving grid resilience, defined as the ability to predict, endure, and rapidly recover from different disturbances. To achieve this, countries are focusing on grid modernization, investing in energy storage, microgrids, Distributed Energy Resources (DERs), and implementing innovative control strategies.

The African and Ghanaian Energy Landscape: A Crisis of Reliability

Sub-Saharan Africa (SSA) faces critical challenges regarding electricity reliability. Ghana has achieved a high level of electricity access, estimated by the World Bank at about 89.5% in 2023. Currently, 600 million people in SSA still lack access to electricity entirely, and those who are connected often face terrible unreliability. The power sector faces common issues, including aging infrastructure, underinvestment, inadequate maintenance, high technical and commercial losses, and governance challenges. These factors led to Ghana's severe 2012–2016 power crisis, known locally as "Dumsor" ("on and off"), and, despite some mitigation, the national grid remains weak.[2, 3]

The instability of the Ghanaian grid is marked by frequent blackouts (both scheduled load-shedding and unscheduled outages) and significantly poor power quality, including voltage sags (brownouts) and temporary faults. This instability is often more disruptive to critical infrastructure than total blackouts, as sensitive industrial equipment, such as Programmable Logic Controllers (PLCs) and Variable Frequency Drives (VFDs) are highly sensitive to malfunction or damage under low-voltage conditions. There are also fluctuations in hydropower generation due to rainfall imbalances and fuel-supply

irregularities in thermal plants. This unreliable supply severely affects critical facilities such as WTPs, which require a continuous, high-quality electrical supply.

1.1.2 Overview of Ghana's Power Production

Ghana's electricity supply system is dominated by hydroelectric and thermal plants, with a marginal share from renewable energy. According to the Energy Commission of Ghana, the total electricity generation in 2023 was (24.264 GWh), with the following breakdown: Thermal Plants (14.930 GWh), hydropower plants (9.187 GWh) and other renewables (148 GWh) [4]. Figure 1.2 shows the distribution of these power sources.

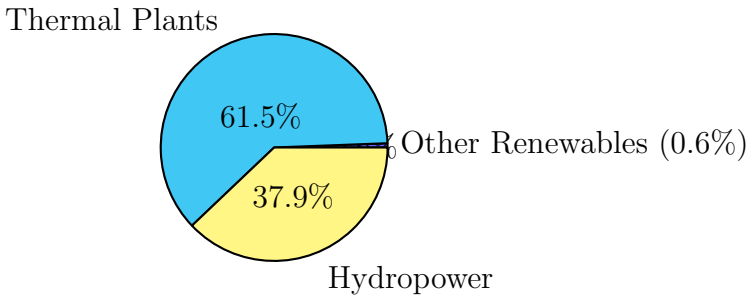

Figure 1.2. Breakdown of Ghana Power Production Sources

Installed generation capacity stood at 5.639 MW, of which 69,6% was thermal, 28,1% hydro, and 2,3% renewables. This reflects a system that is highly reliant on imported fuels and vulnerable to global price fluctuations, hydrological variability, and fuel supply disruptions.

Electricity Consumption Patterns

Electricity consumption has grown steadily, reaching 18.849 GWh in 2023. The sectoral distribution highlights the dominance of industrial and residential demand: industry 8.250 GWh (43,8%), residential 7.479 GWh (39,7%), services 3.069 GWh (16,3%), and agriculture/transport contributing less than 1% [4]. Figure 1.3 illustrates the electricity consumption.

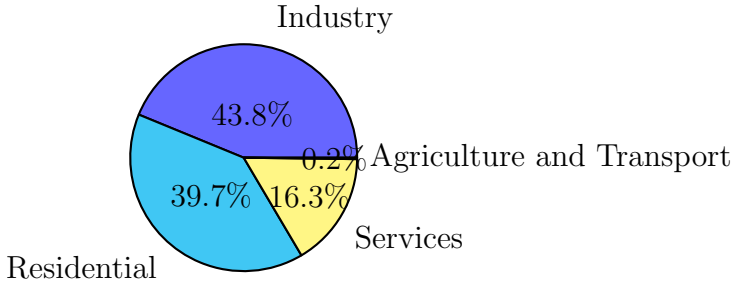

Figure 1.3. Breakdown of Ghana Electrical Consumption

This structure reveals two important features of Ghana's power economy:

- The industrial sector remains the largest consumer, reflecting the country's reliance on mining, manufacturing, and heavy industries whose operations are energy-intensive. Any disruptions in power supply, therefore, have immediate consequences for industrial productivity.
- The residential sector, on the other hand, accounts for nearly as much as industry, driven by rising household connectivity and population growth. This makes the grid highly sensitive to residential peak demand, particularly in the Regional capitals.

The combined dominance of residential and industrial consumption, which accounts for more than 80% of total demand, places enormous stress on the existing generation and distribution infrastructure and increases the risks posed by recurring deficits and system losses.

Reliability Challenges

Despite theoretical installed capacity exceeding domestic peak demand (3.171 MW in 2023), Ghana continues to face power shortages and outages. Several factors account for this, including:

- Fuel constraints: dependence on natural gas and oil leads to frequent supply bottlenecks [5].
- Hydrological risk: output from the dams in Akosombo, Kpong, and Bui fluctuates with rainfall [4].
- Technical and commercial losses: Transmission losses stood at 3,9% (908 GWh) in 2023, while distribution and commercial losses remain as high as 27–31% [4].
- Revenue recovery issues: payment arrears and debt between utilities and independent power producers (IPPs) weaken system liquidity [6]. The combined effect is an unreliable grid, marked by deficits of 500–700 MW in 2024 and recurring load shedding or "Dumsor" [7], [8]

1.1.3 The Case of B-WTP and Challenges for Critical Infrastructure

The Case of B-WTP

The operational difficulties at the B-WTP serve as a representative example of the systemic failures rooted within Ghana's unstable power grid. As a critical component of the public water supply infrastructure, B-WTP relies heavily on stable electrical power

for processes such as raw water pumping (intake), chemical dosing, filtration, final water pumping, and automated control systems.

According to internal reports, B-WTP experiences significant operational downtime due to power supply issues, categorized into two main problems:

1. Complete Blackouts: Unscheduled grid failures result in immediate and total shutdowns of treatment processes. This stops clean water production and creates operational risks. After the blackout, restarting the plant is time-consuming, leading to service delays and disturbances.
2. Under voltage (Brownout) Conditions: The conditions damage high-power motors and sensitive equipment such as PLCs and VFDs. Low voltage forces these motors to draw excessive current, leading to overheating and triggering protective relays that cause a production pause without a blackout. This repeated stress shortens the critical component's lifespan and increases maintenance costs.

The consequence of these disruptions is a significant reduction in B-WTP's ability to meet its mandate, resulting in irregular water supply, potential public health risks, and financial losses for Ghana Water Limited (GWL). The case of B-WTP highlights the mismatch between the plant's requirement for steady, clean, continuous power and the grid's irregular, fluctuating, and poor-quality supply[9].

Scarcity of Available Power

This is an operational reality in which the upstream grid is frequently curtailed, and power quality is poor, with wide blackouts and recurring frequency dips. Under these conditions, the B-WTP and the town's critical services do not operate at full capacity due to the unreliability of the national grid. There is a need for a stable, high-quality electrical power supply to the motors, drives, and controls for the sustained operation of the B-WTP, which will directly correlate with the supply of potable water to the Koforidua township.

Ghana's transmission system has experienced region-scale interruptions in recent years, outlined below:

- GRIDCo reported disturbances on February 7, 2024 (autotransformer trip at Kintampo; restoration by 07:35) [10, 11].
- GRIDCo also reported disturbances on March 3, 2024 (Mallam substation fault; staged restoration the next evening) [10, 11].
- Supply constraints originated upstream in generation on June 13, 2024, where GRIDCo and ECG jointly warned of load management due to reduced gas supply

from Nigeria via WAPCo [12].
- Sector diagnostics confirmed that "installed capacity" does not equate to available capacity: ACEP's 2024 review showed Ghana faced availability deficits of 120-312 MW in most months of 2022, validating the weak-grid assumption [13].

1.1.4 The WTP electrical infrastructure at risk

A conventional surface WTP for a large town typically includes: intake and high-lift pumps (MV/LV induction motors, often on VFDs); mixers and blowers; chemical dosing equipment (diaphragm pumps); clarifier drives; backwash pumps and air-scour blowers; distribution pumps; and the control layer. Each class is electrically sensitive in different ways: motors to sags/unbalance, VFDs to DC-bus dips/swells, and PLCs/analyzers to short interruptions and surges [14, 15, 16, 17].

Equipment Damage and Downtime from Reduced Power Quality

There are many effects of poor electrical quality on electromechanical equipment. From the conversion into thermal, dielectric and mechanical stresses, shortening equipment life, and multiple restarts, which in a treatment process manifests as hours of recovery even if the grid comes back in minutes. This is further explained below;

- **Voltage sags (70–90% V for 0.1–3 s):** Induction motor torque collapses beyond a certain voltage dip as the torque produced is directly proportional to the square of supplied voltage at terminals, which drives high input current to maintain torque. This results in heating, stalling, chatter/arc at the contractor's site, and accelerated insulation aging. VFDs trip on under-voltage, stressing electrolytic capacitors; PLCs are sometimes affected and reset without UPS ride-through.[14, 15, 16, 17].
- **Frequency dips (<49 Hz):** The distortion of V/Hz ratio leads to transformer over-flux and motor heating. The pump curves shift toward lower head, increasing the risk of cavitation. Timing-critical sequences (mix/floc/backwash) drift, especially during gas-supply driven load management windows[18, 19, 20].
- **Voltage imbalance (e.g., 2–3%):** Negative-sequence currents caused by voltage unbalance lead to increased rotor losses and heating in three-phase induction motors, requiring motor derating in accordance with IEC 60034-26 and IEC 60034-1 to ensure safe thermal operation. Voltage unbalance also increases DC-link ripple and thermal stress in Variable Frequency Drives (VFDs), as addressed in the IEC 61800 series [21, 22, 23, 24].
- **Short interruptions/re-closing (0.1–10 s):** Although electrical power may be restored after a short interruption, the sudden stoppage and restart of pumps introduce hydraulic transients and air ingress into the pipeline network, while control systems may lose their operational state. As a result, the plant requires a

controlled re-sequencing of pumps, valves, and control logic before normal operation can resume [25, 26, 27, 28]. In addition, delays in re-establishing turbidity and chlorine compliance extend plant downtime well beyond the outage duration, as evidenced by GRIDCo disturbances in February–March 2024 [10, 11].

- **Transients/surges:** Lack of rated lightning surge arrestor (LA) or the lack of maintenance for LA's in local substations results in the impact of lightning strike on long feeders being directly reflected as over-voltages in the grid supply, damaging PLC I/O, instrumentation PSUs, and VFD front-ends lacking surge suppression. These create latent recurring faults until boards are replaced. [14, 16, 17].

1.1.5 Microgrid as a Potential Solution

Definition and Types

Given the B-WTP's frequent power outages and equipment sensitivity to voltage and frequency deviations, an alternative solution, such as a microgrid should be considered. According to the United States Department of Energy, a microgrid is a group of interconnected loads and distributed energy resources within clearly defined electrical boundaries that acts as a single controllable entity [29]. Unlike the traditional power grid, in which electricity is generated at large power plants and transmitted over long distances, a microgrid integrates local energy sources and directly supplies nearby loads. There are different types of microgrids:

1) Grid-connected, it remains physically connected and exchanges energy with the main utility grid.
2) Off-grid (island mode) is a self-sufficient energy system that generates, stores, and manages power independently of the traditional power grid.
3) Hybrid microgrid, it combines elements of the grid connected and the off-grid types of microgrid.

Figure 1.4 provides a visual representation of the elements involved in a microgrid.

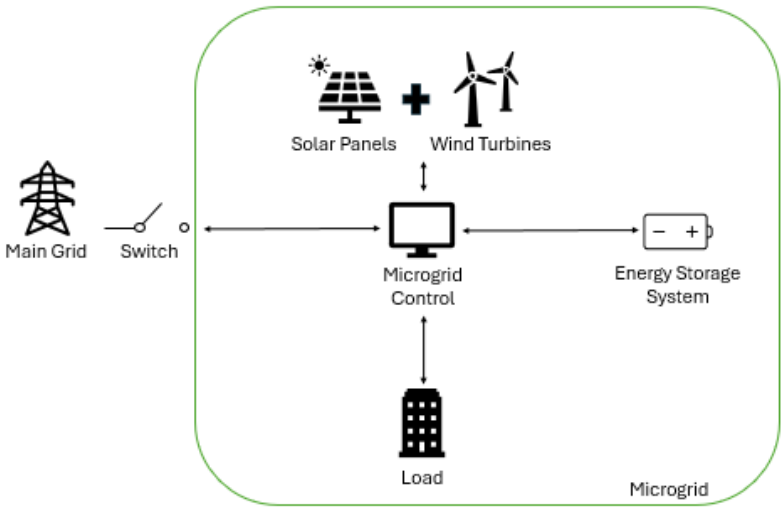

Figure 1.4. Conceptual diagram illustrating the main components and structure of a microgrid.

Flexibility and Relevance to Ghana

The ability to incorporate multiple energy generation technologies is what distinguishes microgrids from conventional power systems. In practice, this means renewable options, such as PV panels and WT, can be integrated with traditional units, such as diesel generators. Such a configuration enhances both supply reliability and system sustainability, with BESS playing a key role in balancing production and demand and ensuring voltage and frequency stability. In Ghana, where solar potential is exceptionally high, and some regions also benefit from wind resources, this flexibility makes microgrids especially suitable. Given the critical infrastructure of the B-WTP, which depends on continuous electricity for its pumping and treatment processes, grid power outages not only disrupt the plant but also threaten the water supply of nearby communities [30]. A well-designed microgrid could address these vulnerabilities by ensuring continuous operation even during extended grid outages.

1.1.6 Role of Energy Storage Systems

Energy Storage Systems (ESS) are a key enabling component of modern grids, particularly in configurations with high shares of renewable energy generation.

Autonomy and Backup

A primary function of ESS is to provide backup energy when generation is insufficient. In a microgrid with solar and wind sources, the output is inherently variable. When solar irradiance drops or wind subsides, storage enables the system to discharge and maintain

supply to loads. In practice, ESS can provide hours to days of autonomy depending on size and design [31]. Figure 1.5 gives a graphical representation of an ESS.

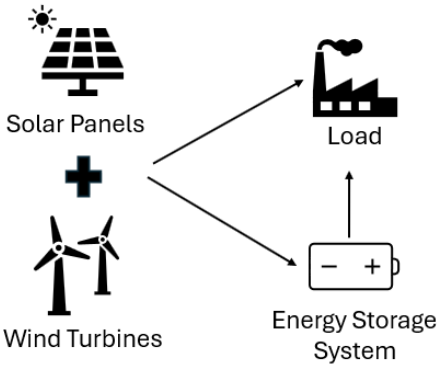

Figure 1.5. Conceptual illustration of an ESS supporting microgrid autonomy by balancing generation from solar and wind sources and supplying the load.

Sizing the storage system is a critical design challenge, where one must trade off between capital cost and backup autonomy. Several optimization studies propose methods for sizing battery systems to meet reliability indices while minimizing cost [32].

Frequency, Voltage Control, and Grid-forming Capability

Beyond energy buffering, ESS units in a microgrid often have to support power quality and stability. In islanded mode, the microgrid may lack the mechanical inertia provided by large synchronous generators. ESS (through battery inverters) can act as a virtual inertia or provide fast frequency regulation and voltage support. This helps stabilize transient disturbances, sudden load changes, or fluctuations in renewable input [33] [31]. In fact, an ESS coupled with intelligent control can enable smooth transitions between renewable and storage backup sources, ensuring that motors and sensitive equipment are protected from voltage fluctuations [34]. ESS in microgrids are commonly classified into three main control types:

- Grid-forming BESS establish and regulate system voltage and frequency, enabling stable islanded operation and black-start capability.
- Grid-following BESS synchronize to an existing grid reference and primarily inject or absorb power under grid-connected conditions.
- Grid-supporting BESS complement grid operation by providing ancillary services such as voltage support and frequency regulation, thereby enhancing overall microgrid stability and reliability.

Managing Variability and Uncertainty Considerations

Renewable generation (especially PV) is intermittent; hence, ESS must help integrate mismatches across multiple time scales (intra-hour, daily, seasonal). A robust control strategy is required to address uncertainty in generation and load [35] [36].

Types of Storage Technologies

Various storage technologies can be considered:

- Lithium-ion batteries: Offer high efficiency, fast response, and high energy density, making them suitable for both grid-forming and grid-following ESS in microgrids.
- Flow Batteries: Store energy in electrolytes, making them suitable for long-duration energy storage. These systems are typically used in grid-following applications or as energy buffers due to their slower dynamic response.
- Lead-acid: Traditional and economical option often used for smaller applications as a backup and in grid following applications.
- Emerging options (e.g, sodium-sulfur, superconducting magnetic energy storage) exist, but are often less mature, more expensive, or require specialized conditions.

1.1.7 Technical and Economic Challenges

Although microgrids offer a promising pathway to improving energy reliability and sustainability, several technical and economic challenges remain.

From a technical perspective, one of the primary concerns is the variability of renewable energy sources, such as solar and wind, which can lead to supply instability, particularly in islanded microgrids without an external grid to provide ancillary services. This requires careful sizing of ESS and the use of advanced power electronics capable of managing grid formation [37]. Another technical challenge relates to the protection of sensitive equipment. Facilities like B-WTP rely on large induction motors that are vulnerable to under-voltage and frequency deviations [30]. Without proper control strategies and backup capacity, microgrids risk equipment damage. Designing such systems, therefore, requires not only investment in hardware but also in intelligent software capable of predicting demand fluctuations and optimizing resource utilization.

Economically, microgrid implementation is hampered by high initial Capital Expenditures (CAPEX). PV panels, WT, storage units, and advanced control technologies represent high upfront costs [38]. Although Operating Expenses (OPEX) are generally lower over the system's lifetime than those of diesel-based solutions, the long payback period often creates financial barriers. Facilities such as water treatment plants may face additional

difficulties in securing financing without any external support.

Further barriers relate to maintenance and technical expertise. Microgrids require specialized knowledge for installation, operation, and long-term maintenance, but such expertise may not always be available locally. Without sustained investment in human resources, even well-designed microgrids may struggle to deliver the desired benefits [39].

1.1.8 Emerging Insights from the Problem Analysis

The preceding analysis has traced multiple inconveniences affecting the B-WTP, operational difficulties, insufficient grid power availability, and power quality issues in the existing supply. Each of these dimensions has clear connections with cost, service life, and operational planning. Yet when these layers are weighed against one another, a consistent pattern emerges: **Power availability is the most decisive factor undermining the reliable supply of clean water to the community** [6, 25, 10]. From a humanitarian perspective, the consequence is distinct. The B-WTP is designed to ensure a continuous supply of safe drinking water for tens of thousands of people. Still, that mission is frequently bothered by electrical power outages and instability. The brunt of an electrically vulnerable grid translates to severe physical health hazards and risks borne by the community due to the consumption of unsafe, contaminated water [26].

As proposed, a **microgrid architecture bounded with renewable sources (PV and Wind)** offers this solution: insulation from grid cutbacks and long-term operational cost reduction [40]. However, RES are inherently volatile for night-time suitability, which introduces additional challenges. Batteries can firm volatile generation, providing ride-through for such disturbances, and even inject fast frequency response to stabilize the microgrid during fault incidents. But they are also capital-intensive and unstable. Overuse of batteries for stability support shortens their useful life and increases life-cycle costs. Thus, while batteries are indispensable for ensuring system reliability, they must be optimally sized and carefully integrated into economic analyses, stability studies, and load dispatch strategies [6].

Beyond reliability and economics, there is also a **sustainability dimension**. The adoption of a renewable-dominant microgrid in the B-WTP is not only a technical fix to supply and quality problems; it is also a **contribution to de-carbonization and climate goals**. By using local solar and wind resources, the project reduces the plant's footprint, diversifies its energy base, and demonstrates how essential public infrastructure can transition to sustainability. In this sense, the microgrid is both an operational safeguard and a **step toward a cleaner, more resilient energy future for Ghana** [6, 18].

1.2 Problem Definition

Access to reliable electricity in Ghana remains limited, and frequent outages and unstable grid conditions severely affect critical infrastructure, including the B-WTP. Current Backup solutions, such as diesel generators, are unsustainable primarily due to environmental concerns and fuel supply logistics. In contrast, reliance on an unstable grid supply threatens both water security and equipment. Microgrids with RES and storage have the potential to enhance reliability and sustainability, but their design must account for technical, economic, and operational challenges within the local Ghanaian context. To address this problem, the following problem definition is given:

How can a renewable energy-based microgrid with integrated energy storage be designed and controlled to provide a reliable and sustainable power supply for the Bukunor Water Treatment Plant in Ghana, while remaining technically feasible and economically viable?

To obtain a complete formulation of the problem definition, this project will aim to do the following:

- Develop a PLECS model that emulates a microgrid with PV, WT, together with an integrated BESS serving the peak and base load requirements for the B-WTP.
- Develop a current control strategy in Matlab/Simulink to control the Grid-following inverters in the microgrid.
- Validate the developed model using HIL test in the laboratory.

2 Energy Model

This chapter presents the energy model of the proposed microgrid for the B-WTP. The focus is on describing load demand and evaluating how PV and WT generation, together with BESS, can be combined to meet demand over time. Simplified models are used to simulate energy flows and to examine different system configurations. Ultimately, the most feasible configuration is selected.

2.1 Load Profile

This section provides an overview of how the load profile was developed and simulated under ideal operating conditions (i.e., uninterrupted power supply and full grid availability) over one year. This approach offers a clear understanding of the total energy required by the plant.

The load profile is the variation in electrical demand over a period and is a critical input to system design. It captures the plant's operational characteristics, including pumping, treatment, cooling, lighting, and other auxiliary processes, which contribute to fluctuations in energy consumption. A clear understanding of this load profile is essential for accurately matching the generation capacity of the renewable energy systems to the plant's demand, ensuring both reliability and operational efficiency.

Since the treatment plant has experienced frequent power outages, the load profile was reassessed and calculated under ideal operating conditions to represent the plant's expected performance in the absence of power interruptions.

The load profile used in this study represents the B-WTP's ideal operation on a typical day. To estimate annual energy demand, the daily load profile was multiplied by 365, providing a realistic basis for system sizing and performance evaluation.

The table presenting the different load configurations, indicating when the various loads are operational and when they are idle, is provided in Appendix A. From the table, the following was observed:

- The total energy consumption for the day is 21.132,86 kWh.
- The peak demand is 1.352,69 kWh.
- The minimum load is 171,19 kWh.

The results are visualized in Figure 2.1 below.

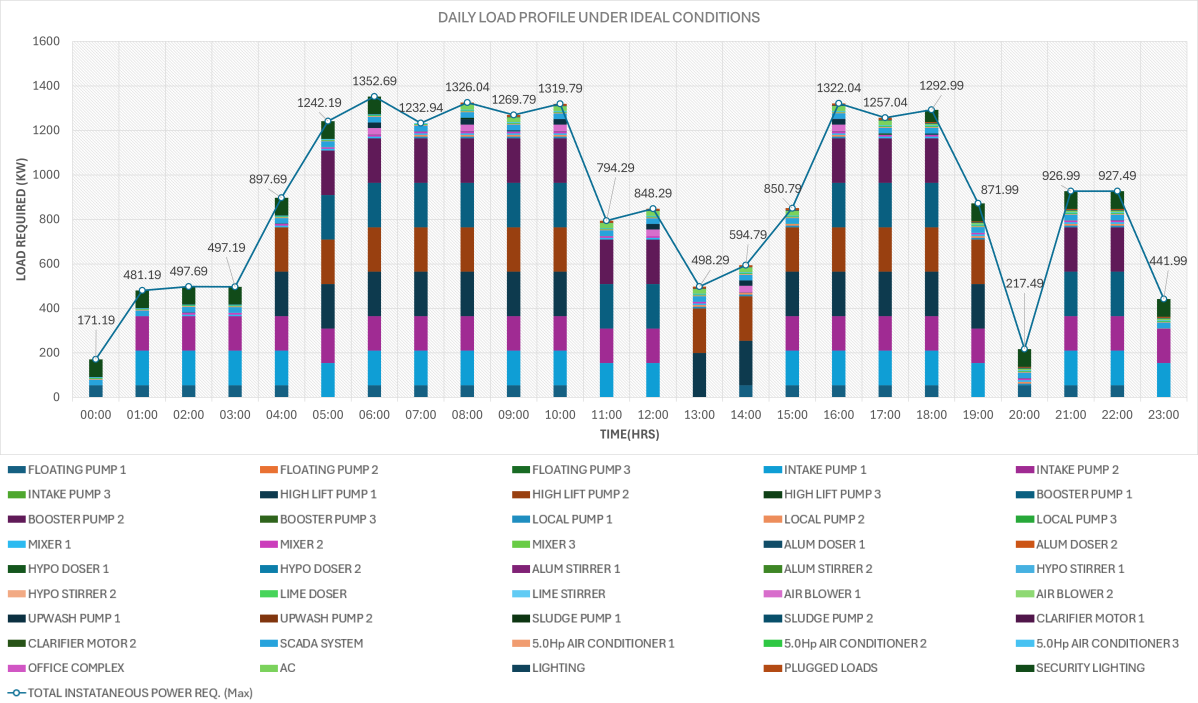

Figure 2.1. 24-hour load profile of the B-WTP under ideal operation conditions, showing the contribution of individual process loads and the total instantaneous power demand.

2.2 Renewable Energy Conversion

With 585 GW of capacity additions, globally, solar energy is the fastest-growing renewable energy source, followed by wind energy [41]. The report indicates that this record-breaking expansion in 2024 represents the most significant annual increase in renewable power capacity, with PV installations accounting for the largest share. Wind energy also exhibited substantial growth, driven by continued deployment of onshore systems and rapid advances in offshore wind technology.

In Ghana, both solar and wind resources are considered due to the nation's favorable geographical and climatic conditions. Ghana receives high levels of solar irradiation, typically 4,5-6,0 kW/m^2 per day, ensuring a reliable solar resource throughout the year [42]. Likewise, moderate to high wind speeds, particularly along coastal regions such as Ada, Anloga, Ningo, and Prampram, as well as portions of the Akwapim–Togo ranges and the northern Savannah zones, indicate significant potential for wind energy generation.

The combination of these two renewable resources provides a complementary energy mix, with solar energy (irradiance) dominant on average days, with wind power often peaking at night or during the dry season, as shown in Figure 2.2. A pattern that is critical for

system reliability, grid stability, and the overall sustainability of the hybrid microgrid plant.

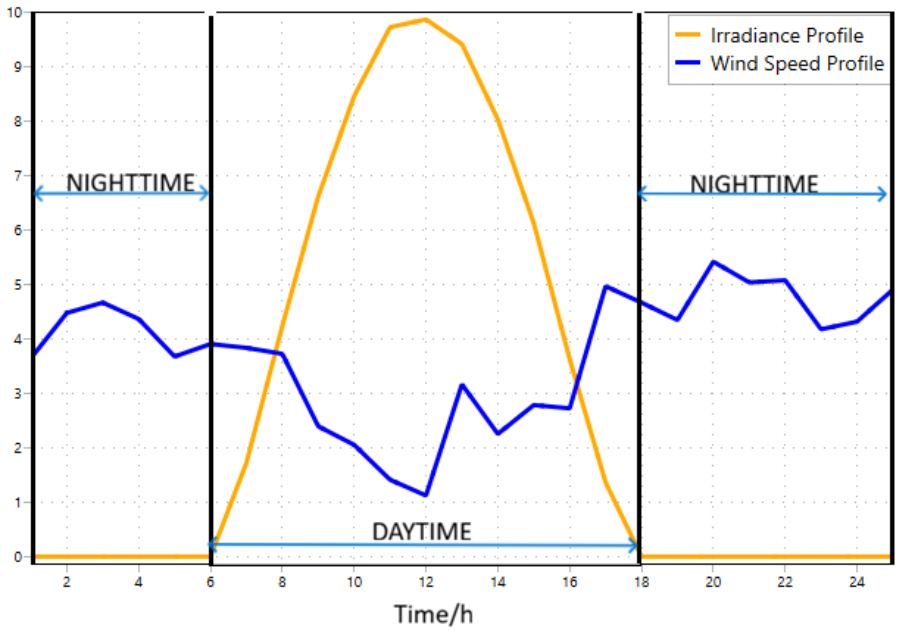

Figure 2.2. Average Daily Irradiance and Wind Speed Profile

The designed microgrid for the B-WTP relies primarily on PV and wind energy as its renewable energy sources. This section presents the core physical and mathematical models describing how solar radiation and wind kinetic energy are converted into usable electrical power.

2.2.1 PV Power Operation

PV panels convert solar radiation into electrical energy through the photovoltaic effect. For system-level analysis and energy simulations, a simplified PV power equation that expresses the panel output as a function of irradiance, temperature, and panel area is used. The instantaneous power output of a PV array used in the model is approximated in Equation 2.1.

$$P_{PV} = A_{panel} \cdot \eta \cdot G \cdot [1 - \beta \cdot (T_{cell} - T_{ref})] \tag{2.1}$$

- P_{PV} is the PV power output $[W]$
- A_{panel} is the total panel area $[m^2]$
- η is the nominal panel efficiency
- G is the solar irradiation $[\frac{W}{m^2}]$
- β is the temperature coefficient

- T_{cell} is the cell temperature [$°C$]
- T_{ref} is the reference temperature [$°C$]

The model assumes that the cell temperature increases with solar irradiation according to Equation 2.2

$$T_{cell} = T_{2m} + K \cdot G \tag{2.2}$$

Where T_{2m} is the ambient temperature, which is defined as a constant, and K is the thermal coefficient, which accounts for the heating effect of solar radiation on the PV cell surface.

2.2.2 PV Model

The PV model, as illustrated in Figure 2.3, computes the instantaneous DC power output as defined in Equation 2.1 based on the solar irradiance and temperature effects. The input irradiance data are imported from a file containing measured solar irradiance measurements for 2024 at the BWT Plant [43]. An average ambient temperature of 26$°C$, also reported in the same file, was used [43].

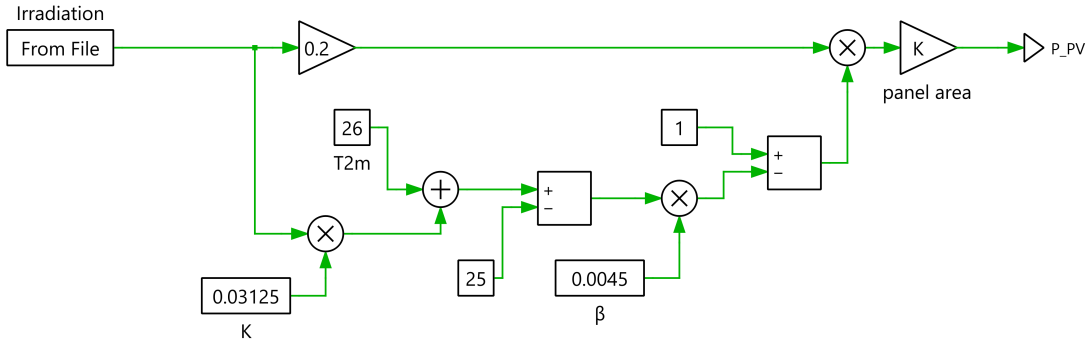

Figure 2.3. The PV model visualized in PLECS

2.2.3 PV Simulation

After the model was designed in PLECS, a panel area of 12.000 m^2 was considered, and the simulation was run using the irradiance from the downloaded file to obtain an overview of the generated solar power of 2 MW. The resulting graph for the first fifteen days of January is shown in Figure 2.6a. Particular attention is given to the worst-case scenario in Figure 2.8b, which clearly shows that power generation occurs only during the day.

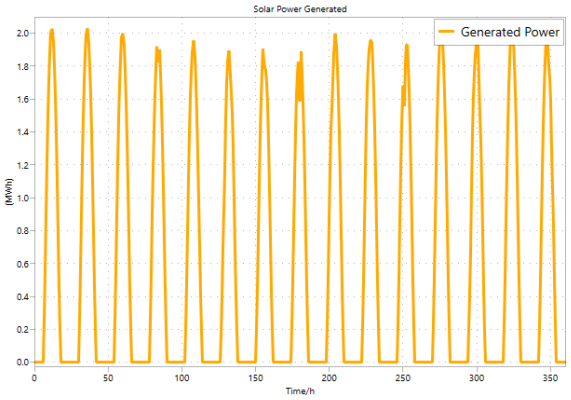

(a) Simulated PV power output for the first 15 days of January for 2 MW Solar Plant, using measured irradiance data.

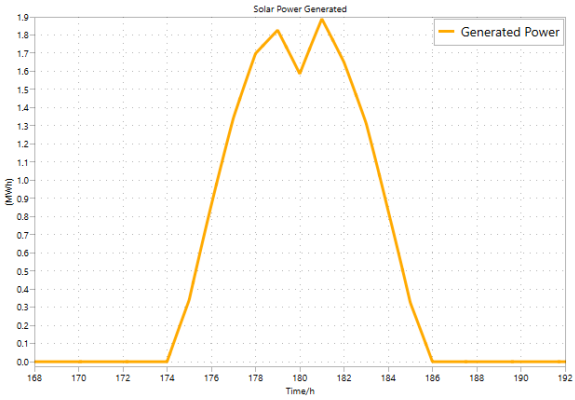

(b) Simulated PV power output on the lowest-generation day in January, highlighting that power is produced only during daylight hours.

Figure 2.4. Simulated PV power output of the 2 MW solar plant in January, comparing the first 15 days with the lowest-generation day derived from measured irradiance.

2.2.4 Wind Energy Conversion

Wind turbines extract kinetic energy from moving air and convert it into mechanical shaft power. This mechanical shaft power is subsequently converted into electrical power through a generator. The fundamental expression governing wind power extraction is defined in Equation 2.3.

$$P_{wind} = (\frac{1}{2} \cdot \rho \cdot A) \cdot C_p \cdot v^3 \tag{2.3}$$

where

- P_{wind} is the mechanical power extracted from the wind [W]
- ρ is the air density $[\frac{kg}{m^3}]$
- A is the rotor swept area $[m^2]$
- C_p is the power coefficient (set to 0.3 in this model)
- v is the wind speed $[\frac{m}{s}]$

The coefficient $(\frac{1}{2} \cdot \rho \cdot A)$ represents the kinetic energy content of the wind stream, while C_p accounts for the aerodynamic efficiency of the wind turbine. The cubic relation between wind speed and power indicates that even a small change in wind velocity can lead to a substantial increase in generated power.

2.2.5 Wind Power Model

The wind model estimates the instantaneous mechanical power output of the wind turbine as a function of available wind speed and turbine characteristics. The implementation of the model in PLECS is shown in Figure 2.5

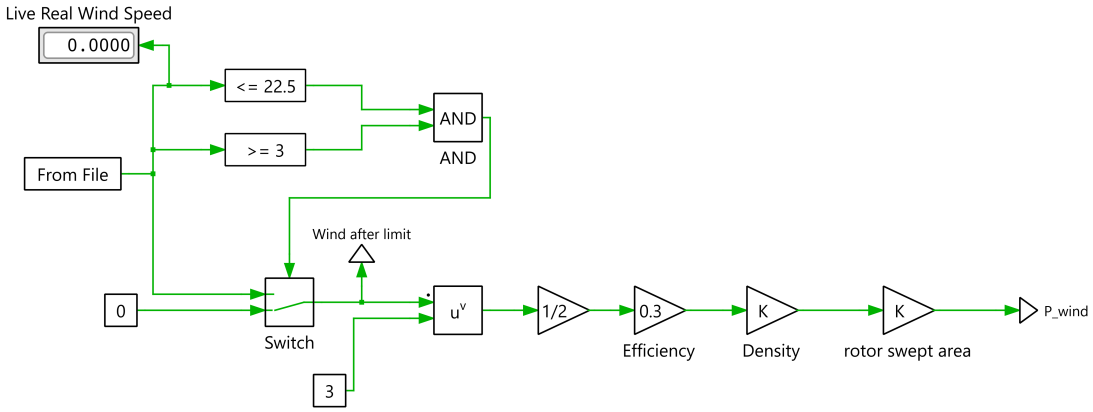

Figure 2.5. The wind power model visualized in PLECS.

The input wind speed data is imported from a file containing measured wind speed data for 2024 at the B-WTP [43]. To ensure realistic turbine operation, the model applies cut-in and cut-out wind-speed limits. The turbine operates only when the wind speed is between $3\frac{m}{s}$ and $22.5\frac{m}{s}$. Otherwise, the wind speed is set to zero. This logic is implemented using logical comparison and switch blocks, as shown in Figure 2.5.

The logical control block ensures that the turbine produces power only within its operational range, as defined by Equation 2.4

$$P_{wind} = \begin{cases} \frac{1}{2} \cdot A \cdot C_p \cdot v^3, & 3 \leq v \leq 22.5 \\ 0, & \text{otherwise} \end{cases} \tag{2.4}$$

This simplified model effectively captures the nonlinear relationship between wind speed and turbine output power while preventing unrealistic power generation at very low or very high wind speeds. The resulting P_{wind} signal is then used as an input to the overall microgrid power balance model.

2.2.6 Wind Power Simulation

After the model was designed in PLECS, a rotor area of 7.854 m^2 was considered, and the simulation was run using wind- speed data from the downloaded file to obtain an overview of the generated wind power. The January graph in Figure 2.6a shows that power is generated under certain conditions. Figure 2.8b shows the worst case of wind power generation in January.

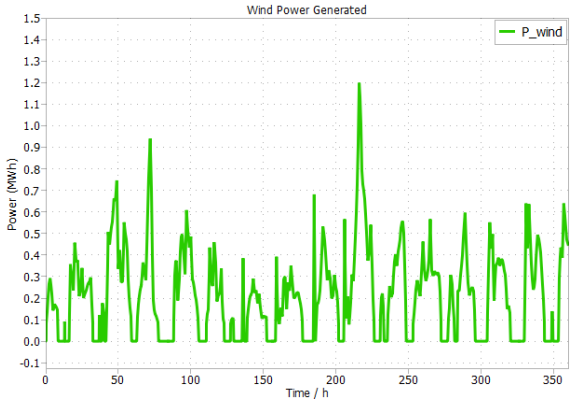

(a) Simulated wind power output for the first 15 days of January for a 7.854 m² rotor area, using measured wind-speed data.

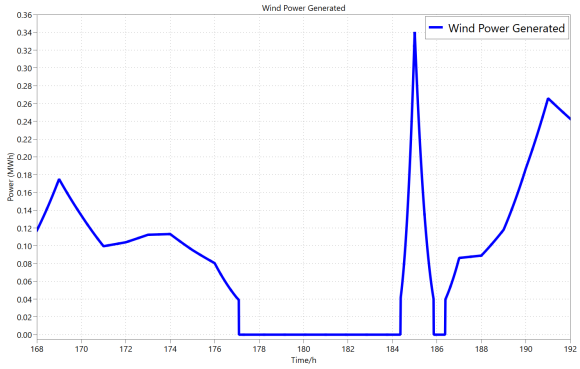

(b) Simulated wind power output on the lowest-generation day in January, illustrating that power is produced only under favorable wind conditions.

Figure 2.6. Simulated wind turbine power output in January for the 7.854 m² rotor, showing the first 15 days and the lowest-generation day derived from measured wind-speed data.

2.3 Battery Energy Storage

A BESS plays a central role in an islanded microgrid by balancing the mismatch between renewable power production and load demand. The battery in this project is modeled using a simplified energy-balance formulation. Instantaneous DC battery power is computed as the imbalance between total renewable generation and electrical load, corrected for conversion efficiency as defined in Equation 2.5

$$P_{bat,DC} = \eta_{PE} \cdot P_{total} - P_{load} \tag{2.5}$$

where

- $P_{bat,DC}$ is the Instantaneous DC battery power
- P_{total} is the sum of all renewable sources (PV+Wind)
- P_{load} is the electrical demand of the B-WTP
- η_{PE} is the power-electronic efficiency (set to 0,95)

A positive value of $P_{bat,DC}$ implies charging, while a negative value suggests discharging. The battery's stored energy is updated in discrete time by integrating the power flow:

$$E_{bat}(t) = E_{bat}(t-1) + P_{bat,DC}(t) \cdot \Delta t \tag{2.6}$$

where

- E_{bat} is the stored energy [Wh],
- Δt is the simulated time step.

This simple, integration-based representation aligns with the battery model implemented in PLECS, as shown in Figure 2.7.

The State of Charge (SoC) is defined as in Equation 2.7.

$$SoC = \frac{E_{bat}}{E_{capacity}} \cdot 100\% \tag{2.7}$$

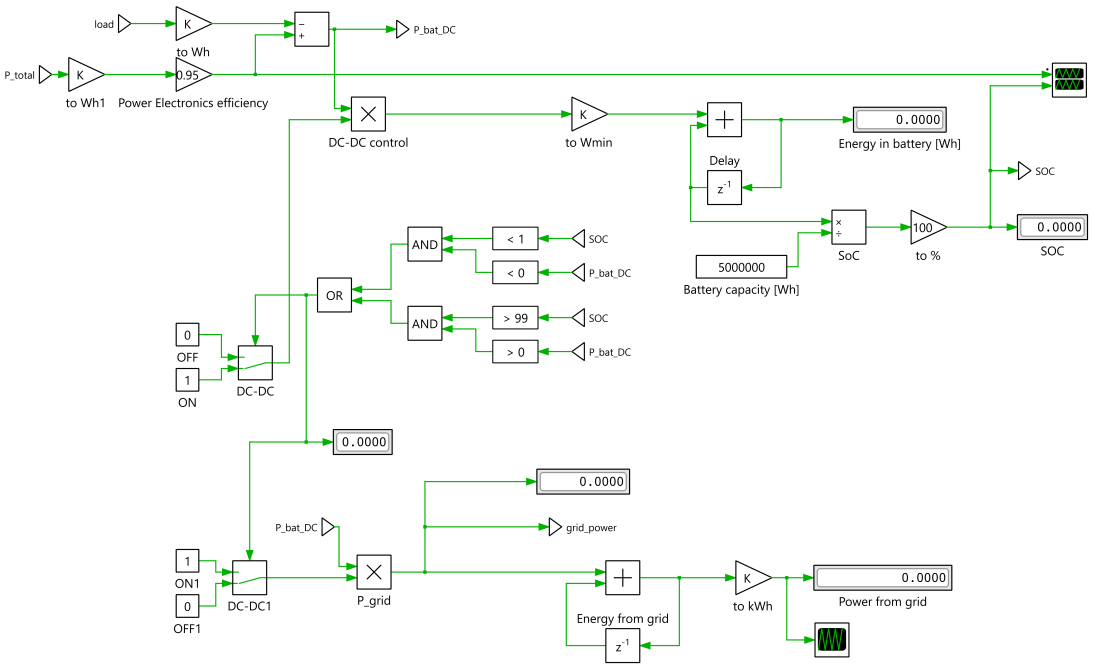

Figure 2.7. The BESS model visualized in PLECS

After implementing the model, a test run was made to be sure the battery model charges and discharges as required. The result of the test run is shown in Figure 2.8

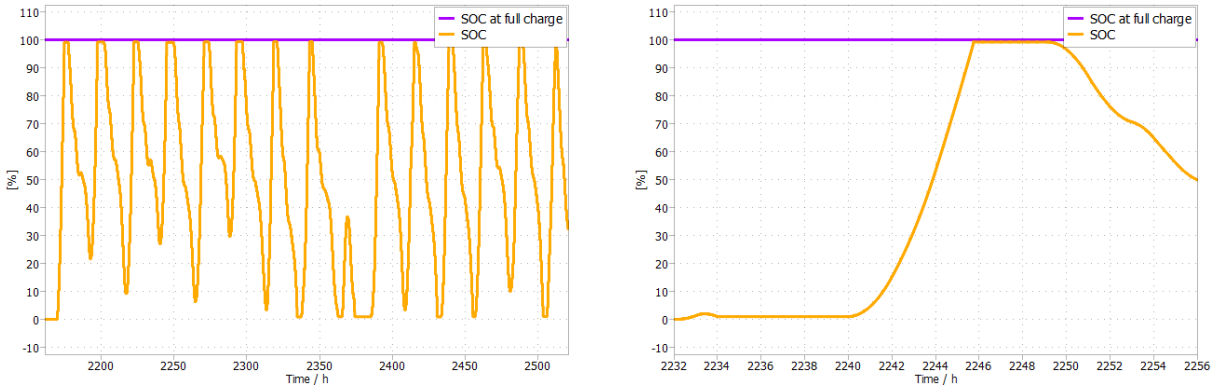

(a) Simulated SOC for One(1) day. ***(b)*** Simulated SOC for fifteen (15) days.

Figure 2.8. Simulated SOC BESS to be used.

2.4 Sizing of Power Generation System

The next step was to determine the optimal configuration of the power sources to be installed. To achieve this, 17 scenarios were simulated in PLECS to select the most suitable system configuration for the B-WTP. Four main factors stated below were considered when defining the scenarios to be simulated:

1) Peak power required in an hour,
2) Maximum Power that can be generated from Solar panels, by varying the Solar Panel Area
3) Maximum Power that can be produced from Wind Turbines, by varying the rotor diameter of the Wind Turbine; and
4) BESS: Since the plant has a capacity of 13 MWh, three main battery sizes were considered;
   - 5 MWh Battery
   - 10 MWh Battery
   - 15 MWh Battery

Table 2.1 below presents a summary of the scenarios simulated.

Table 2.1. Simulated Configurations

Scenario	**Configuration**	**PV Area [m^2]**	**Rotor Area [m^2]**	**Battery [MWh]**
1	PV + WT	12.000	7.854	-
2	PV + WT	20.400	7.854	-
3	PV + WT	24.000	7.854	-
4	PV + WT	24.000	-	-
5	PV + WT	-	15.708	-
6	PV + WT + BESS	12.000	7.854	5
7	PV + WT + BESS	24.000	7.854	5
8	PV + WT + BESS	12.000	15.708	5
9	PV + WT + BESS	12.000	7.854	10
10	PV + WT + BESS	24.000	7.854	10
11	PV + WT + BESS	18.000	7.854	10
12	PV + WT + BESS	20.400	7.854	10
13	PV + WT + BESS	12.000	15.708	10
14	PV + WT + BESS	18.000	11.781	10
15	PV + WT + BESS	12.000	7.854	15
16	PV + WT + BESS	24.000	7.854	15
17	PV + WT + BESS	12.000	15.708	15

The results of the 17 scenarios in Table 2.1 were then analyzed, and the results discussed in section 2.5.

2.5 Simulation Results and Analysis - Energy Model

This simulation aimed to analyse various scenarios for a hybrid energy system comprising PV/WT plants supported by a BESS. The system is designed to meet an annual load of 7.735 MWh. The main objective was to identify the optimal combination of these components' sizes that maximises self-sufficiency while maintaining reasonable economic profitability. To achieve this, seventeen different scenarios were simulated to monitor the system's hourly behavior over the year. After each simulation, total power production, the import/export profile, and BESS performance were evaluated. Based on these simulation results, key indicators of energy efficiency and system independence (self-consumption and self-sufficiency) were calculated.

The simulation results clearly show how different configurations and component sizing affect the behavior and performance of the hybrid system. Three main scenarios were simulated and subsequently expanded to seventeen scenarios. The results of these simulations are as follows:

2.5.1 Hybrid Power System (PV + WT)

As shown in Figure 2.9, the first set of simulations, which included only PV and WT plants, served as the starting point for analysing the relationship between local production and consumption. The power capacity of the PV plant was not fixed. Instead, it was varied across the three scenarios presented below.

Case	Cofiguration	P_PV (MWh/yr)	P_WT (MWh/yr)	P_total (MWh/yr)	Batt (MWh)	Export (MWh/yr)	Import (MWh/yr)	Net Export (MWh/yr)	Self consumption	Self sufficiency
1	PV + wind	4250	1076	5326	0	1584	3972	-2388	70%	49%
2	1.7*PV + wind	7225	1076	8301	0	4058	3471	587	51%	55%
3	2*PV + wind	8500	1076	9576	0	5217	3355	1862	46%	57%

Figure 2.9. The calculated yearly cases for PV + WT configurations without BESS, based on different sizing options

Figure 2.10a and Figure 2.10b show that significant amounts of energy are imported and exported over a month, and therefore there is a need to install an energy storage system.

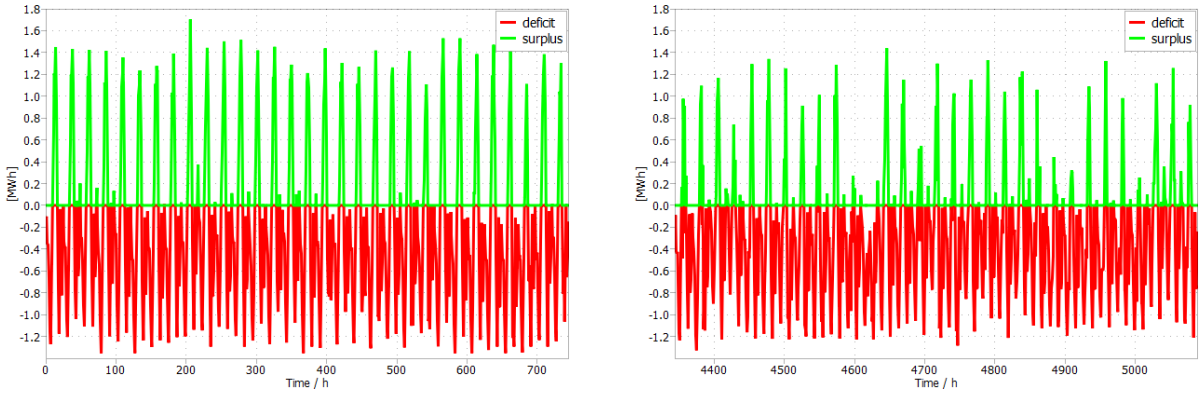

(a) January ***(b)*** July

Figure 2.10. Monthly Overview of import–export profiles - without BESS (Case 1)

To make it clearer, Figure 2.11a and Figure 2.11b show the power exported and imported energy during just one day in two different months.

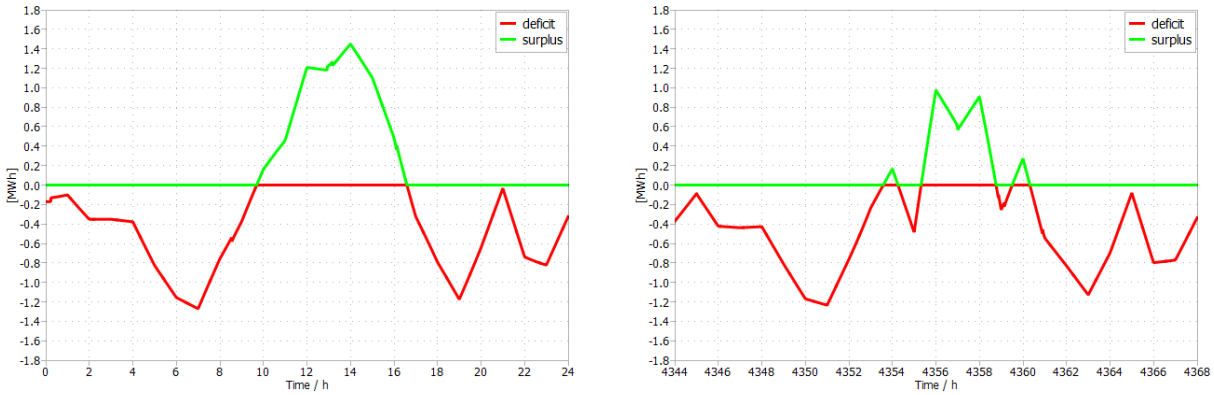

(a) January 1st ***(b)*** July 1st

Figure 2.11. Daily Overview of import–export profiles - without BESS (Case 1)

In the following simulations (Cases 2 and 3), the capacities of individual sources were gradually increased to examine how this affected the energy balance. As shown in Figure 2.9, increasing installed PV power leads to higher production and a significant increase in energy export during periods of high solar activity. Adding more wind turbines improved the daily output distribution because wind power is generated even at night. However, a portion of the generated energy still had to be exported to the grid.

2.5.2 Single energy source (Only PV/WT)

The next set of simulations, shown in Figure 2.12, analyses single energy sources in order to evaluate their individual impact on the system.

Case	Cofiguration	P_PV (MWh/yr)	P_WT (MWh/yr)	P_total (MWh/yr)	Batt (MWh)	Export (MWh/yr)	Import (MWh/yr)	Net Export (MWh/yr)	Self consumption	Self sufficiency
4	only 2*PV	8500	0	8500	0	5033	4247	786	41%	45%
5	only 2*wind	0	2152	2152	0	240	5802	-5562	89%	25%

Figure 2.12. The calculated yearly cases for single source configurations, based on different sizing options

As shown in Figure 2.13, the daily PV production covers the load only during daylight hours, while no electricity is generated between approximately 19:00 and 07:00. This clearly demonstrates that PV alone cannot ensure a continuous supply.

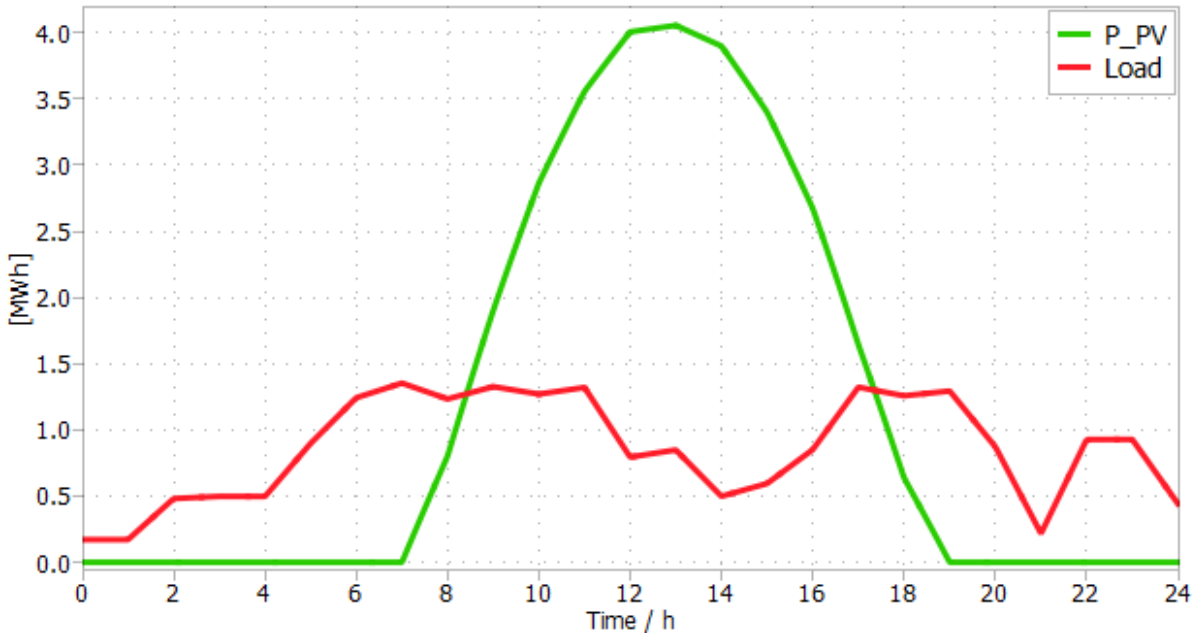

Figure 2.13. Daily PV Generation and Load Profile - Representative Low-Sun Day (Case 4)

In Figure 2.14, a representative low-wind day was selected to illustrate the limitations of using wind power as the sole energy source. The red curve shows the daily load, while the green curve shows wind power generated during the day.

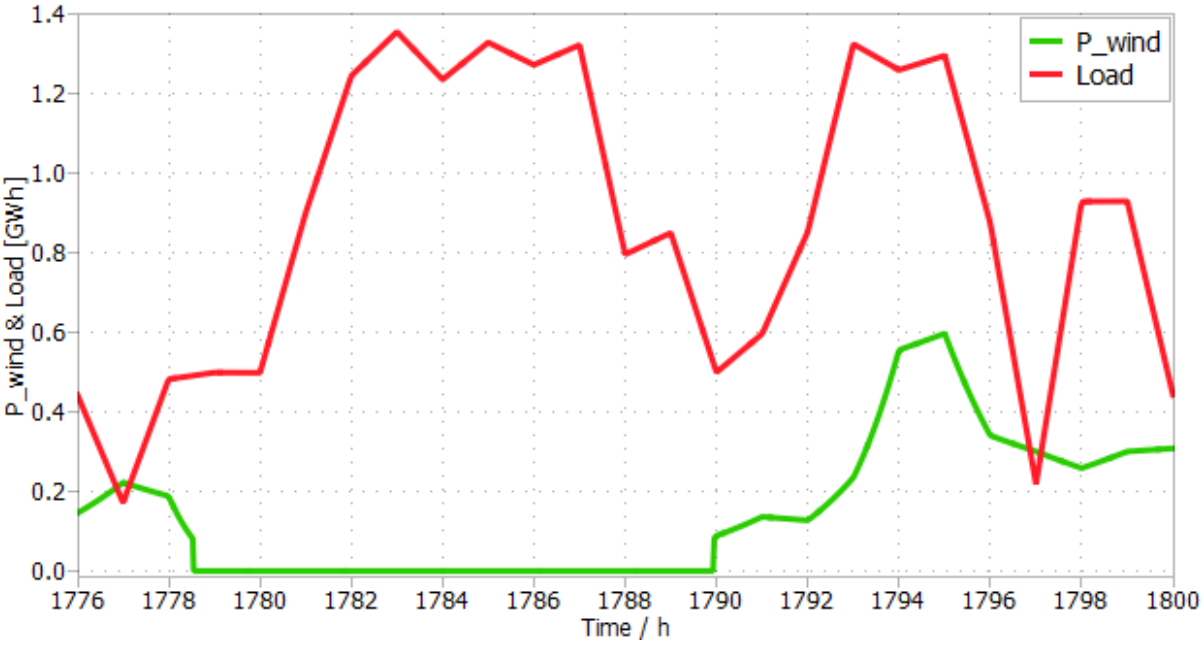

Figure 2.14. Daily Wind Generation and Load Profile - Representative Low-Wind Day (Case 5)

Based on these results, it was determined that using only a wind farm at the selected location in Ghana is not feasible, as the available wind potential is insufficient to ensure continuous and reliable energy production.

2.5.3 Integration with BESS (PV + WT + BESS)

To address the limitations identified in the previous subsection, a battery storage system was integrated into the model, and the final set of simulations was conducted using the configuration shown in Figure 2.15.

Case	Cofiguration	P_PV (MWh/yr)	P_WT (MWh/yr)	P_total (MWh/yr)	Batt (MWh)	Export (MWh/yr)	Import (MWh/yr)	Net Export (MWh/yr)	Self consumption	Self sufficiency
6	PV + wind + Batt.	4250	1076	5326	5	35	2726	-2691	99%	65%
7	2*PV + wind + Batt.	8500	1076	9576	5	3065	1651	1415	68%	79%
8	PV + 2*wind + Batt.	4250	2152	6402	5	119	1803	-1684	98%	77%
9	PV + wind + 2*Batt.	8500	1076	9576	10	0	2687	-2687	100%	65%
10	2*PV + wind + 2*Batt.	8500	1076	9576	10	1746	373	1372	82%	95%
11	1.5*PV + wind + 2*Batt.	6375	1076	7451	10	225	886	-661	97%	89%
12	1.7*PV + wind + 2*Batt.	7225	1076	8301	10	733	593	141	91%	92%
13	PV + 2*wind + 2*Batt.	4250	2152	6402	10	17	1704	-1688	100%	78%
14	1.5*PV + 1.5*wind + 2*Batt.	6375	1614	7989	10	447	596	-149	94%	92%
15	PV + wind + 3*Batt.	4250	1076	5326	15	0	2688	-2688	100%	65%
16	2*PV + wind + 3*Batt.	8500	1076	9576	15	1564	188	1376	84%	98%
17	PV + 2*wind + 3*Batt.	4250	2152	6402	15	0	1691	-1691	100%	78%

Figure 2.15. The calculated yearly cases for PV + WT + BESS configurations, based on different sizing options

Figure 2.16a highlights the need for storage by showing the daily import and export profile without a BESS. In this case, surplus energy is exported to the grid because it cannot be stored, while periods of low production require importing electricity from the grid.
When a BESS was added to the model, a significant increase in self-sufficiency and self-consumption was observed. Excess energy could be stored and used during periods of reduced production, thereby decreasing dependence on the grid, as shown in Figure 2.16b.

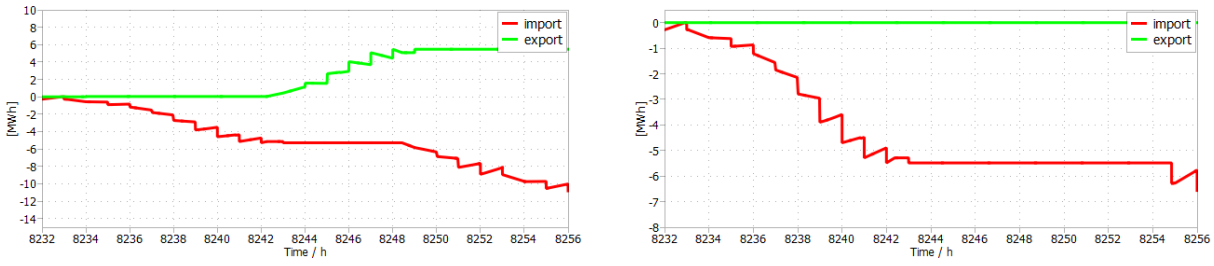

(a) Without BESS (Case 1) ***(b)*** With BESS (Case 6)

Figure 2.16. Daily import–export profiles for the PV–wind system

This is further illustrated in Figure 2.17, which shows the daily profiles of energy production, load, and battery SoC for case 9, which includes 8500 MWh of PV, 1076 MWh of WT, and a 10 MWh battery. The day starts off with a discharged battery (SoC = 0%), indicating a clear import from the grid. The red curve shows the daily load, the green shows total power generated during the day, and the orange one shows battery SoC.

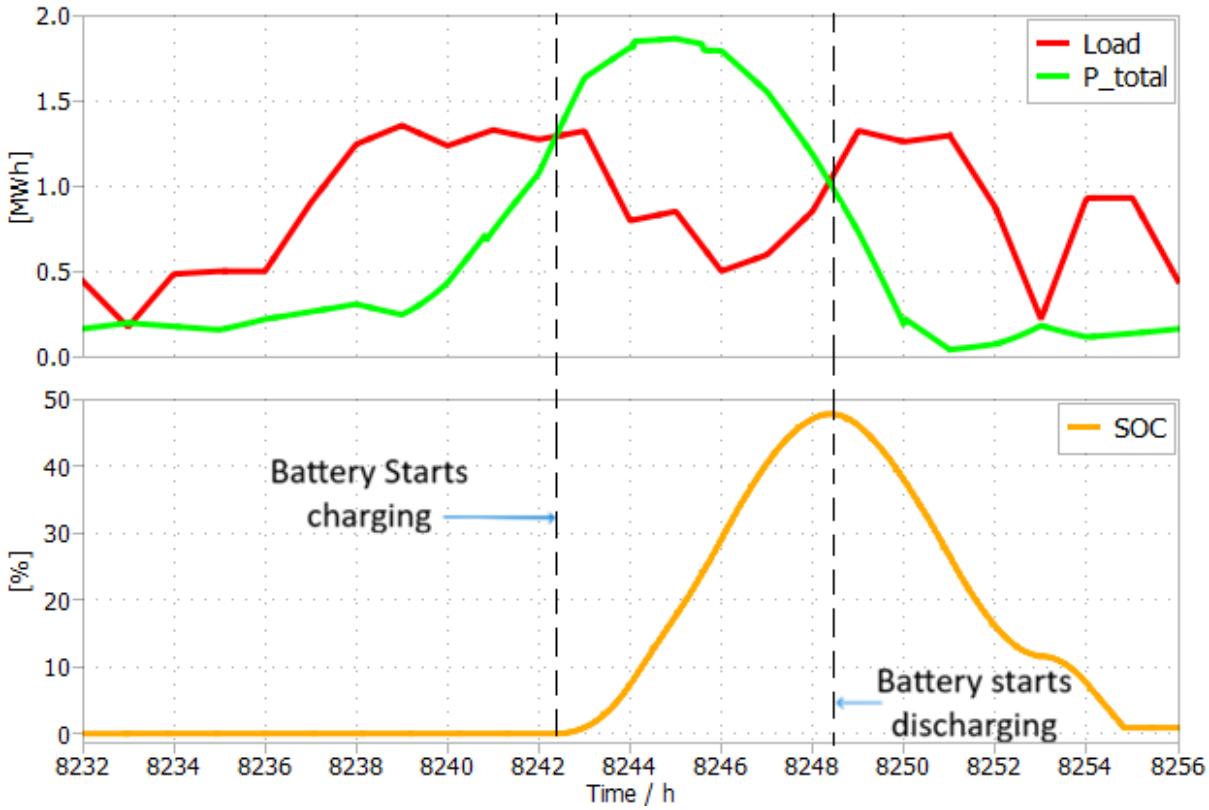

Figure 2.17. Daily generation, load, and battery SoC for a representative operating day (Case 9)

During periods when production exceeds consumption, the surplus energy is used to charge the battery, increasing SoC. Later in the day, as production declines, stored energy is used to supply the system, reducing SoC.

However, it has been shown that an excessive increase in battery capacity, e.g., to 15 MWh, is not justified without an increase in the installed capacity of PV or wind systems. As illustrated in Figure 2.18a (monthly profile) and Figure 2.18b (daily profile), the available production is insufficient to charge such a large battery, causing it to operate only within a narrow SoC range of approx. 0-35% throughout the whole year. Consequently, the system would still have to import energy from the grid during periods of low solar irradiance or low wind speed.

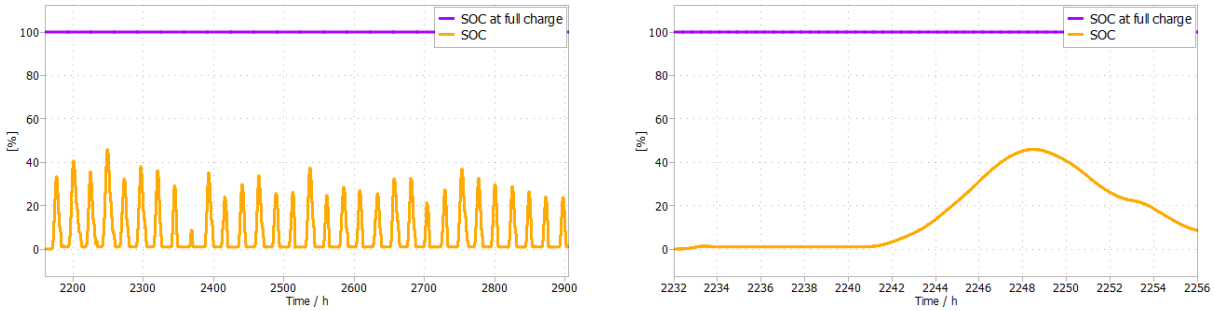

(a) High-Production Month (April) ***(b)*** High-Production Day (April 3rd)

Figure 2.18. SoC of 15 MWh Battery (Case 15) - Under utilization

Among the cases analysed, 12 and 14 proved to be the most favorable. Case 12 includes 7225 MWh of PV, 1076 MWh of WT, and a 10 MWh battery, whereas case 14 comprises of 6375 MWh of PV, 1614 MWh of WT, and a 10 MWh battery. Both cases achieve a high level of self-sufficiency (92%), whereas case 14 has slightly higher self-consumption (94%) and lower energy exports, making it technically more balanced. On the other hand, case 12 is financially more favorable when excess energy can be sold at an acceptable price.

Overall, the results indicate that the combination of PV and wind with a 10 MWh battery offers the best trade-off between technical efficiency and economic profitability.

2.6 Economic Analysis

Based on the simulation results, the next step is to analyse the economic impact of the cases. Based on the simulation results, cases 12 and 14 were selected for financial analysis. Although case 16 had promising results, it would not be feasible to have a 15 MWh battery. The average cost for a lithium-ion battery is 334 $/kWh [44]. This would make the battery alone cost $5.01 million.

In case 12, the battery capacity is 10 MWh, the PV panel area is 20.400 square meters, and the swept area of a 250 kW wind turbine is 7.854 square meters. The battery would cost $3,34 million. The average cost of PV power, C_{PV}, is defined in Equation 2.8 and Equation 2.9:

$$P_{\text{DC}} = A_{\text{PV}} \cdot \eta_{\text{PV}} \cdot G_{\text{STC}} \tag{2.8}$$

$$C_{\text{PV}} = P_{\text{DC}} \cdot c_{\text{PV}} \tag{2.9}$$

Where:

- A_{PV} : Total photovoltaic array area [m^2]
- η_{PV} : PV module conversion efficiency (decimal)
- G_{STC} : Solar irradiance under Standard Test Conditions [W/m^2]
- c_{PV} : Installed PV cost per watt [$/W]
- P_{DC} : Photovoltaic DC output power [W]
- C_{PV} : Total installed photovoltaic system cost [$]

Using these equations, P_{DC} is 3,264 MW, and the cost to install the system is $3,92 million [45]. The cost of installing a wind turbine is defined in Equation 2.10:

$$C_{\text{wind}} = P_{\text{wind}} \cdot c_{\text{wind}} \tag{2.10}$$

where:

- P_{wind} : Rated wind turbine electrical power output [W]
- c_{wind} : Installed wind turbine cost per watt [$/W]
- C_{wind} : Total installed wind turbine cost [$]

The total price for the wind turbine would be $ 4,54 million [46]. Making the total price for case 12, $ 11,8 million. For case 14, the battery storage remains the same; the PV area is reduced to 18.000 square meters, and the wind area is increased to 11.781 square meters. This reduces the cost of PV installation to $3,46 million, but increases the price of the wind turbine installation to $6,8 million. Making the total cost of case 14 $13,6 million. Thus, from an economic standpoint, case 12 is the best solution, as it will significantly improve Bukunor's reliance on the grid while incurring lower CAPEX.

3 Converter Model

The Energy Level Model was used to obtain a clear understanding of the load profile from the Bukunor WTP and the renewable energy generation profiles from different sources, namely solar energy from the PV model and wind energy from the WT model, using arithmetic equations for power generation. The hourly deficit was clearly identified as an excess that persists throughout the simulation period (1 year). Using this data, the battery was optimally sized to reduce dependence on the grid while achieving a substantial percentage of self-consumption of renewable energy.

In this section, the modeling of converters that connect these power generation sources to the grid is examined in greater detail. The technical concepts and mathematical equations governing the design of the converter topology and its connection to the grid are first discussed. Then, the control strategy and the controller type used to control the converters, enabling them to deliver the required power at the specified instants specified in section 2.5, are discussed.

After the theoretical concepts have been presented, a description is given of how a simplified average model of the converters was first built in MATLAB/Simulink and PLECS, and how this model was then modified to a switched-converter model by changing the plant topology. Towards the end of this section, the simulation results are discussed, along with several technical and design challenges considered during model development.

3.1 Reference Frame Transformations

The first concept to be discussed is the transformation of reference frames. Three-phase AC systems are naturally described in an ABC frame, where currents and voltages of each phase are treated as separate sinusoidal quantities. Although this representation matches physical reality, it is not considered convenient for control and analysis, since complex controllers are required to operate across multiple variables and in time-variant environments. To convert time-varying, coupled signals that require sinusoidal steady-state reasoning into a simplified time-invariant variable, a sequence of mathematical transformations is applied, as explained below. [47, 48]

$$\text{ABC} \xrightarrow{\text{Clarke}} \alpha\beta \xrightarrow{\text{Park}} dq$$

Each transformation reduces signal complexity and enables control strategies similar to those used in DC systems. The dq frame, in particular, transforms sinusoidal AC quantities into DC-like steady state values, which are significantly easier to regulate using PI controllers. A complex plane representation of the difference reference frames has been mentioned in Figure 3.1.

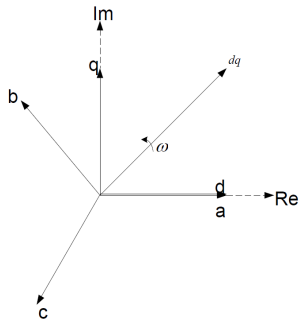

Figure 3.1. Orientation of the dq and three-phase systems in the complex plane

3.1.1 Clarke Transformation (ABC→ $\alpha\beta$)

The Clarke transformation converts a balanced three-phase system from the ABC reference frame to the orthogonal two-axis $\alpha\beta$ reference frame. This transformation reduces the system's dimensionality while preserving the essential information required for control, measurement, and analysis.

In the $\alpha\beta$ frame, the resulting components i_α and i_β form a stationary orthogonal coordinate system. Compared to the original three sinusoidal signals, which are oscillating and phase-shifted, the $\alpha\beta$ components offer a more compact and geometrically intuitive representation. This makes the Clarke transformation a standard tool for controlling, for example, inverter-based microgrids [49].

The transformation is expressed in Equation 3.1, where the three-phase currents i_a, i_b, i_c, are projected into the orthogonal $\alpha\beta$ reference frame:

$$\begin{bmatrix} i_\alpha \\ i_\beta \end{bmatrix} = \frac{2}{3} \begin{bmatrix} 1 & -\frac{1}{2} & -\frac{1}{2} \\ 0 & \frac{\sqrt{3}}{2} & -\frac{\sqrt{3}}{2} \end{bmatrix} \begin{bmatrix} i_a \\ i_b \\ i_c \end{bmatrix} \tag{3.1}$$

3.1.2 Park Transformation ($\alpha\beta \rightarrow dq$)

The Park transformation rotates the stationary $\alpha\beta$ reference frame into a synchronous rotating reference frame known as the dq frame. This transformation is fundamental in inverter and motor control, because it converts AC quantities into DC-like values when the reference frame rotates at the same angular frequency as the electrical system.

In the dq frame:

- The d-axis component typically represents the active-power-related quantity.
- The q-axis component represents the reactive-power-related quantity.

When the angular position θ corresponds to the phase of the AC voltage, the transformed variables become essentially constant in steady-state operation. This simplifies control design, since PI-controllers can regulate DC-like quantities instead of oscillating sinusoidal signals [50]. The mathematical structure of the Park transformation is shown in Equation 3.2.

$$\begin{bmatrix} i_d \\ i_q \end{bmatrix} = \begin{bmatrix} \cos\theta & \sin\theta \\ -\sin\theta & \cos\theta \end{bmatrix} \begin{bmatrix} i_\alpha \\ i_\beta \end{bmatrix} \tag{3.2}$$

Here, θ represents the instantaneous electrical angle of the synchronous frame. In grid-following inverters, θ is obtained from a Phase-Locked Loop (PLL), which is described in detail in subsubsection 3.4.1, while grid-forming inverters form their own references. [47, 48]

3.2 Average Model Plant

This section introduces the average microgrid model, which serves as the plant model for converter-level modeling. The averaged model represents the electrical behavior of the microgrid in a simplified, computationally efficient form. Instead of switching-level converters, the model uses averaged voltage sources to emulate the steady-state behavior of the PV inverter, wind inverter, and the grid interface. This reduces computational load while preserving the fundamental power-flow relationships required for control design and dynamic analysis[51]. An overview of the averaged plant implemented in PLECS is shown in Figure 3.2.

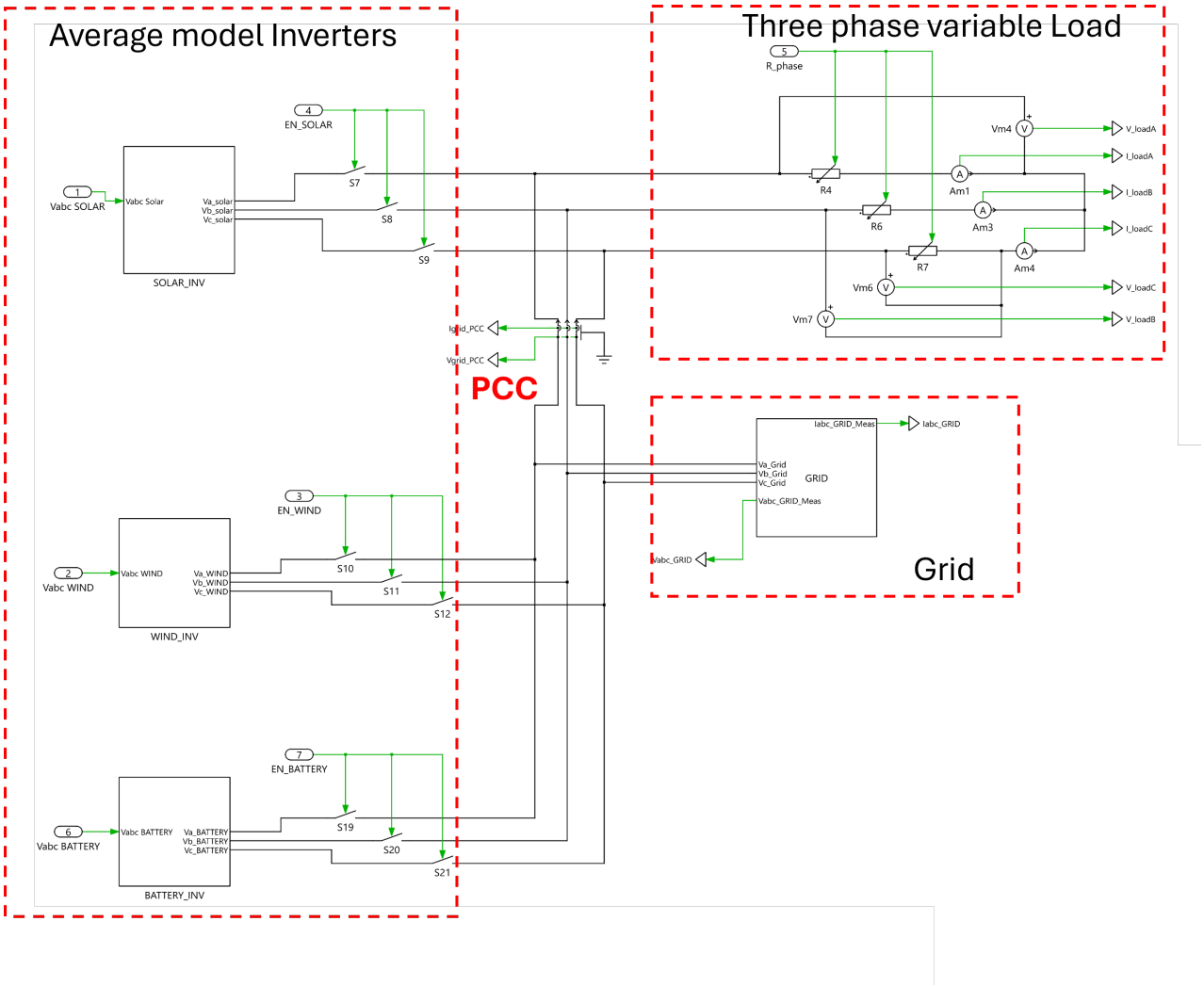

Figure 3.2. Overall Average Plant Model implemented in PLECS

Averaged Inverter Model (Solar, Wind and Battery)

All three inverters in the microgrid (PV, WT, and battery) use the same averaged three-phase inverter topology, shown in Figure 3.3. Only the reference voltages vary with the power reference derived from the energy-level model for the individual generation source type. The inverters are represented as a three-phase voltage source in a switching-cycle-averaged model. The commanded phase voltages V_a, V_b, V_c are applied directly to controlled voltage sources, whose outputs pass through the filter inductors L_1, L_2, L_3. This defines the current dynamics according to Equation 3.3:

$$L\frac{di}{dt} = v_{inv} - v_{bus} \tag{3.3}$$

Instead of simulating semiconductor switching, the inverter outputs the phase voltages V_a, V_b, and V_c directly through controlled voltage sources. The approach preserves the fundamental AC behavior required for controller development while significantly reducing the computational burden.

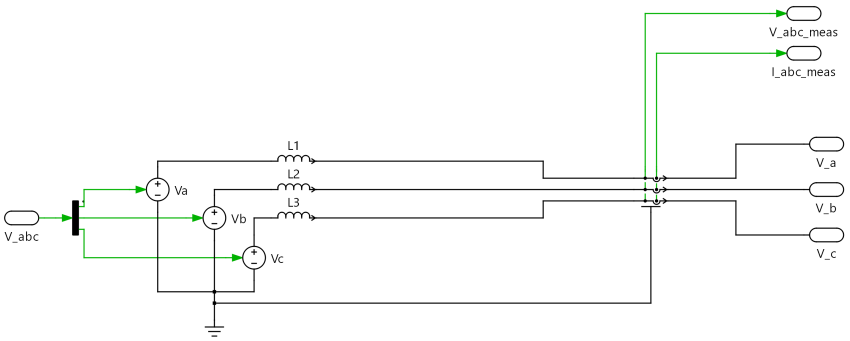

Figure 3.3. The averaged inverter topology used for all three inverters (PV, WT, Battery in PLECS

The resulting terminal voltages and currents are measured and provided as feedback signals:

- V_{abc} are the measured inverter output voltages
- I_{abc} are the measured inverter output currents

3.2.1 Grid Model

The AC grid is represented by its Thevenin equivalent as seen from the Point of Common Coupling (PCC). Per phase, the grid is modeled as an ideal voltage source V_g in series with an equivalent impedance $Z_g = R_g + j\omega L_g$, which emulates the distribution network and transformer [52].

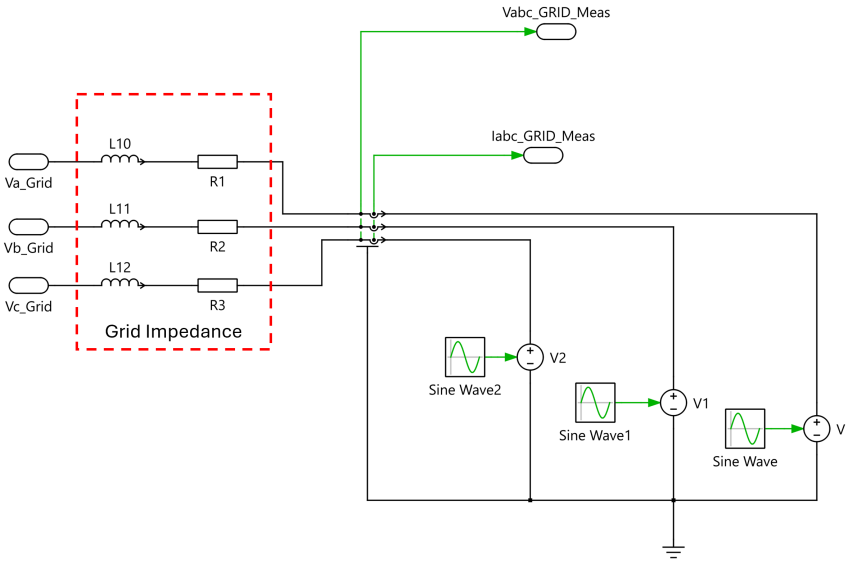

Figure 3.4. Phase-shifted Sinusoidal Ideal Voltage sources used to model the grid with grid impedance

This simplification aims to emulate a stiff grid, i.e., a grid whose terminal voltage remains practically constant despite power injections or withdrawals from the converter under study. From a physical point of view, the grid is "stiff" when its short-circuit capacity at the point of common coupling (PCC) is much larger than the rated power of the converter. This assumption is common in the analysis and design of grid-connected converters, as it decouples the control design from large-scale network dynamics and allows focusing on the local behavior of the converter and its filters.

Per-Phase Thevenin Equivalent

For one phase, the Thevenin equivalent is:

$$V_g = R_g I_g + L_g \frac{dI_g}{dt} + V_{\text{PCC}}, \tag{3.4}$$

where:

- V_g is the grid phase voltage,
- I_g is the grid current (equal to i_{PCC}),
- V_{PCC} is the phase voltage at the PCC.

In steady state, the magnitude of Z_g is related to the short-circuit capacity of the grid. A common indicator of grid strength is the short-circuit ratio (SCR):

$$\text{SCR} = \frac{S_{\text{sc}}}{S_{\text{rated}}}, \tag{3.5}$$

where S_{sc} is the three-phase short-circuit power at the PCC and S_{rated} is the rated apparent power of the inverter.

Symmetrical Three-Phase Representation

For many analyses, the grid can be idealized as a perfectly balanced three-phase system. The phase-to-neutral voltages are then:

$$v_{an}(t) = V\cos(\omega t), \tag{3.6}$$

$$v_{bn}(t) = V\cos\left(\omega t - \frac{2\pi}{3}\right), \tag{3.7}$$

$$v_{cn}(t) = V\cos\left(\omega t + \frac{2\pi}{3}\right), \tag{3.8}$$

and the line-to-line voltages :

$$v_{ab} = v_{an} - v_{bn}, \tag{3.9}$$

$$v_{bc} = v_{bn} - v_{cn}, \tag{3.10}$$

$$v_{ca} = v_{cn} - v_{an}. \tag{3.11}$$

Similarly, the phase currents can be written as:

$$i_a(t) = I\cos(\omega t), \tag{3.12}$$

$$i_b(t) = I\cos\left(\omega t - \frac{2\pi}{3} + \varphi\right), \tag{3.13}$$

$$i_c(t) = I\cos\left(\omega t + \frac{2\pi}{3} + \varphi\right), \tag{3.14}$$

where I is the current amplitude and φ is the phase angle between voltage and current.

dq-Frame Grid Equations

In the synchronous dq frame aligned with the grid voltage [53, 48], the grid model can be written as:

$$v_{\mathrm{PCC},d} = v_{g,d} - R_g i_{\mathrm{PCC},d} + \omega L_g i_{\mathrm{PCC},q}, \tag{3.15}$$

$$v_{\mathrm{PCC},q} = v_{g,q} - R_g i_{\mathrm{PCC},q} - \omega L_g i_{\mathrm{PCC},d}. \tag{3.16}$$

For ideal PLL alignment, the grid voltage in dq coordinates becomes:

$$v_{g,d} = V_g, \qquad v_{g,q} = 0. \tag{3.17}$$

Using this, the instantaneous active and reactive power per phase can be expressed in the dq frame as:

$$p = \frac{3}{2}\big(v_d i_d + v_q i_q\big), \qquad q = \frac{3}{2}\big(v_q i_d - v_d i_q\big), \tag{3.18}$$

which simplifies further when $v_q = 0$.

These expressions are later used in the active and reactive power control loops.

3.2.2 Average Model Filter Design

Power converters are connected to the grid through an output filter whose main purposes are:

- to attenuate switching harmonics,
- to limit the current ripple,
- to ensure that the injected current meets grid quality requirements.

This subsection presents the modeling and design considerations for both structures, including the effects of parasitic resistances in the inductors.

L-Filter Model

In average model analyses, it is sufficient to approximate the filter as a pure series inductance L_f with parasitic resistance R_f. However, it typically requires a relatively large inductance to achieve acceptable attenuation of switching ripple. This increases the voltage drop across the filter, reduces available dynamic range for current control, and increases physical size and cost. At the same time, there are also resistive components to the capacitor and to the inductor, which introduce thermal losses and slightly improve the damping of high-frequency components.

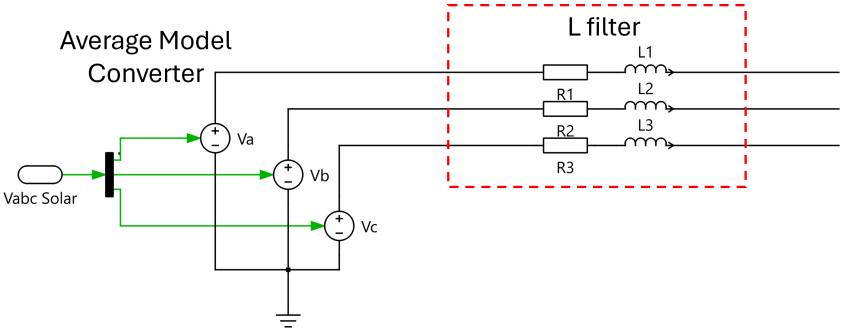

Figure 3.5. L filter with parasitic resistance used in Average Modeled Inverter

The phase-domain relation for the L filter is:

$$v_{k,\text{inv}} - v_{k,\text{PCC}} = R_f i_k + L_f \frac{di_k}{dt}, \tag{3.19}$$

where $v_{k,\text{inv}}$ is the inverter output phase voltage, $v_{k,\text{PCC}}$ is the phase voltage at the point of common coupling, and i_k is the phase current.

The transfer function from the inverter output voltage e_{dq} to the injected current $i_{\text{PCC},dq}$ is then:

$$G_{\text{plant}}(s) = \frac{i_{\text{PCC},dq}(s)}{e_{dq}(s) - v_{\text{PCC},dq}(s)} = \frac{1}{R_f + sL_f}, \tag{3.20}$$

which reduces to $1/(sL_f)$ when R_f is neglected, as commonly done for current loop design [52, 51]

3.3 Switched Inverter Model

To validate the averaged-model controller under realistic switching behavior, a switched inverter model is developed. This model has the same topology as the averaged model, with a few additions, which include:

- Modeling of a three-phase inverter with IGBT switching devices, free-wheeling diodes
- LCL filters
- PWM

This representation captures harmonics and switching dynamics, creating voltage and current ripples needed for realistic laboratory validation.

While the averaged inverter model presented in section 3.2 is well suited for control design and system-level studies, it does not capture switching dynamics, harmonics, or PWM-related phenomena. To support laboratory implementation and to validate the averaged-model controller under realistic conditions, a switched three-phase inverter model is developed in PLECS/Simulink.

3.3.1 Two-Level Three-Phase VSI Topology

The basic power circuit of the two-level three-phase VSI is shown conceptually in Figure 3.6. Each phase leg consists of an upper and a lower switch in a half-bridge configuration. The midpoint of each leg is connected to one phase of the three-phase reactor. The DC-link voltage is denoted by v_{DC} and is assumed to be supported by a capacitor of value C, where V_{dc} is the DC Link voltage, and 1 through 6 are the gating signals that are generated from the PWM Switching Block.

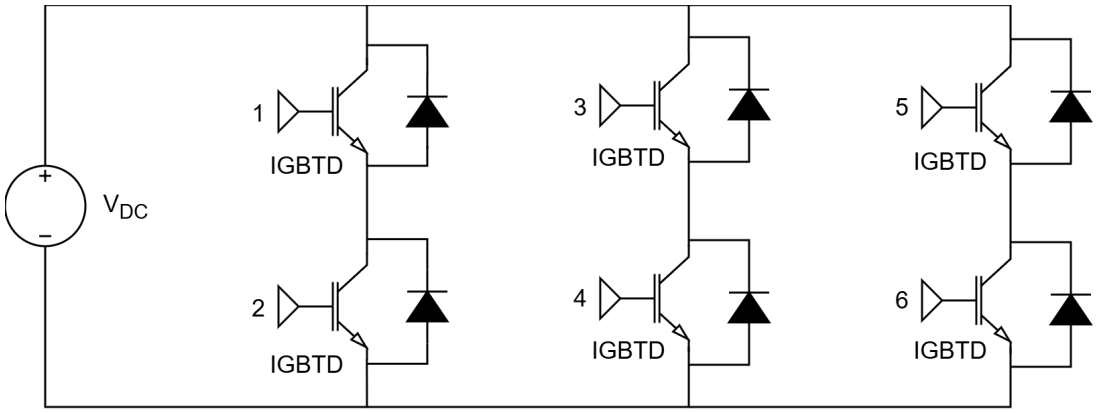

Figure 3.6. The switched two-level Three-Phase VSI Topology visualized

Under standard assumptions:

- balanced three-phase system with a neutral connection,
- identical phase filter impedance with inductance L and resistance R,
- negligible on-state resistance of the semiconductor devices.

The averaged phase-domain model of the two-level VSI is

$$C\frac{dv_{DC}}{dt} = \sum_{k=1}^{3} i_k d_k - i_{DC}, \tag{3.21}$$

$$L\frac{di_k}{dt} + Ri_k = e_k - v_{DC}\left(d_k - \frac{1}{3}\sum_{n=1}^{3} d_n\right), \tag{3.22}$$

$$\sum_{k=1}^{3} i_k = 0, \qquad \sum_{k=1}^{3} e_k = 0, \tag{3.23}$$

where:

- $k \in \{a, b, c\}$ is the phase index,
- i_k is the phase current,
- e_k is the inverter-side phase voltage,
- $d_k \in [0, 1]$ is the duty cycle of leg k,
- i_{DC} is the DC-link current.

For an ideal two-level leg, the instantaneous phase-to-negative-DC-bus voltage v_{kN} takes only two levels:

$$v_{kN} \in \left\{-\frac{v_{DC}}{2}, +\frac{v_{DC}}{2}\right\}, \tag{3.24}$$

The linearized averaged model uses the duty cycle d_k to represent the fraction of the PWM period spent in each switching state.

3.3.2 dq-Frame Model of the Two-Level VSI

To align the electrical variables with the control structure, the three-phase states are transformed to the synchronous dq reference frame using Clarke–Park transformations. The d-axis is chosen to coincide with the fundamental grid voltage vector [52].

Applying the transformation to (3.21)–(3.22) and grouping the terms yield the following dynamics in the dq frame:

$$C\frac{dv_{DC}}{dt} = \frac{3}{2}\big(i_d d_d + i_q d_q\big) - i_{DC}, \tag{3.25}$$

$$L\frac{di_d}{dt} - \omega L i_q + R i_d = e_d - v_{DC} d_d, \tag{3.26}$$

$$L\frac{di_q}{dt} + \omega L i_d + R i_q = e_q - v_{DC} d_q, \tag{3.27}$$

where ω is the grid angular frequency and i_d, i_q, are the dq components of the inverter output current and e_d, e_q, are the dq components of the corresponding three-phase grid voltage. [48, 54]. The variables d_d, d_q, denote the d- and q-axis components of the modulation vector in the synchronous reference frame. They satisfy

$$-1 \leq d_d, d_q \leq 1,$$

And relate the converter AC-side voltages to the DC-link voltage by

$$v_d = v_{DC} d_d, \qquad v_q = v_{DC} d_q.$$

The cross-coupling terms $\pm\omega L i_{q,d}$ arise from the transformation to the rotating frame. These terms do not originate from new physical couplings in the hardware. They arise due to the rotating coordinate system of the Park transformation.

3.3.3 Sinusoidal PWM Switching Strategy

In this section, the switching signals for the three-phase two-level inverter are derived using a Sinusoidal Pulse-Width Modulation (SPWM) scheme. The goal of the PWM block is to translate the output of the current controller into an actual gate signals for the inverter switches, while ensuring modulation remains within the linear operating range and respects the available DC-link voltage.

Reference Voltages From the Current Controller

The inner current controller operates in the synchronous dq reference frame and produces the commanded converter output voltages:

$$v_a, v_b, v_c$$

These voltages are the values required at the inverter's AC terminals to track the desired d- and q-axis currents generated by the power controller.

Normalization With Respect to the DC-Link Voltage

A two-level inverter can only output voltages constrained by the DC-link voltage; reference voltages must be normalized to ensure they remain within the modulation limits. This is done by dividing each phase voltage reference by half of the DC-link voltage,

$$m_a = \frac{v_a^*}{v_{DC}/2}, \qquad m_b = \frac{v_b^*}{v_{DC}/2}, \qquad m_c = \frac{v_c^*}{v_{DC}/2}.$$

The quantities m_a, m_b, and m_c are the modulation indices, and by construction they satisfy

$$-1 \leq m_{a,b,c} \leq 1,$$

This keeps the modulation strictly inside the linear SPWM region. For the model, an ideal DC source is used; however, this scaling strategy ensures that any DC-link voltage variations are naturally accounted for, as the normalization automatically scales the modulation depth [55].

Carrier Comparison and Generation of Switching Pulses

To generate the actual gate signals, a high-frequency triangular carrier signal $v_{\text{tri}}(t)$ with switching frequency f_s is used. Each modulation index is compared against this carrier,

$$m_x(t) \gtrless v_{\text{tri}}(t), \qquad x \in \{a, b, c\},$$

And the result of this comparison directly determines the switching state of the upper IGBT of that phase,

$$S_{x,\text{upper}}(t) = \begin{cases} 1, & m_x(t) \geq v_{\text{tri}}(t), \\ 0, & m_x(t) < v_{\text{tri}}(t). \end{cases}$$

The complementary signal drives the lower switch in each leg,

$$S_{x,\text{lower}}(t) = 1 - S_{x,\text{upper}}(t).$$

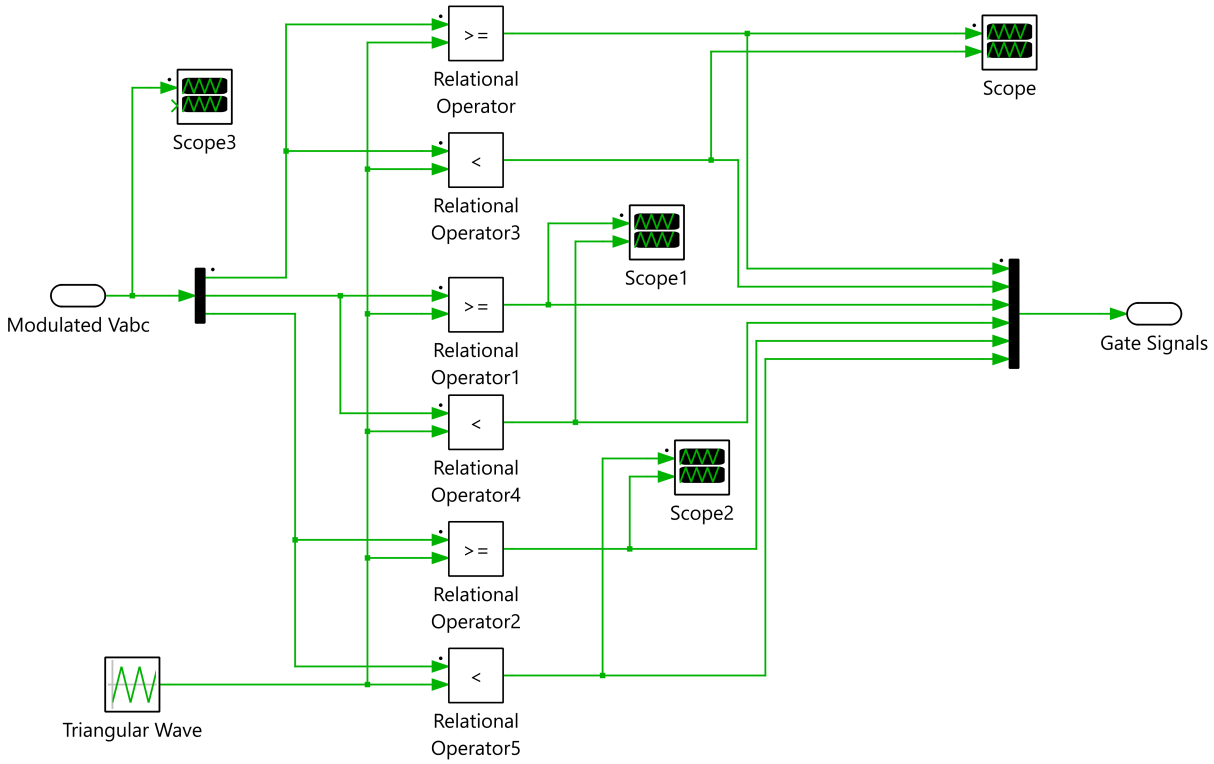

Figure 3.7. Circuit Diagram Implementation of Sin PWM in PLECS

This SPWM method, which has been shown inFigure 3.7 keeps the switching frequency constant at 10 kHz and places the dominant harmonics around the switching frequency and its multiples, thereby simplifying filter design. Since the modulation indices come directly from the current controller (scaled by the DC-link voltage), the inverter output voltage closely follows the commanded values, ensuring accurate and fast current tracking [55, 54].

3.3.4 Switched Model Filter Model and Design

Since the switched model is being implemented, additional switching harmonics are present in the output current and voltage waveforms of both the two-level and three-level inverters. From this point onward in the text, all design considerations according to the two-level inverter are assumed.

The inverter is connected to the grid through an output filter whose main purposes are:

- to attenuate switching harmonics,
- to limit the current ripple,
- to ensure that the injected current meets grid quality requirements.

In grid-connected switched power converters, the most common filter choice is the higher-

order LCL filter, which consists of an additional Shunt Capacitor and a damping resistor in parallel, followed by a grid-side transformer inductance modeled as another inductor in series [56, 57]. This section presents the modeling and design considerations for both structures, including the effects of parasitic resistances in the inductors. As shown in Figure 3.8, the LCL filter is implemented with parasitic resistances in series with the inverter-side and grid-side inductances, and damping resistors in series with the shunt capacitance.

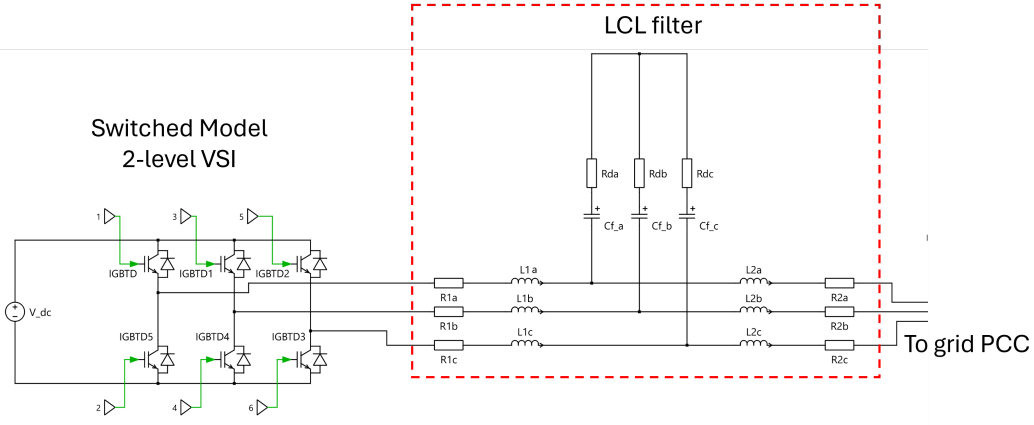

Figure 3.8. Circuit Diagram Implementation of LCL filter in PLECS

A three-phase representation of one filter branch is:

$$v_{k,\text{inv}} - v_{k,c} = R_1 i_{k,1} + L_1 \frac{di_{k,1}}{dt}, \tag{3.28}$$

$$i_{k,c} = i_{k,2} - i_{k,1}, \tag{3.29}$$

$$v_{k,c} - v_{k,\text{PCC}} = R_2 i_{k,2} + L_2 \frac{di_{k,2}}{dt}, \tag{3.30}$$

where:

- $v_{k,c}$ is the capacitor voltage,
- $i_{k,1}$ is the inverter–side inductor current,
- $i_{k,2}$ is the grid–side inductor current,
- $i_{k,c}$ is the capacitor current.

3.3.5 dq-Frame Model of the LCL-Type Filter

The per-phase circuit of the filter is illustrated in the original work as a reactor in series with the inverter, a capacitor to ground, and the transformer leakage inductance on the grid side [52]. Neglecting the capacitor ESR, the three-phase model is:

$$C_f \frac{de_k}{dt} = i_{c,k}, \tag{3.31}$$

$$i_{c,k} = i_{\mathrm{PCC},k} - i_k, \tag{3.32}$$

where:

- e_k is the phase voltage across the capacitor (PCC voltage),
- i_k is the inverter-side inductor current,
- $i_{\mathrm{PCC},k}$ is the current injected into the grid,
- $i_{c,k}$ is the capacitor current.

Transforming to the synchronous dq frame and separating the components gives:

$$C_f \frac{de_d}{dt} = \omega C_f e_q + i_{c,d}, \tag{3.33}$$

$$C_f \frac{de_q}{dt} = -\omega C_f e_d + i_{c,q}, \tag{3.34}$$

$$i_{c,d} = i_{\mathrm{PCC},d} - i_d, \tag{3.35}$$

$$i_{c,q} = i_{\mathrm{PCC},q} - i_q. \tag{3.36}$$

Equations (3.33)–(3.36) represent the dynamic behavior of the filter capacitor in the dq frame and are used later in the AC voltage control loop design.

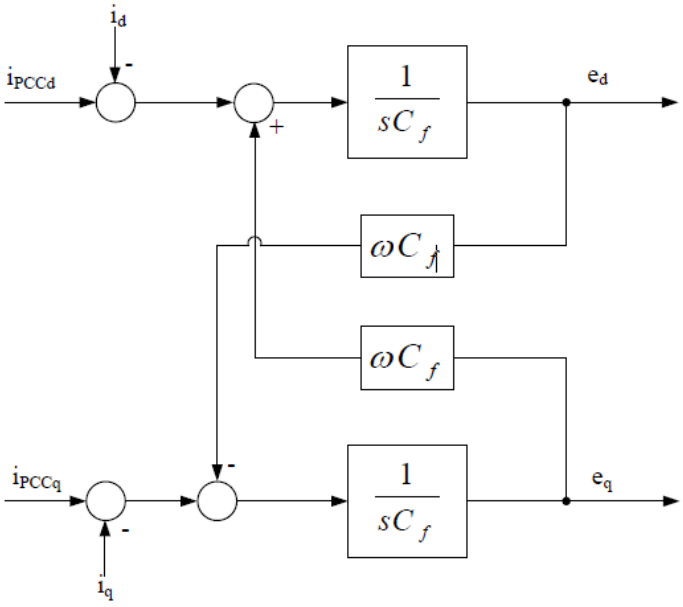

Figure 3.9. This model shows the implementation of the C type filter in dq reference frame

There is a sharp resonance peak caused by the interaction of L_1, L_2, and C_f, which might lead to potential instability of the current controller. A common approach is to add a damping resistor R_d in series with the filter capacitor [56, 48]. The impedance of the capacitor branch becomes

$$Z_C(s) = R_d + \frac{1}{sC_f}. \tag{3.37}$$

Including R_d in the undamped LCL characteristic equation modifies the resonant dynamics. Neglecting resistances R_1 and R_2 for clarity, the corresponding characteristic polynomial simplifies to

$$L_1 L_2 C_f \, s^3 + R_d(L_1 + L_2)C_f \, s^2 + (L_1 + L_2)s + 1 = 0. \tag{3.38}$$

The natural (undamped) resonance frequency remains

$$\omega_{\text{res}} = \sqrt{\frac{L_1 + L_2}{L_1 L_2 C_f}}, \tag{3.39}$$

but the inclusion of R_d introduces a damping factor

$$\zeta_{\text{LCL}} = \frac{R_d}{2}\sqrt{\frac{C_f(L_1 + L_2)}{L_1 L_2}}. \tag{3.40}$$

Thus, R_d directly scales the damping ratio while leaving the resonant frequency almost unchanged.

3.4 Control Structure for Switched Inverter

This section presents the control strategy used to regulate the grid power following the inverters in the microgrid. The section is divided into two parts.

In the first part, based on the averaged inverter model and the theoretical groundwork introduced earlier, the controller for the averaged model is developed. Emphasis is placed on dq-current control and active-power control, implemented through nested control loops. This section also introduces the transfer functions used to tune the averaged plant model, as well as the filter and associated auxiliary blocks.

In the second part, the adaptation of the same control principles to the switched model is discussed. The design implications of transitioning from an averaged model to a switched model are considered, and the effects on the controller are examined.

3.4.1 Controller for the Averaged Model

The control strategy implemented in the averaged inverter model follows the widely used grid-following control architecture for renewable energy converters [58, 48, 59].

The control strategy for the grid-following converter consists primarily of two cascaded loops. Usually, there is a fast internal current loop, which regulates the inverter current

feeding to the grid and is responsible for the power quality, and an external power loop, which controls the active power flow between the inverter and the grid PCC. The design of this outer control loop is intended to ensure system stability and exhibits slow dynamics.

In a grid-following inverter, the AC bus voltage sets the grid frequency and phase, while the inverter adjusts its injected active and reactive power. This structure is well-suited to the microgrid in this project, in which the PV, WT, and battery inverters (when operating in grid-following mode) synchronize with the AC bus.

The overall controller structure is visualized in Figure 3.10.

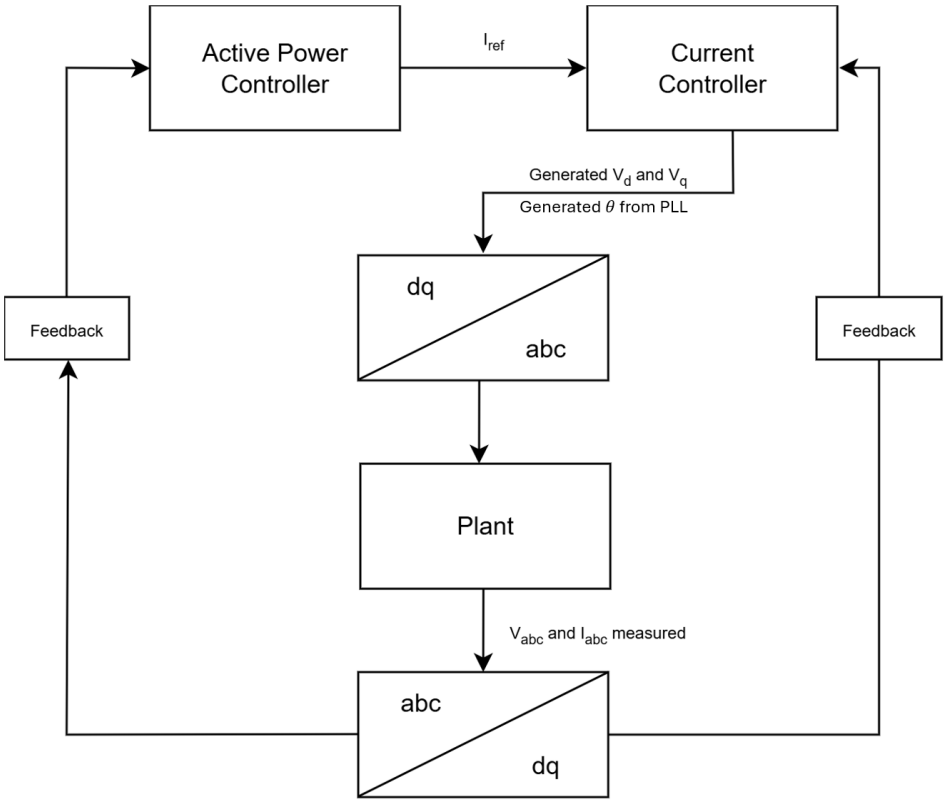

Figure 3.10. Overall control structure of the average model inverter[58].

Reference Frame Transformations

The first component of the controller is the Clarke-Park transformation. The Simulink block converts the natural-reference-frame signals directly to the dq components, as shown in Figure 3.11. This enables simplified control design and complete decoupling of active and reactive power.

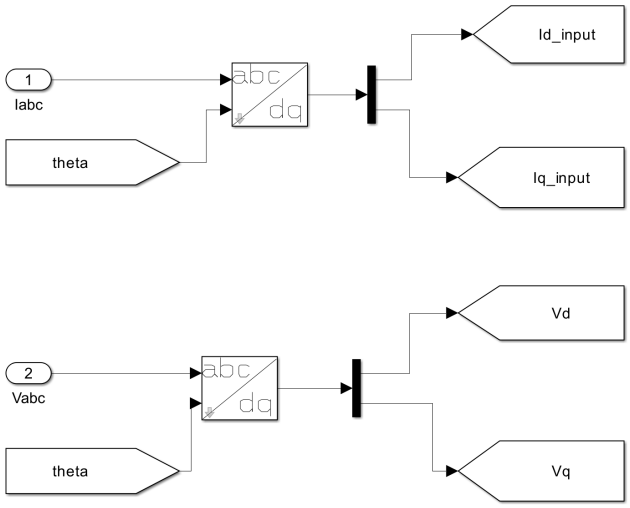

Figure 3.11. The abc to dq transformation applied in Simulink

Linear PI Controller

PI controllers are used extensively in this work, as they provide a simple yet highly effective means of regulating electrical quantities once they are transformed into the synchronous rotating reference frame (SRF). A PI controller combines a proportional term, which responds instantaneously to the control error, with an integral term, which eliminates steady-state offset. In power-electronic systems, this structure is generally sufficient to achieve accurate tracking of currents, voltages, or frequency without introducing unnecessary complexity. The output response of the PI controller is shown below:

$$u(t) = K_p\, e(t) + K_i \int_0^t e(\tau)\, d\tau, \tag{3.41}$$

where $e(t)$ is the difference between the reference and the measured quantity.

This structure is simple to implement, computationally inexpensive compared with easy-to-tune alternatives, and highly effective when the controlled variable is a time-invariant signal.

PI Controller in the dq–Frame

In the dq reference frame, PI controllers are typically used because they provide stable and accurate regulation of quantities that become DC in steady state. When expressed in dq coordinates, the controller can be represented by the following matrix transfer function:

$$G_{\mathrm{PI}}^{(dq)}(s) = \begin{bmatrix} K_p + \dfrac{K_i}{s} & 0 \\ 0 & K_p + \dfrac{K_i}{s} \end{bmatrix}, \tag{3.42}$$

where K_p denotes the proportional gain and K_i is the integral gain of the controller.

Phase Locked Loops (PLL)

In an inverter-based microgrid, maintaining a stable synchronisation of voltage, frequency, and phase between converters is vital. A PLL is the control mechanism that tracks the electrical phase angle and frequency of the system, enabling each inverter to align with the shared AC bus or grid reference. The PLL is a closed-loop feedback system that locks the phase of its internal oscillator to that of a reference signal [60].

Working Methodology

The basic principle of a PLL is to use a feedback loop to synchronize the inverter output with the grid voltage. In this loop, the estimated phase angle (θ') is generated by using a PI controller to regulate $\Delta\theta$ to zero, combined with an integrator that converts rotational speed to phase angle, as indicated in (3.43):

$$\theta' = \int \left(\omega_{\text{nom}} + K_p \, \Delta\theta + K_i \int \Delta\theta \, dt \right) dt \tag{3.43}$$

Where ω_{nom} is the nominal grid frequency, K_p and K_i are the proportional and integral gains of the PI controller, respectively, and $\Delta\theta$ is the phase difference between the grid voltage θ_{grid} and the inverter estimated phase angle by the PLL, θ'. The PLL adjusts the phase angle to minimise $\Delta\theta$, ensuring synchronisation with the grid. Once locked, the PLL ensures that the output oscillator's phase tracks the reference, minimising phase error and keeping the inverter's output synchronised with the grid or microgrid bus. When the system is in steady state and locked, the loop nodes are equal in phase and frequency between reference and feedback [60].

The overall PLL interaction with the inverter control system is illustrated in Figure 3.10, where the estimated phase angle, θ, is supplied to the transformations[61]. The PLL implemented in this project is an SRF-PLL, where the q-axis component of the grid voltage, v_q, is regulated to zero. When the rotating frame is aligned with the grid voltage vector, the q-axis component becomes zero, making v_q a natural phase-error signal. A digital PI controller processes this error, and the resulting output is added to a nominal feed-forward term ($100\pi \frac{rad}{s}$) to construct the estimated angular frequency. Integrating this frequency yields the instantaneous phase angle, θ, which is wrapped to the range 0 to 2π to avoid numerical drift.

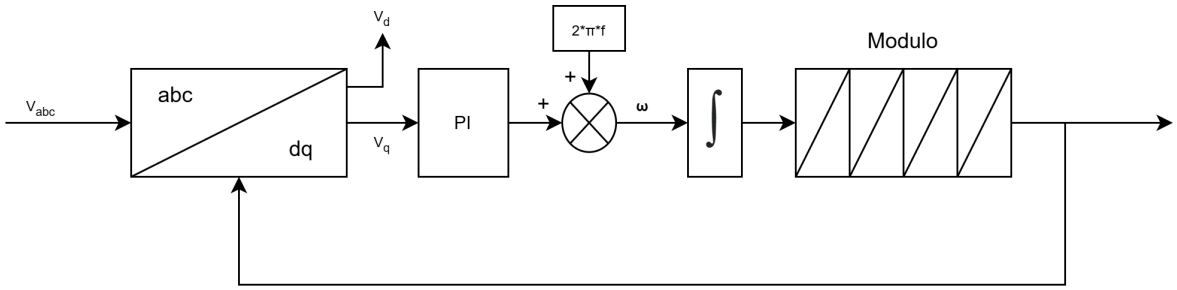

Figure 3.12. Block diagram of PLL

Figure 3.12 shows the implemented dq-PLL subsystem from the Simulink model used in the project. The block diagram closely follows the classical PLL structure described in [58] and includes the phase-detector stage, PI regulator, frequency feedforward term, and numerical integration for angle generation.

In the PLL implementation with the q-axis voltage error as an input to the PLL loop filter, the dynamic relationship between the phase angle error and the estimated angle can be represented as a second-order system with an additional zero arising from the PI controller. The closed-loop PLL transfer function can be written as

$$H_{\text{PLL}}(s) = \frac{k_p s + k_i}{s^2 + k_p s + k_i}, \tag{3.44}$$

where k_p and k_i denote the proportional and integral gains of the PLL's PI controller, respectively.

This form matches the standard representation of a second-order system with a real zero:

$$G_{\text{2nd}}(s) = \frac{2\zeta\omega_n s + \omega_n^2}{s^2 + 2\zeta\omega_n s + \omega_n^2}, \tag{3.45}$$

where ω_n is the natural frequency and ζ is the damping ratio.

Equating coefficients from both expressions yields explicit expressions for the PLL gains:

$$k_p = 2\zeta\omega_n, \qquad k_i = \omega_n^2. \tag{3.46}$$

Selection of Natural Frequency and Damping

The choice of ω_n and ζ determines the transient behavior of the PLL. The value of ω_n is 50Hz as we are dealing with a grid-connected inverter. A typical engineering choice is a damping ratio of $\zeta \approx 0.7$, which provides a balance between speed and overshoot.

The desired settling time T_{set} of the PLL turns out to be around 0.112s.

Once ω_n and ζ are selected, the PLL's PI gains follow immediately from

$$k_p = 70, \qquad k_i = 2500. \tag{3.47}$$

This tuning procedure provides a transparent, purely analytical method for determining PLL parameters, ensuring a well-damped, predictable synchronization response without relying on trial-and-error[61].

3.4.2 Inner Control Loop - Current Controller

The current controller regulates the inverter output currents in the synchronous reference frame. Once the PLL has aligned the reference frame with the AC Bus voltage, the measured phase currents from the measuring meter ahead of the filter are transformed into i_d and i_q. The purpose of the current controller is to ensure that the inverter currents track their reference values $i_d^\star$ and $i_q^\star$, generated by the power controller.

The current controller will be implemented as a PI controller with d- and q-axis decoupling. The controller is based on the dynamic model of the inverter-side inductor expressed in the synchronous frame as seen in Equation 3.48

$$\begin{aligned} L\frac{di_d}{dt} &= v_d - v_{\text{bus},d} + \omega L i_q, \\ L\frac{di_q}{dt} &= v_q - v_{\text{bus},q} - \omega L i_d. \end{aligned} \tag{3.48}$$

where:

- v_d, v_q are the inverter reference voltages.
- $v_{bus,d}$, $v_{bus,q}$ are the bus voltages in the synchronous frame.
- L is the filter inductance.
- ω is the estimated grid angular frequency from the PLL.

The terms $\omega L i_q$ and $-\omega L i_d$ represent cross-coupling between the d- and q-axis dynamics [48, 59]. To improve controller performance, these terms are included as feed-forward decoupling, allowing each PI-regulator to control its axis independently. The resulting control law can be written as shown in Equation 3.49

$$\begin{aligned} v_d^\star &= v_{bus,d} + \omega L i_q + K_p(i_d^\star - i_d) + K_i \int (i_d^\star - i_d)dt, \\ v_q^\star &= v_{bus,q} - \omega L i_d + K_p(i_q^\star - i_q) + K_i \int (i_q^\star - i_q)dt. \end{aligned} \tag{3.49}$$

These voltages represent the inverter's desired output voltages in the synchronous frame. They are transformed back to the natural reference frame using inverse Park and Clarke

transformations to generate the three-phase voltage references. After saturation and limiting to respect inverter modulation constraints, they are passed through $dq \rightarrow abc$ transformation to generate the three-phase reference voltages $v^{\star}_{abc}$ for the averaged model.

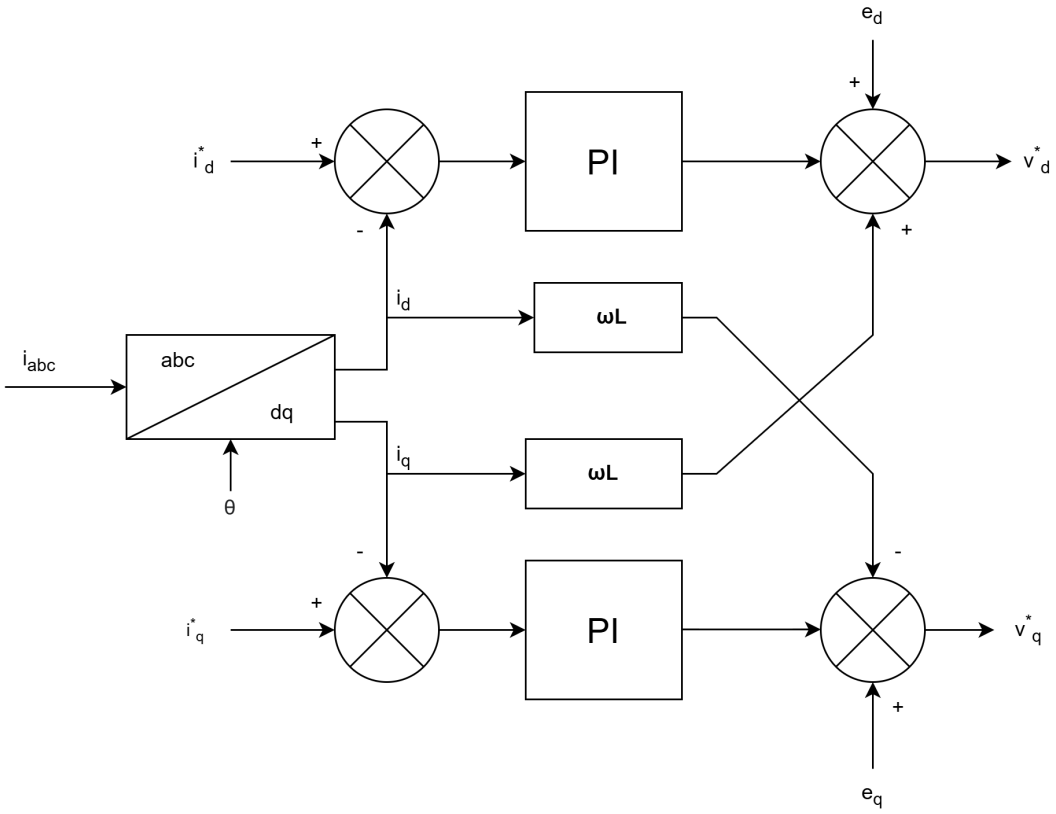

Figure 3.13. The structure of the inner current controller implemented in synchronous reference frame.

The implemented dq-controller used in the Simulink model is shown in Figure 3.13 as a control block diagram. The current controller forms the inner loop of the inverter control system. By using a PI controller, the dq currents can be regulated directly, which ensures a fast dynamic response, accurate active and reactive power injection, robustness against bus-voltage disturbances, proper decoupling between axes, and stable operation under varying load conditions. The output of the current controller, $v^{\star}_{dq}$, is transformed back to the abc frame and applied to the averaged inverter as the modulation reference.

3.4.3 Adapting to Switched Plant Dynamics

While the averaged model provides a simplified representation of the inverter dynamics suitable for controller design and conceptual validation, the switched model introduces several non-ideal and high-frequency phenomena. In the averaged inverter model, the semiconductor switching is abstracted away and replaced by a controlled voltage source

applied directly to the filter inductors. This results in smooth dynamic system parameters. However, the switched model includes the following additional elements:

- **Switching delay/PWM sampling delay:**
  The voltage applied to the filter is not instantaneous; it is updated once per PWM cycle. This introduces an effective delay that reduces phase margin.
- **LCL filter effects:**
  The output filter now contains additional switching harmonics and ripples that must be filtered out, and a simple inductive filter no longer suffices. Additional capacitive filtering is required to ensure that the inverter output voltage exhibits low THD despite using a 2-level switched VSI.

3.4.4 Determining Transfer Function of Current Controller

The design of the inner current controller begins with the development of a small-signal transfer function that relates the inverter's commanded voltage to the resulting inductor current. The inner current control loops for the d- and q-components have identical dynamics. Thus, the current controllers are tuned only for the d-axis, and the q-axis controller parameters are assumed equal to those for the d-axis. The current control block diagram is presented in Figure 3.13. As it can be observed, the decoupling between the d-axis and the q-axis, as well as the voltage feed forward, have been neglected as they were considered disturbances in the system, instead of the simple first-order relation.

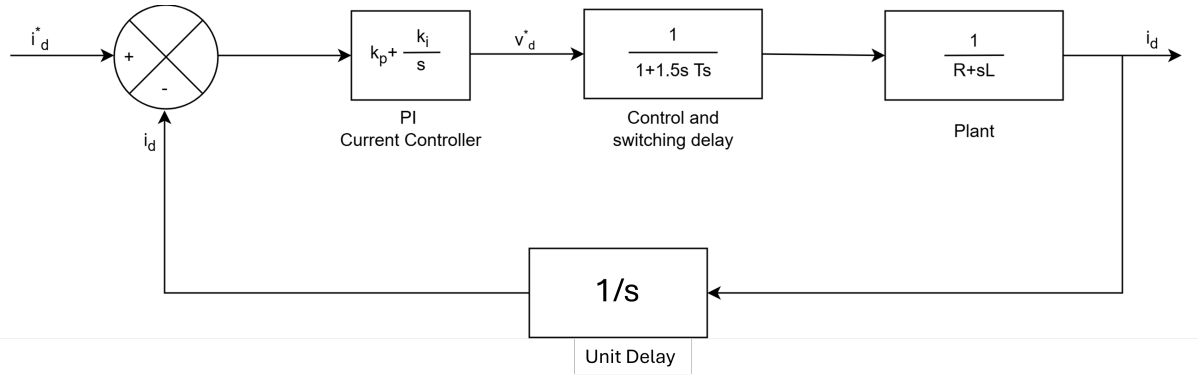

Figure 3.14. Block diagram representing the transfer function of the Closed Loop Current Controller

Plant and Filter

In an average-model converter, the inverter current and voltage upstream of the inverter-side inductive filter were measured. Then, the inverter is connected to the grid through a single series inductance, L, with parasitic resistance, R.

Under small-signal conditions, the transfer function relating the inverter voltage to the inductor current is

$$G_{i,L}(s) = \frac{i_d(s)}{v_{d,\text{inv}}(s)} = \frac{1}{Ls + R}. \tag{3.50}$$

where $v_{d,\text{inv}}$ is the voltage reference generated by the current controller and i_d is the d-axis current.

As previously mentioned, the switched model needs additional filtering to smooth out the voltage and current ripples from switching. Therefore, while measuring the current ahead of the grid side inductor, an LCL filter can be used, consisting of an inverter-side inductor, L_1, with resistance, R_1, a shunt capacitor, C_f, and a grid-side inductor, L_2, with resistance, R_2.

Transforming these equations into the Laplace domain yields the small-signal transfer function from inverter voltage to inverter-side current:

$$G_{i,LCL}(s) = \frac{i_1(s)}{v_{\text{inv}}(s)} = \frac{L_2 s + R_2}{(L_1 s + R_1)(L_2 s + R_2)C_f s + L_1 s + R_1}. \tag{3.51}$$

Using an L-Filter Approximation for PI Tuning in Switched Model Inverters

For the inner current loop, the exact plant with an LCL filter is of the third order. The transfer function from inverter voltage to inverter–side current can be written as Equation 3.51. From this equation, the resonance frequency of the LCL filter can be calculated, which is given by exhibiting

$$\omega_{\text{res}} = \sqrt{\frac{L_1 + L_2}{L_1 L_2 C_f}}, \qquad f_{\text{res}} = \frac{\omega_{\text{res}}}{2\pi}. \tag{3.52}$$

For the parameters

$$L_1 = 5 \text{ mH}, \quad L_2 = 1 \text{ mH}, \quad C_f = 4.8 \ \mu\text{F}, \quad R_d = 0.1 \ \Omega,$$

was obtained

$$f_{\text{res}} \approx 2.51 \text{ kHz},$$

which is far above the fundamental frequency of 50 Hz and also above the desired bandwidth of the current loop [56, 48]. If the main resonance is modeled as a second–order mode with equivalent inductance

$$L_{\text{eq}} = \frac{L_1 L_2}{L_1 + L_2},$$

a simple estimate of the damping ratio with a series damping resistor R_d in the capacitor branch is

$$\zeta \approx \frac{R_d}{2}\sqrt{\frac{C_f}{L_{\text{eq}}}} \approx 2.6 \times 10^{-4}, \tag{3.53}$$

which confirms that the resonance is sharp but confined to a narrow band around f_{res}.

At much lower frequencies (around 50 Hz), the capacitor current is negligible, and the grid–side inductance hardly affects the inverter–side current dynamics. In this range, the LCL plant seen by the current controller reduces effectively to a first–order filter

$$G_{i,L}(s) \simeq \frac{1}{L_1 s + R_1}. \tag{3.54}$$

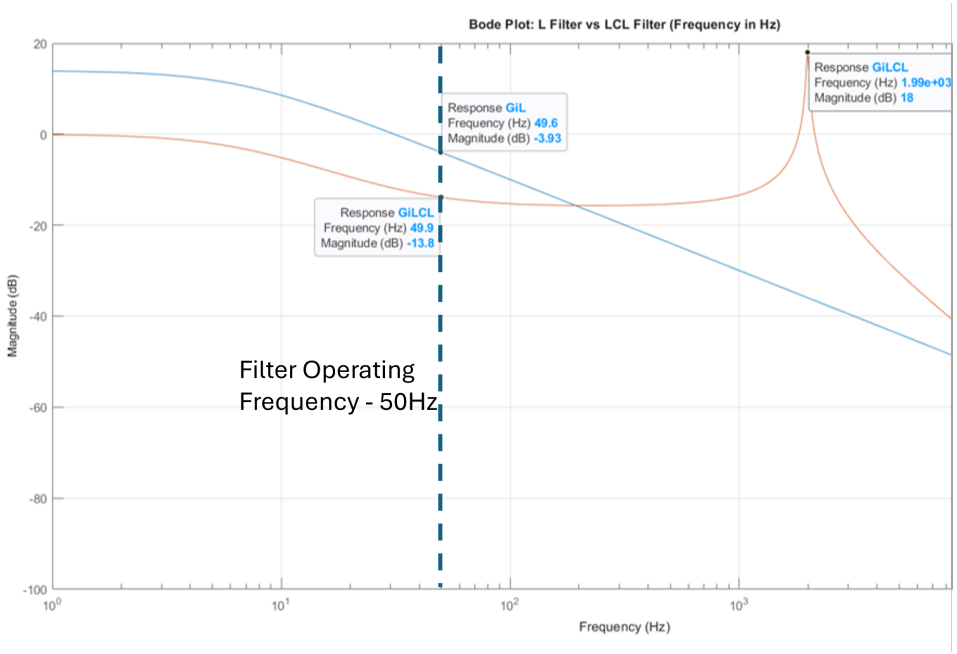

Figure 3.15. Bode Plot (Magnitude) of L filter and LCL Filter

As prevalent in Figure 3.15, it can be observed that the Bode plots of $G_{i,LCL}(s)$ and $G_{i,L}(s)$ almost have the same slope (-18.5 $\frac{dB}{dec}$) around 50 Hz: resulting in both the filters behaving as a single dominant pole. In other words, the third pole and the resonant peak of the LCL filter only become relevant close to f_{res}, well outside the frequency range where the current–loop bandwidth is placed. Because of this separation in frequency, the PI current controller can be tuned safely using the simpler L–filter model $G_{i,L}(s)$ without explicitly handling the full third–order LCL transfer function.

PI controller

The current controller block used for regulating the current is a PI controller with the transfer function given by:

$$G_{PI_c} = k_{p_c} + \frac{k_{i_c}}{s} \tag{3.55}$$

Delay due to Inverter Switching and Control Delay

The control and switching delay block emulates the delay introduced by the digital calculation; its transfer function is given by Equation 3.56, and it has the form of a first-order transfer function with the time constant $T_s = 1/f_s$:

$$G_{\text{control}} = \frac{1}{1 + 1.5sT_s} \tag{3.56}$$

where $f_s = 10$ kHz represents the sampling frequency.

Unit Sampling Delay

The sampling block emulates the delay introduced by the analog-to-digital conversion; its transfer function is given by Equation 3.57 and is first-order with a time constant of 0.5Ts.

$$G_{\text{sampling}} = \frac{1}{s} \tag{3.57}$$

Current Controller Overall Transfer Function

Having determined the individual transfer functions of the different blocks used in the forward gain path and the feedback loop. The closed-loop transfer function of the current controller can be determined now. For the inner current control loop, the gain is written in terms of the forward path gain $G(s)$ and the feedback path gain $H(s)$ as

$$L(s) = G(s)\,H(s). \tag{3.58}$$

The corresponding closed-loop transfer function from the current reference to the measured current is

$$T(s) = \frac{G(s)}{1 + G(s)\,H(s)}. \tag{3.59}$$

In this case, $H(s)$ represents the sampling and delay behaviour in the feedback path. This unit sampling delay block is approximated by

$$H(s) = \frac{1}{s}. \tag{3.60}$$

The forward path $G(s)$ is the product of the PI controller and the equivalent L–filter plant:

$$G(s) = G_{\text{PI}}(s)\,G_{\text{plant}}(s), \tag{3.61}$$

with

$$G_{\text{PI}}(s) = K_p + \frac{K_i}{s}, \qquad G_{\text{plant}}(s) = \frac{1}{R + Ls}. \tag{3.62}$$

Hence,

$$G(s) = \frac{K_p + K_i/s}{R + Ls} = \frac{K_p s + K_i}{s\,(R + Ls)}. \tag{3.63}$$

Substituting $G(s)$ and $H(s)$ into the closed-loop expression,

$$T(s) = \frac{G(s)}{1 + G(s)\,H(s)}, \tag{3.64}$$

after simplification, the closed-loop transfer function was obtained in terms of K_p, K_i, L and R:

$$T(s) = \frac{s\,(K_i + K_p s)}{Ls^3 + Rs^2 + K_p s + K_i}. \tag{3.65}$$

Using MATALB's Control System Designer to tune the Current Controller Gains

Having determined the equivalent transfer function for the current controller in Equation 3.65, the inner d-axis current controller is being tuned. For this, MATLAB's Control System Designer (SISOtool) was employed. This environment has enabled the construction of a custom control loop to suit the Overall closed-loop transfer Function by defining compensator and plant dynamics, a feedback-delay block, a reference-scaling gain to accommodate different values of the d-axis current, and iteratively tuning the controller using both frequency- and time-domain criteria.

The architecture selected in SISOtool is shown in Figure 3.16. The noise disturbances in the forward and feedback paths were not assumed while tuning the PI controller. Firstly the control architecture was edited so that the loop contained four blocks:

- the compensator $C(s)$,
- the plant $G(s)$,
- the feedback path $H(s)$,
- and an input scaling factor $F(s)$.

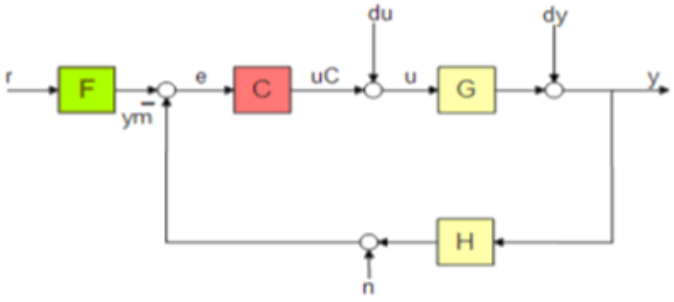

Figure 3.16. Control Loop Architecture Type used in SISOTool

The forward-path plant $G(s)$ consists of two cascaded transfer-function blocks as defined in Equation 3.62.

The plant used in SISOtool is therefore

$$G(s) = G_{\mathrm{LR}}(s)\, G_{\mathrm{controldelay}}(s) = \frac{1}{(R + Ls)(1 + 1.5\, sT_s)}. \tag{3.66}$$

The feedback block $H(s)$ represents the unit sampling delay introduced by discrete-time current measurement. This delay as defined in Equation 3.67 was approximated in Figure 3.14.

$$H(s) = \frac{1}{s} \tag{3.67}$$

The next step was to edit the compensator using the SISOtool Compensator Editor to make it identical to a PI controller by inserting:

- an integrator at $s = 0$,
- and a real zero at $s = -1/\tau$,

$$C(s) = K_p + \frac{K_i}{s} = K_p \left(1 + \frac{1}{s\tau}\right), \qquad K_i = \frac{K_p}{\tau}. \tag{3.68}$$

For the specific design shown in Figure 3.16, the compensator expression was

$$C(s) = 100\, \frac{1 + 0.025s}{s}, \tag{3.69}$$

hence, implying that the final Kp and Ki values are

$$K_p = 100 \times 0.025 = 2.5, \qquad K_i = 100. \tag{3.70}$$

These PI controller gain values were obtained using the PI Tuning interface with the "Robust response time" method.

Both frequency-domain and time-domain tuning modes were evaluated, both of which belong to the class of robust tuning methods. This helped us adjust the control-loop bandwidth to the desired frequency. There have been several sets (8 sets) of controller gains that have been tried on the Closed Loop transfer Function of the current controller to obtain a step response in Figure 3.17.

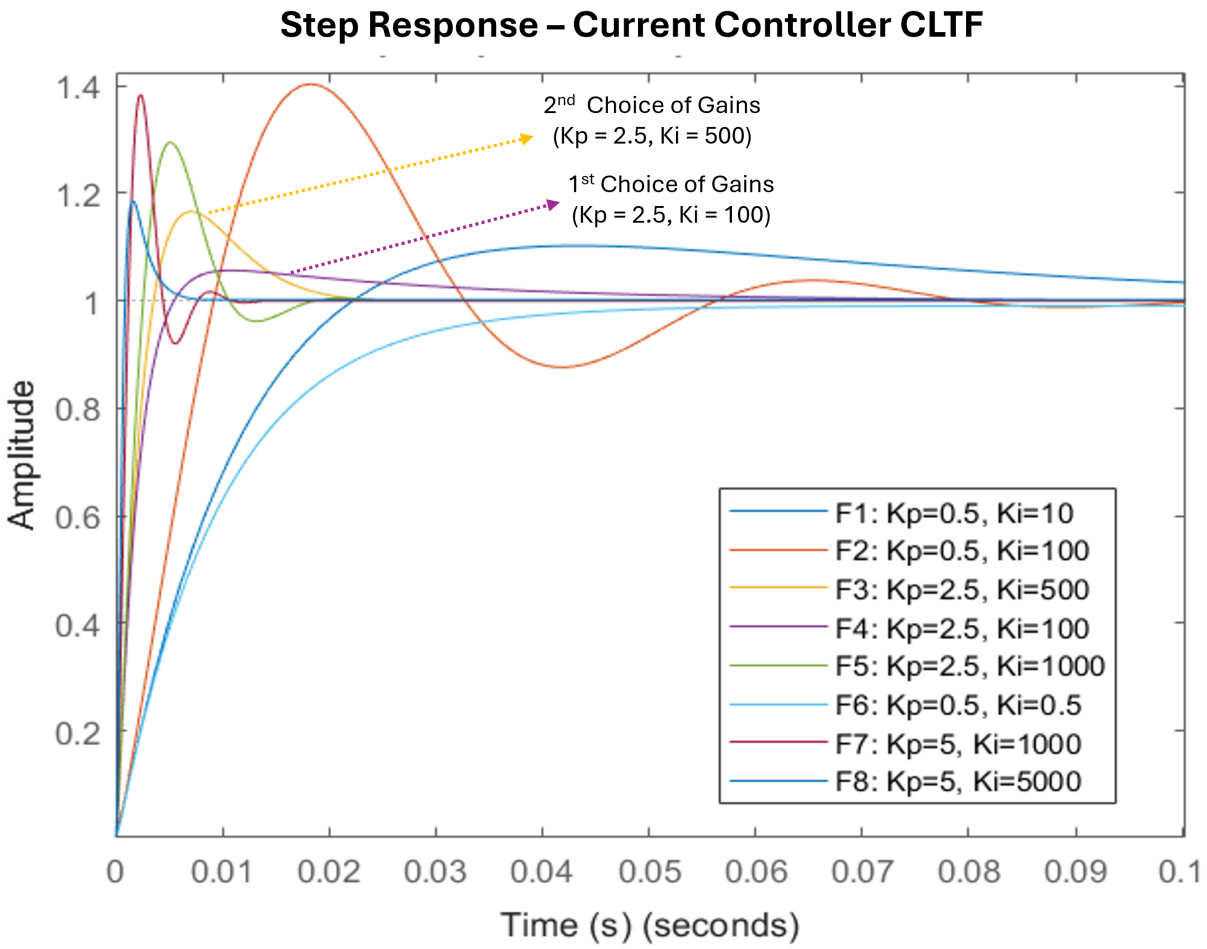

Figure 3.17. Multiple Step Responses from different sets of Gain Values for Graphical Illustration of Controller Gain Choice

After obtaining a graphical comparison of all the different sets of gains, the constraint parameters were checked for each gain set, namely the overshoot percentage, the rise time, and the settling time, to check if any of the obtained step responses did not align with the predefined constraints.

The tuning constraints were:

1) overshoot below 10%,
2) rise time in the order of 0.001 milliseconds
3) a settling time less than one to two grid periods

$$T_{\text{grid}} = 0.02 \text{ s}, \qquad T_s < 0.01 - 0.04 \text{ s}.$$

Sl No.	Gain Values		Parameter Constraints Elimination		
	Kp	Ki	Overshoot(%)	Rise Time (ms)	Settling Time(ms)
1	0.5	0.5	NA	22.3	44.6
2	0.5	10	10.3	15.6	121.2
3	0.5	100	40.4	7.1	73.6
4	2.5	100	6.1	3.4	34.8
5	2.5	500	16.3	2.3	15.5
6	2.5	1000	29.5	1.9	15.9
7	5	1000	38.4	0.9	7.2
8	5	5000	20.7	0.7	5.1

Figure 3.18. Current Controller Parameter Constraint Evaluation

A relative ranking of the gain sets was also performed for each constraint parameter to finalize the selection of a gain set for the current controller. The lower the overall score for the gain set, the more suited the gain value set is for the parameter constraints for the transfer function.

Sl No.	Gain Values		Parameter Constraints Relative Ranking			Overall Score
	Kp	Ki	Overshoot	Rise Time	Settling Time	
1	0.5	0.5	1	8	8	17
2	0.5	10	3	7	7	17
3	0.5	100	8	6	6	20
4	2.5	100	2	5	5	12
5	2.5	500	4	4	4	12
6	2.5	1000	6	3	3	12
7	5	1000	7	2	2	11
8	5	5000	5	1	1	7

Figure 3.19. Current Controller Gain Values Relative Suitability

Based on the rankings of different gain sets shown in Figure 3.19 and the gain sets that were eliminated due to parameter constraints being out of bounds, shown in Figure 3.18. The final choice of gain set was chosen as mentioned in Equation 3.70, showing a rise time of 0.003 s, a settling time well below 0.03 s, with an overshoot of 6.1%.

The Bode magnitude and phase plots exhibited a clean first-order roll-off with no low-frequency resonant behavior, confirming that the L-R model is suitable within the chosen bandwidth. The root-locus plot shows that the closed-loop poles remained well within the left-half plane, with adequate damping and no unstable branches near the selected loop gain. This confirms that the tuned PI compensator yields a stable and well-conditioned current control loop.

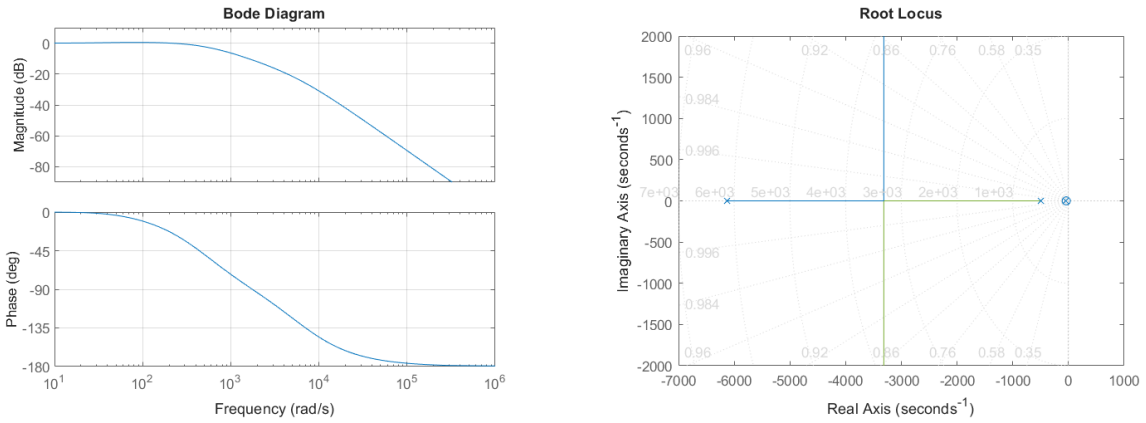

(a) Bode Plot for Current Controller ***(b)*** Root Locus Plot for Current Controller

Figure 3.20. Bode and Root locus plots which shows stable responses for the closed loop transfer function of the Current Controller

3.4.5 Power Controller

The power controller forms the outer control loop of the inverter and determines the dq-current references required to achieve the desired active and reactive power injection. Unlike analytical formulations that compute current references directly from the steady-state relationships among P, Q, and the dq currents, this project employs a closed-loop power controller based on PI regulators.

Active and Reactive Power Calculation and Control

The instantaneous active power at the inverter terminals is computed in the synchronous reference frame using the equations shown in Equation 3.71.

$$P = \frac{3}{2}(v_d \cdot i_d + v_q \cdot i_q) \tag{3.71}$$

In the Simulink implementation shown in Figure 3.21, the measured dq-components of the inverter voltage and current are multiplied and summed to form the instantaneous power estimate. This power estimate is compared with the inverter reference power from the Energy Model. It is noteworthy that the reference power differs across the two energy sources, i.e., Solar and Wind. In fact, the active power reference also falls below zero in the Battery Inverter, indicating the duration of excess power generation relative to the Load.

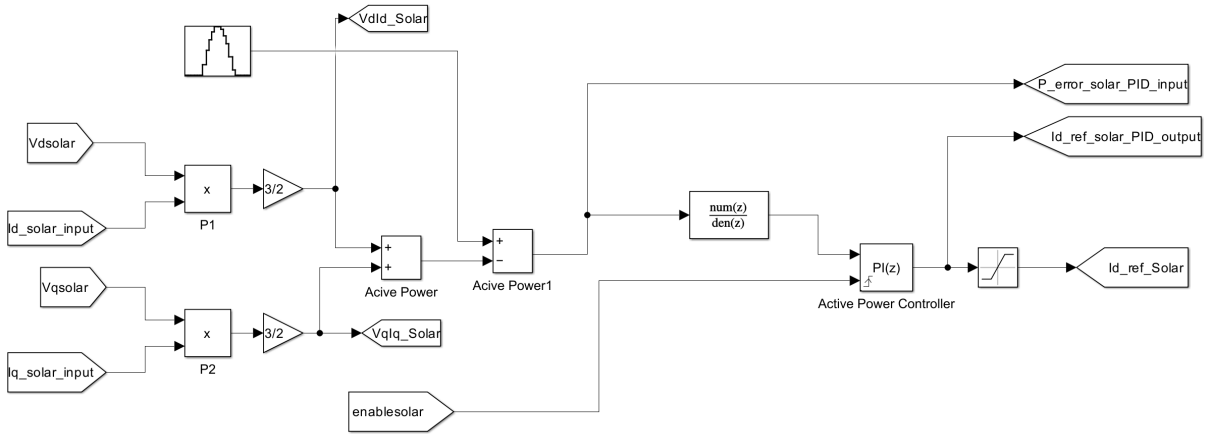

Figure 3.21. Active Power regulation loop for the solar inverter, showing instantaneous power calculation and PI-based reference generation for $i_d^\star$.

Under normal grid-connected operation, the PLL aligns the d-axis with the grid voltage vector. This implies that Vd = Vgrid and Vq is clamped to 0. This assumption effectively reduces the power equation to the following:

$$P = \frac{3}{2}(v_{grid} \cdot i_d) \tag{3.72}$$

This shows that, for a properly aligned synchronous frame, the active power is predominantly governed by the d-axis current. It also means that, if the grid voltage is approximately constant at the operating point, active power control can be achieved solely by adjusting the d-axis current reference.

This measured active power is compared with the active power reference $P^\star$. The active power reference is received from the Energy Model; its profile varies across inverters, and the resulting error is fed to a PI controller. The output of the PI controller corresponds to the d-axis current reference defined in Equation 3.73

$$i_d^\star = K_{p,P}(P^\star - P) + K_{i,P}\int (P^\star - P)dt \tag{3.73}$$

The controller introduces a saturation block to ensure that the generated current reference remains within the allowed limits. The output $i_d^\star$ is sent to the dq-current controller described in subsection 3.4.2.

The instantaneous reactive power is computed from the dq components of voltage and current as defined in Equation 3.74

$$Q = \frac{3}{2}(v_q \cdot i_q - v_d \cdot i_q) \tag{3.74}$$

As with the active power, the reactive power computed is implemented directly in Simulink through multiplication and summation of measured quantities as shown in Figure 3.22.

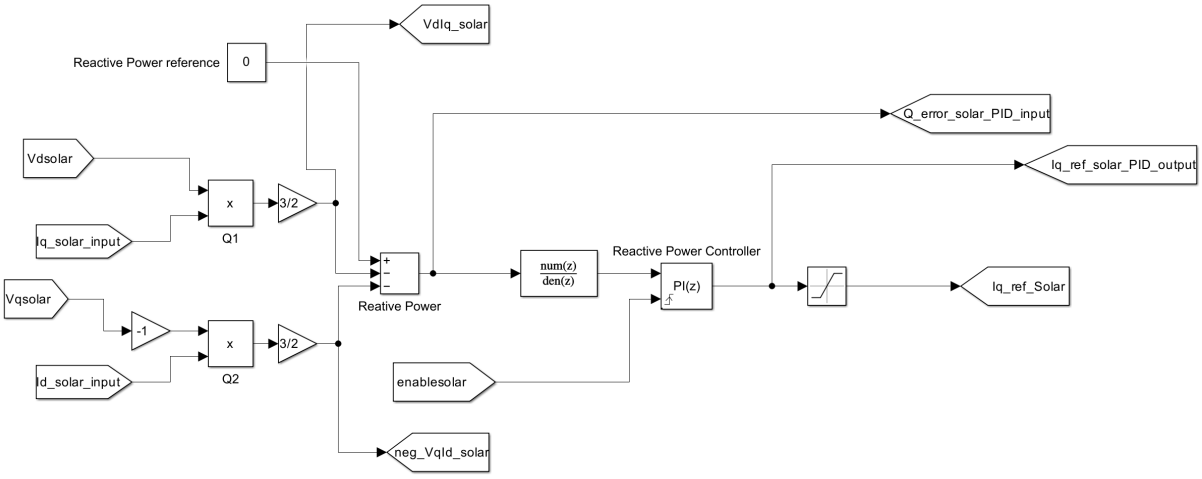

Figure 3.22. Reactive Power regulation loop for the solar inverter, generating $i_q^\star$ from the measured reactive power and reference $Q^\star$.

The measured reactive power is compared with the desired reactive power setpoint $Q^\star$, and the error is fed into a discrete PI controller. The output of the controller is the q-axis reference as seen in Equation 3.75.

$$i_q^\star = K_{p,Q}(Q^\star - Q) + K_{i,Q}\int (Q^\star - Q)dt \tag{3.75}$$

A saturation block ensures that the resulting reference remains within safe limits before passing the reference to the inner dq-current controller.

As shown in Figure 3.21 and Figure 3.22, the solar inverter PQ controller employs the same structure as the wind and battery inverters. The PQ controller, therefore, provides the interface between the power references and the inner dq-current control loop.

Power Controller Tuning

For the outer active-power control loop, we did not rely on a formal optimization method. Instead, the standard hierarchical tuning philosophy was followed used in cascaded control structures. In such systems, the inner current controller must operate significantly faster than the outer power controller so that the current dynamics settle promptly before any changes in the commanded power occur [48].

This requirement arises because the power controller generates the reference i_d^* for the inner current loop. If the power controller were tuned too aggressively, it would modify the current reference faster than the current controller can respond. Such behaviour

can lead to oscillatory references, interaction between loops, and overall poor tracking performance.

To avoid this, a clear timescale separation was enforced between the two loops: the current controller is designed to be fast, whereas the power controller is intentionally slower. The proportional and integral gains of the power controller were selected to be approximately two orders of magnitude smaller than those used in the current controller. This choice ensures that the outer loop evolves gradually, allowing the inner loop to reach and stabilize at its reference before the power loop introduces further changes.

Based on this tuning strategy, the final gains chosen for the active-power controller are inspired by the gains that were finalized for the Current Controller in Equation 3.70

$$K_p = 0.025, \qquad K_i = 0.1. \tag{3.76}$$

The values mentioned in Equation 3.76 produced a smooth and well-damped power response in simulation while maintaining the desired hierarchy between the power and current control loops.

3.5 Simulation Results of Converter Model

The following section presents the results obtained from the switched-model simulations of the microgrid inverters. While the averaged model is used for controller design and dynamic analysis, the switched model provides a detailed validation of the controller performance under realistic switching conditions. The objective is not to analyze harmonics or semiconductor-level behavior, but to confirm that each inverter accurately follows the power reference generated by the control system. The results shown in this section, therefore, focus on the instantaneous three-phase power of the inverters. The overall plant can be seen in Figure 3.23. Only one inverter is connected in the figure, while for the simulation, all three inverters are connected in parallel.

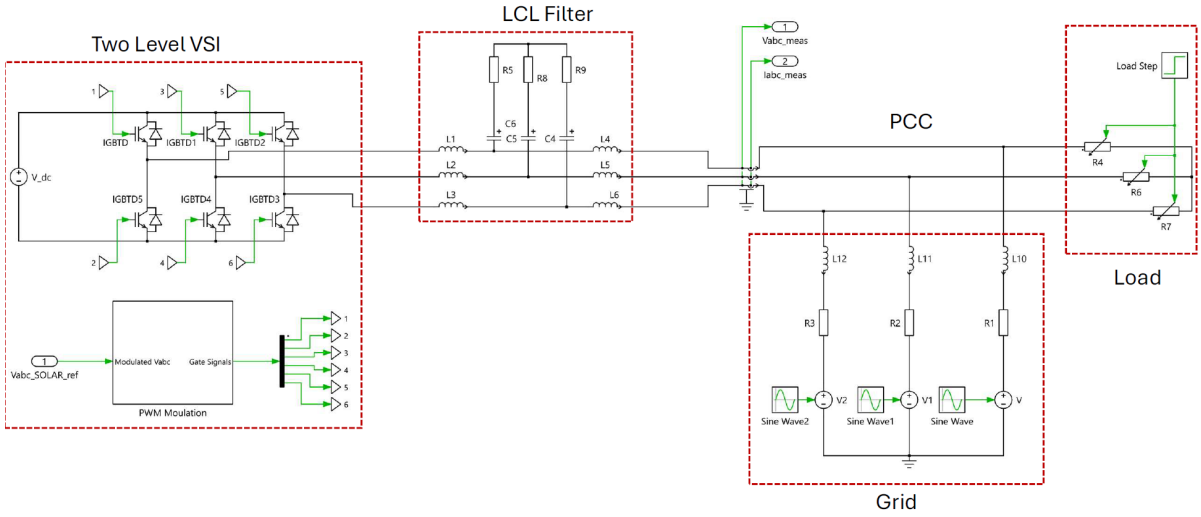

Figure 3.23. The overall Plant shown with a single inverter connected.

3.5.1 Solar Inverter Results

To validate the switching-level implementation of the solar inverter, the switched inverter described in section 3.3 was simulated. The purpose of this validation is not to analyze switching harmonics, but to confirm that the inverter tracks the three-phase power reference generated by the controller. Therefore, the most relevant performance indicator is the instantaneous three-phase output power and can be seen in Figure 3.24.

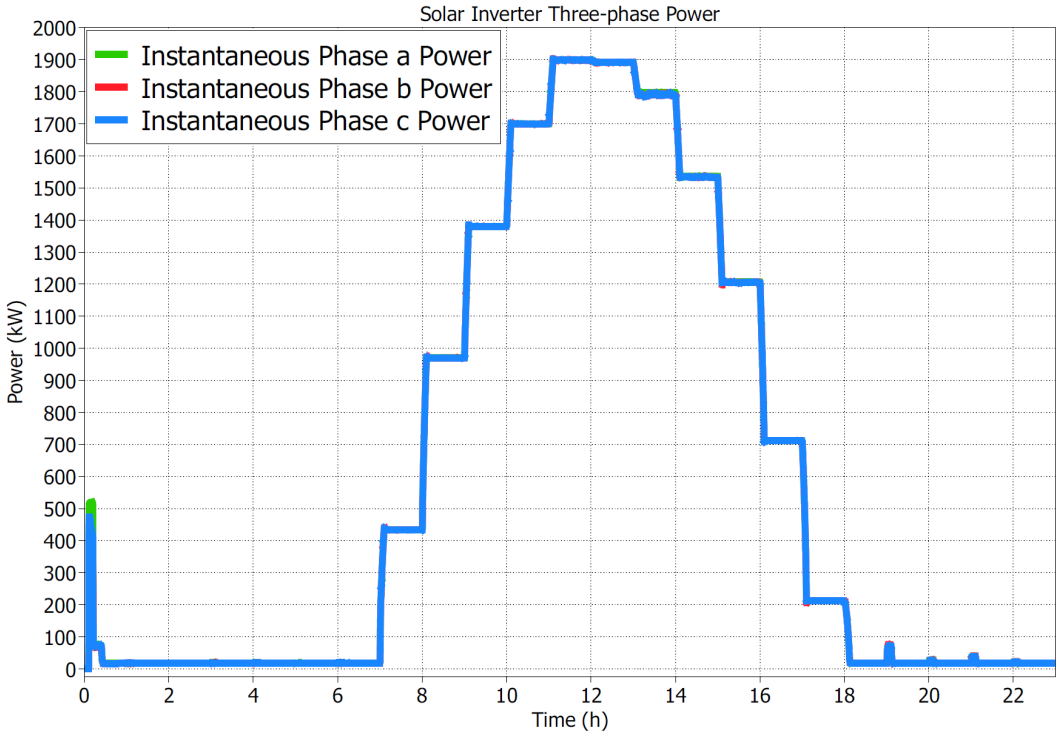

Figure 3.24. Full-day instantaneous three-phase power plot of the solar inverter simulated in Simulink.

Power-Tracking Dynamics during a change in Power reference

To further validate the dynamic behavior of the switched solar inverter, a close-up inspection of the inverter voltage, currents and phase power was conducted at around $8s$ where a change in reference power occurred. The results are shown in Figure 3.25. The upper plot shows the measured three-phase voltages, which remain balanced and sinusoidal throughout the entire transition. No distortion, asymmetry, or transient spikes occur during the change of reference power. The middle plot presents the corresponding three-phase currents. Prior to the change in power, the inverter delivers a lower current amplitude matching the initial power level. Immediately after the power change, the current magnitude rises smoothly. The phase shift between current and voltage remains consistent, confirming accurate alignment with the dq-axis current components.

The lower plot shows the instantaneous phase-a power, which follows the imposed change in power from 400kW to 950kW. Only a single phase is chosen as it can be seen that all three phases are balanced based on Figure 3.24, so for readability, only one phase was displayed. The power increases rapidly without noticeable overshoot and settles into steady state within a few milliseconds. Only the expected high frequency PWM related high frequency ripple is visible. No oscillations or instabilities are observed.

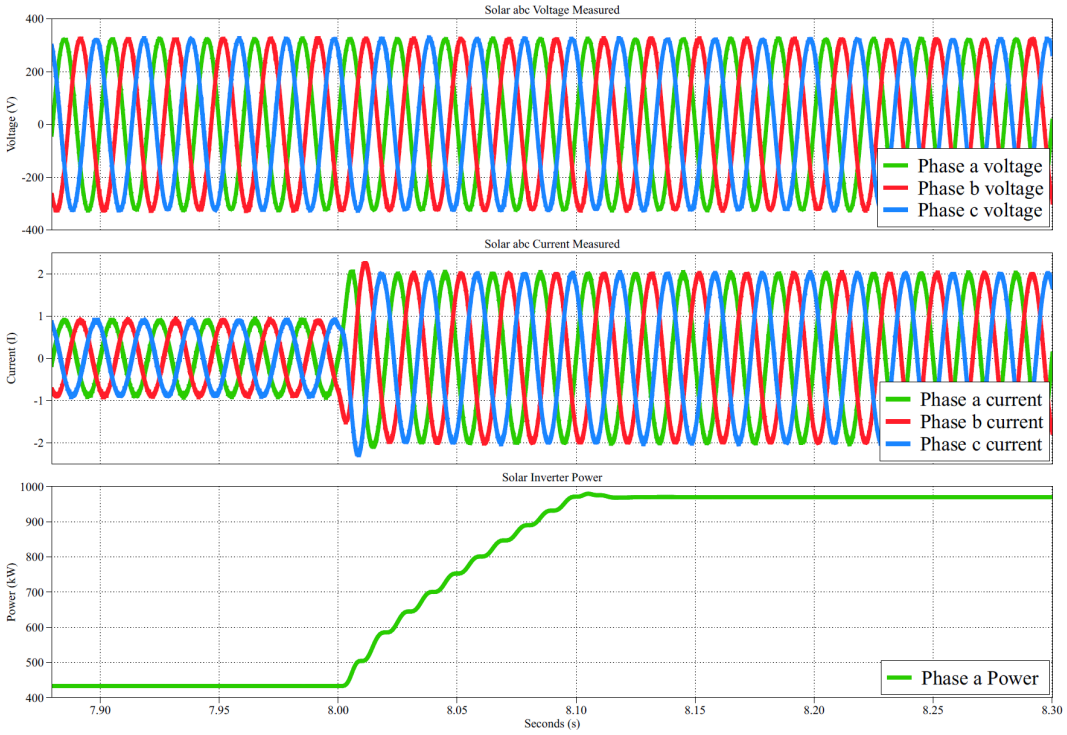

Figure 3.25. Close up view of the solar inverter voltage, current and phase power during a change in power reference.

3.5.2 Wind Inverter Results

To complement the validation of the solar inverter, the switching-level inverter model was simulated using the same PWM-based converter structure as explained in Figure 3.6. The objective is identical: verify that the inverter accurately tracks the instantaneous three-phase power reference produced by the controller.

Full-Day Power Tracking

Figure 3.26 shows the instantaneous three-phase power of the wind inverter over a full 24-hour simulation period. Just like the solar inverter, the wind inverter operates on a balanced three-phase system, causing the phase powers $P_a, P_b.P_c$ to overlap almost perfectly.

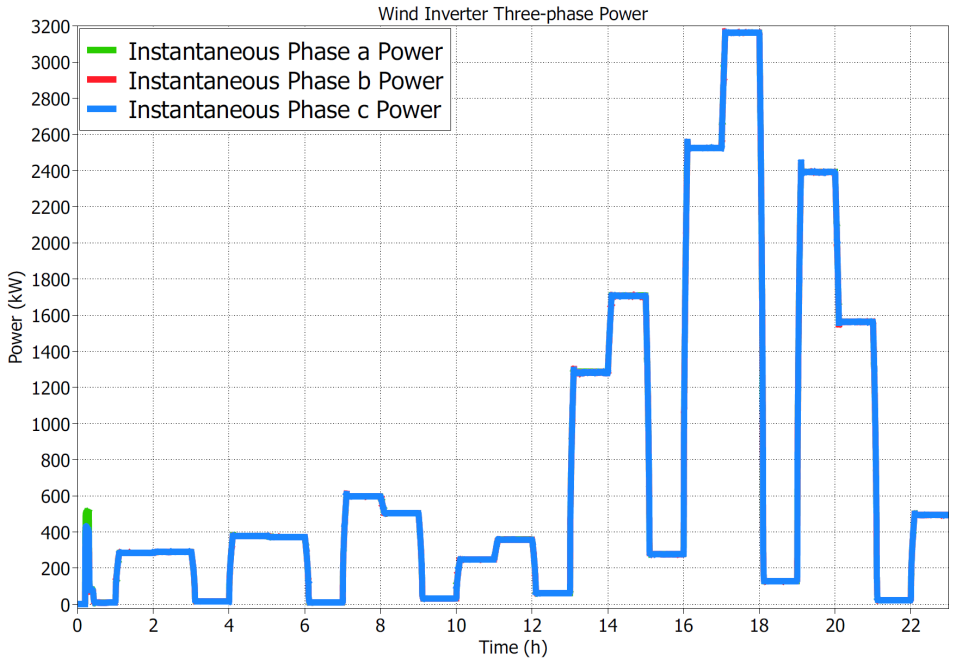

Figure 3.26. Full-day instantaneous three-phase power of the wind inverter.

The overall power profile follows a staircase-type reference derived from the measured 2024 wind-speed dataset, including extended periods of high wind availability and rapid fluctuations throughout the afternoon. The switching-level model successfully reproduces these reference changes without distortion or numerical instability.

Dynamic Response to a Power Reference Reduction Event

To investigate the inverter's dynamic behavior during reference changes, a representative reduction in the power reference at approximately $t \approx 18s$ was examined. Figure 3.27 presents the measured phase voltages, phase currents, and instantaneous power around that event. The following observations can be made:

1) Balanced sinusoidal voltages are maintained before, during and after the transition, showing that a change in the power reference does not introduce any distortion in the power output.
2) Immediately after the reference drop, the phase currents decrease sharply, reflecting the reduction in demanded active power. A brief transient is available, as expected, arising from the L-filter dynamics and the controller's settling.
3) The current quickly converges to a new sinusoidal steady state with reduced amplitude. No sustained oscillations or harmonics distortions are observed.
4) The instantaneous inverter power tracks the power reduction smoothly and without overshoot, demonstrating effective regulation by the current controllers and feed-forward decoupling.

Overall, the results verify that the switching-level wind inverter accurately follows both fast and slow variations in the power reference while preserving balanced three-phase operation and maintaining stable dynamic response.

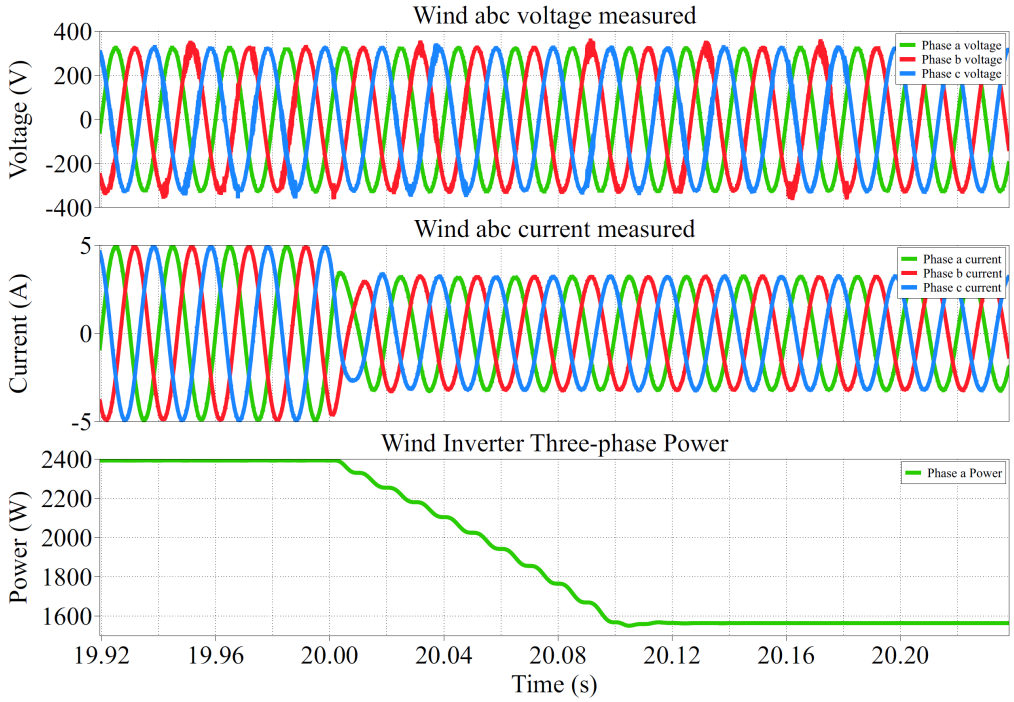

Figure 3.27. Measured phase voltages, phase currents, and instantaneous inverter power at approximately x h.

3.5.3 Battery Inverter Results

The battery inverter is included in the converter model to enable bidirectional power exchange between the Battery and the microgrid. Its primary function is not only to supply active power when renewable generation is insufficient, but also to absorb excess power when renewable generation exceeds load demand. The simulation results for the battery inverter in this section verify that bidirectional behavior is correctly implemented at the switching level while maintaining a balanced three-phase system.

Figure 3.28 presents the three-phase output power of the battery inverter over the equivalent full-day simulation. As for the other inverters, the individual phase powers overlap almost completely, confirming balanced operation throughout the day. The power varies between positive and negative values depending on the battery's operating mode. Positive power corresponds to discharging, in which energy is delivered from the battery to the microgrid, whereas negative power indicates charging, in which surplus energy is stored in the battery. The transitions between these two modes occur smoothly, with only minor ripple introduced by the inverter's switching action.

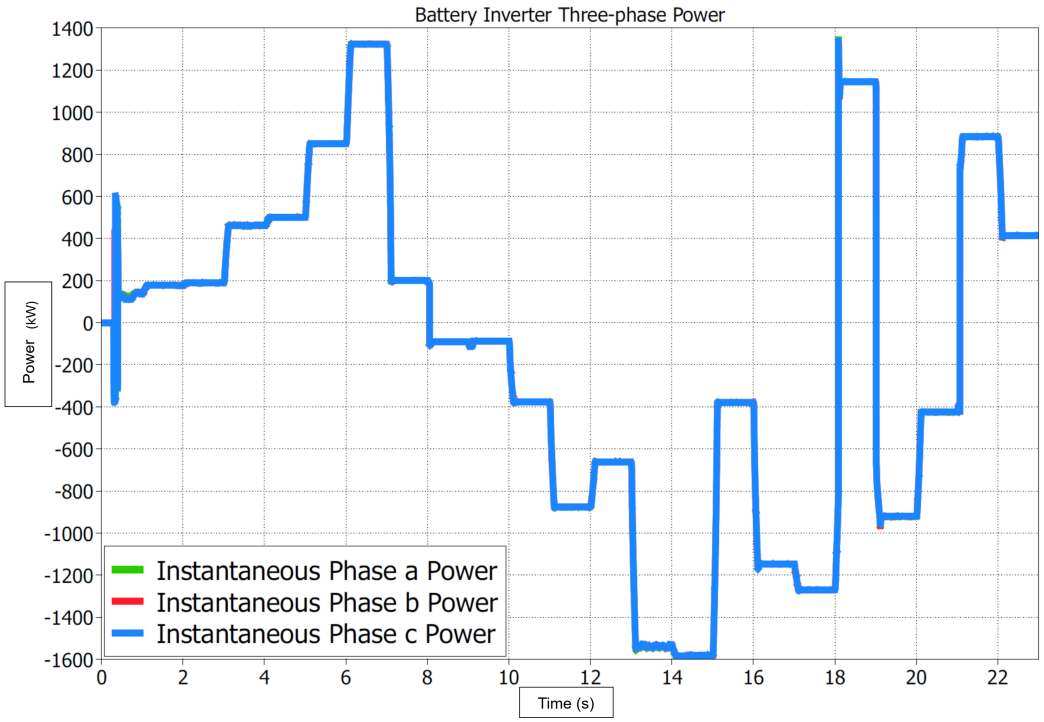

Figure 3.28. Full-day instantaneous three-phase power of the battery inverter, illustrating balanced operation and bidirectional flow during charging and discharging periods.

To illustrate the behavior of these power stages, two short time intervals are further examined in Figure 3.29. In the first interval shown in Figure 3.29a, the battery operates in discharging mode. The phase voltages and currents are aligned, resulting in positive instantaneous phase power. This indicates that active power is transferred from the battery to the microgrid. The waveforms remain balanced and sinusoidal, demonstrating that the current controller maintains stable operation during power delivery.

The second interval, shown in Figure 3.29b, corresponds to the charging of the battery. In this case, the phase voltages have a similar shape and magnitude to the discharging scenario, while the phase currents experience an $\approx 180^{\circ}$ phase shift relative to the voltages. This change in the current phase angle makes the instantaneous three-phase power negative, indicating power flow from the microgrid back into the battery. The smooth operation of the battery inverter during both charging and discharging suggests that the controller successfully reverses the active power direction without introducing instability or imbalance.

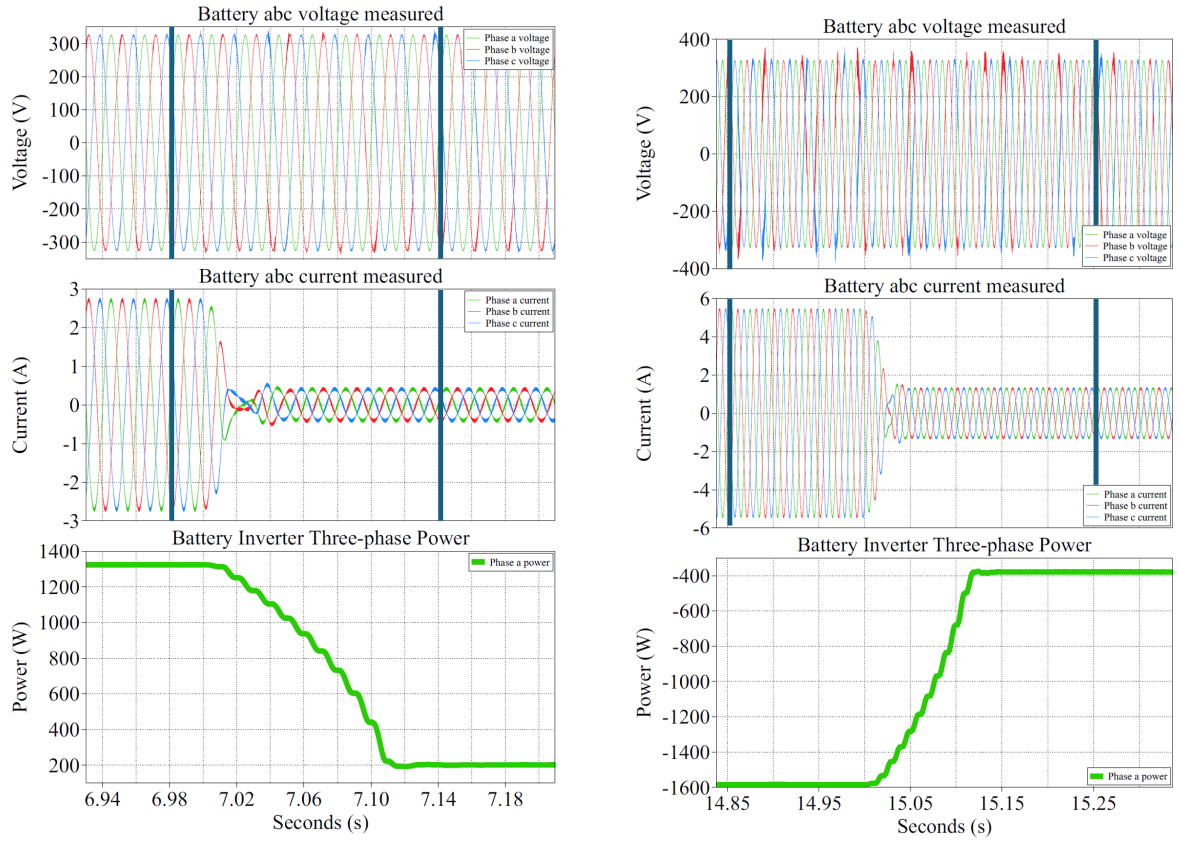

(a) Battery discharging with voltage and current in phase, resulting in positive power flow from the battery.

(b) Battery charging with currents shifted 180° relative to the voltages, resulting in negative power flow from the battery.

Figure 3.29. Zoomed-in view of the response of the battery inverter during (a) discharging and (b) charging, showing phase voltages, phase currents, and instantaneous phase power.

3.5.4 Grid Currents and Voltages

This section evaluates behavior at the grid connection point to examine the interaction between the microgrid and the grid. The focus is on verifying stable operation and balanced three-phase behavior.

Figure 3.30 presents the measured three-phase grid voltages over the whole simulation period. The voltage waveforms remain balanced and sinusoidal, maintaining a constant amplitude and a phase displacement of 120° between phases. This indicates that the grid voltage is not significantly affected by the operation of the connected inverters, ensuring that the PLL maintains consistent synchronization throughout the simulation.

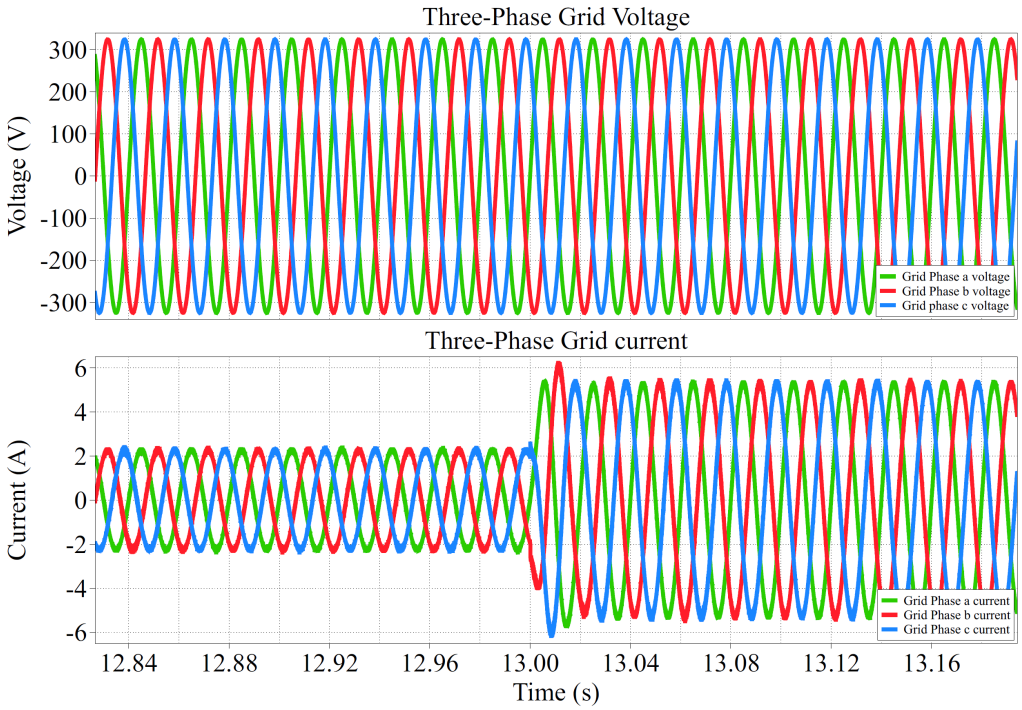

Figure 3.30. Three-phase grid voltage and current measured at the point of common coupling, illustrating balanced sinusoidal waveforms and current magnitude adaptation during variation in power.

The corresponding grid currents are also shown in Figure 3.30. As expected, the current amplitudes vary over time, reflecting changes in the net power exchange between the microgrid and grid. Despite these variations, the currents remain balanced across all three phases and follow the grid voltage in phase.

Overall, the results confirm that the modeled grid operates stably. The grid voltage remains unaffected by the inverters' operation, and the grid currents adjust smoothly to changes in operating conditions.

3.5.5 d-axis Current Reference Tracking

To further validate the inner current control loops of the inverters, the d-axis current reference i_d^* is compared with the measured d-axis current i_d for both the solar- and wind-inverter controllers. In the implemented control structure, the d-axis current directly regulates the active power. Accurate tracking of i_d^* is therefore a reliable indicator of proper power-control behavior.

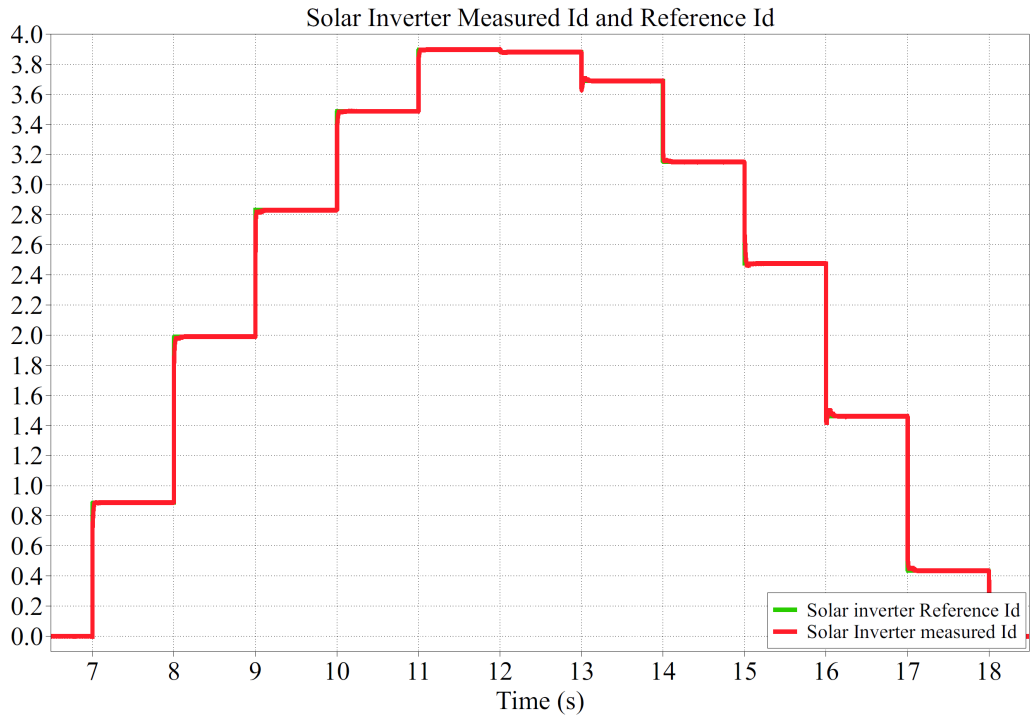

Figure 3.31. Reference and measured d-axis currents for the solar inverter, illustrating accurate tracking of the active power related current during step changes.

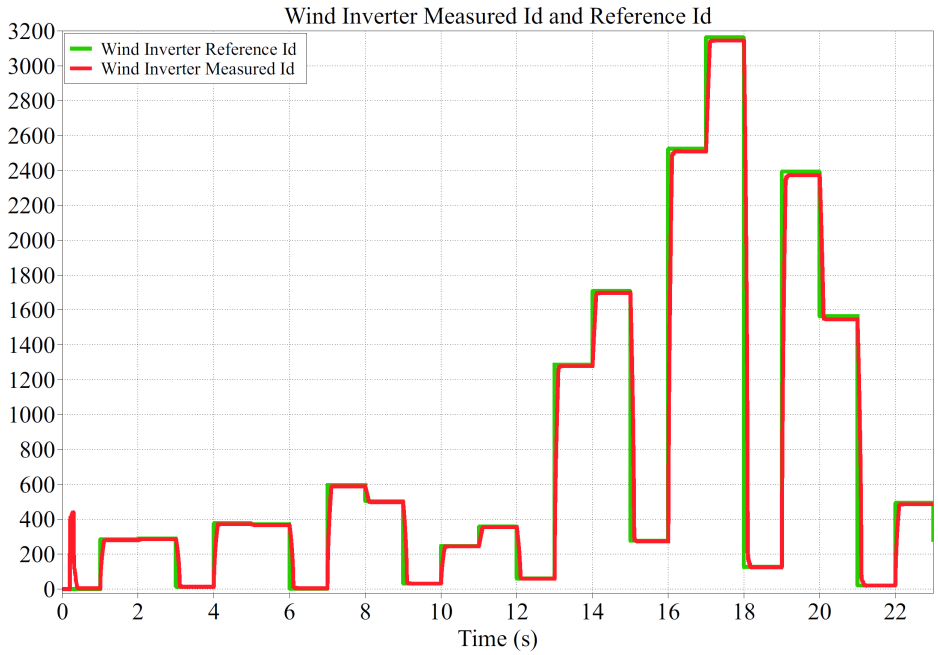

Figure 3.32. Reference and measured d-axis current for the wind inverter, showing fast and accurate current tracking under changing power reference conditions.

Figure 3.31 and Figure 3.32 present the reference and measured d-axis currents for the solar and wind inverters, respectively. In both cases, the reference follows the requested active power derived from the irradiance and wind-speed inputs. The measured d-axis

current closely follows these reference steps throughout the whole simulation, with only small transient behavior after each step change.

Comparing the solar and wind inverter results shows consistent control performance for both inverters. Although the magnitude and timing of the reference steps differ across inverters due to different input profiles, the controller's dynamic response is similar in both cases. This demonstrates that the control structure is robust and applicable across various energy sources within the microgrid.

3.5.6 Total Harmonic Distortion of Inverter Currents

In addition to tracking the power reference, the harmonic quality of the inverter output currents was evaluated by calculating the total harmonic distortion (THD) for both the solar and wind inverters. THD is used as a general indicator of how closely the current waveform approximates an ideal sinusoidal waveform.

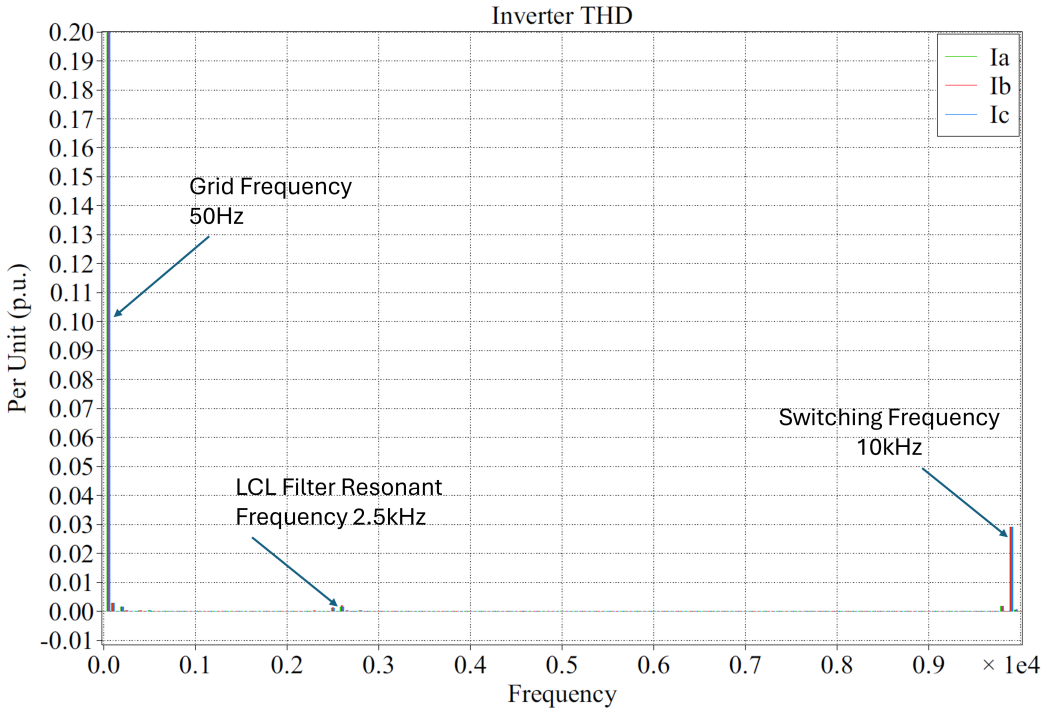

Figure 3.33. Current THD for phases a, b, and c of the inverter. The figure is scaled horizontally with the base frequency THD reaching 1.0 p.u.

Figure 3.33 shows the current THD for phases a,b, and c of the wind inverter, but also the solar inverter, as they are the same. The three phases exhibit very similar THD values, confirming that the inverters operate in a balanced three-phase manner. The dominant contribution comes from the base frequency, while the higher-order harmonics are effectively reduced as desired. Only a small spike is observed at approximately 2.5kHz,

corresponding to the filter resonance, as calculated in subsection 3.4.4, and again at 10 kHz, which is the switching frequency. The measured THD levels remain below the commonly referenced 5% threshold for grid-connected inverters specified in IEEE 1547. This indicates that the implemented current controller provides sufficient harmonic performance for the operating conditions considered in the model.

3.5.7 Load Reference Tracking Performance

The converter model's ability to track the requested load profile is evaluated by comparing the three-phase load power reference with the measured load power, as shown in Figure 3.34. The figure presents a zoomed-in time interval between approximately 5s and 9s, where several step changes are introduced in the load reference.

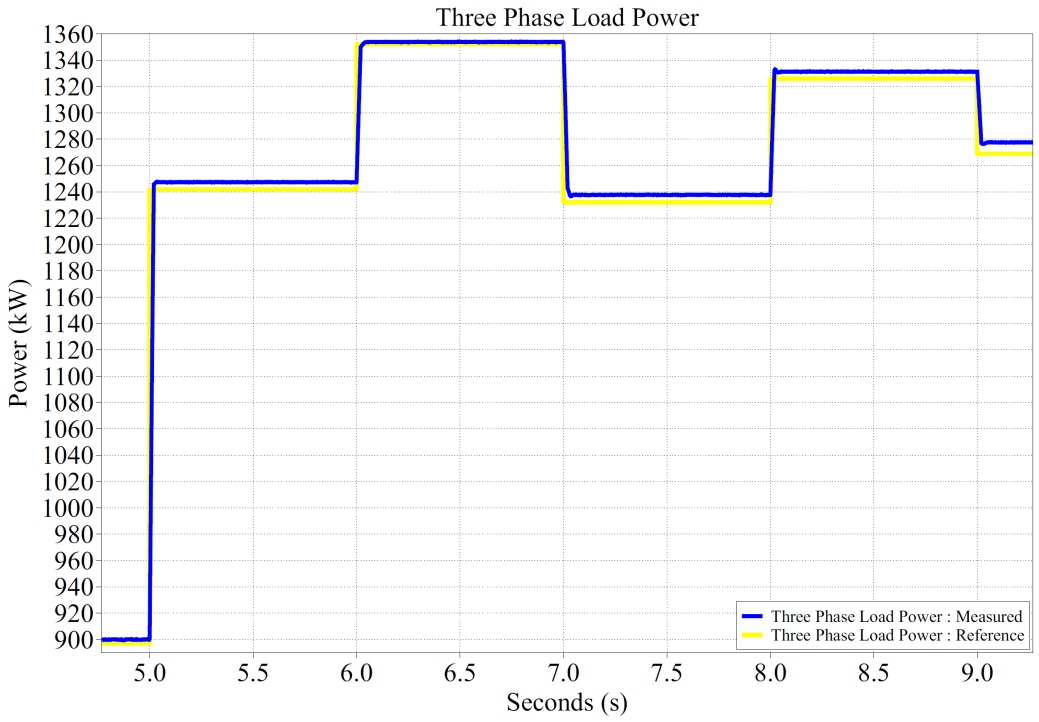

Figure 3.34. Comparison of the three-phase load power reference and measured load power during step changes in the load demand.

As the reference power changes, the measured load power responds promptly and closely tracks the requested levels. Minor transient deviations are observed immediately after each step change and are expected due to the system's dynamic response and the controller's filtering. These transients decay rapidly, and the measured power settles at the new reference value without noticeable steady-state error.

4 Model validation

4.1 HIL Test of the controller

Up to this stage of the work, the inverter system and its associated control algorithms have been validated exclusively through offline simulations. Simulation-based validation provides a controlled and flexible environment for developing and verifying inverter control strategies. In order to bridge the gap between offline simulation and hardware experimentation, a Hardware-in-the-Loop (HIL) testing framework was implemented for the proposed inverter control system. The objective of the HIL implementation was not to redesign the controller, but to verify whether the controller architecture that has been used, i.e., the nested current–power control architecture, retains its behavior under real-time execution. By executing the electrical plant in real time and interfacing it with a physical controller via analog and digital I/O channels, the control algorithms could be evaluated under realistic signal paths, sampling delays, and scaling constraints, without using rated-power hardware during early-stage testing.

4.2 Overview of the HIL Architecture

The implemented HIL platform consists of two main real-time systems: a PLECS RT Box executing the inverter plant model as shown in Figure 4.1 and a dSPACE RTI1103 controller executing the control algorithms as shown in Figure 4.2. These systems are hosted on two separate PCs and are interconnected through physical signal wiring. In this configuration, the complete electrical plant including the inverter, LCL filter, grid model, and local three-phase balanced loads are simulated in real time on the PLECS RT Box processor. The control system, originally developed and validated in MATLAB/Simulink during earlier simulations, is deployed on the dSPACE controller and operates on measured signals received from the PLECS RT Box.

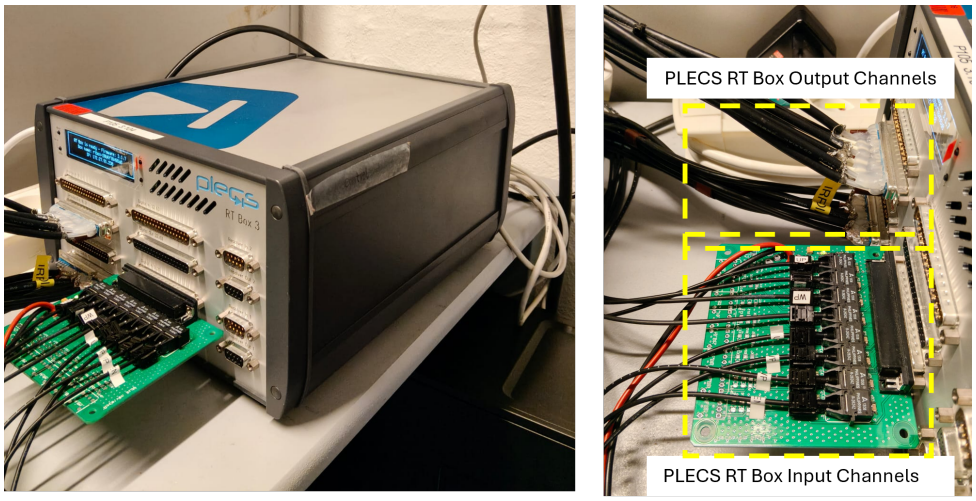

Figure 4.1. Hardware Setup - PLECS RT Box has been used for implementing the Inverter Model

The two systems exchange information exclusively through physical measurement signals and PWM gate signals using multiple ADC channels, thereby closely emulating the signal flow present in a real laboratory inverter setup. This partitioning ensures a clear separation between the plant and controller domains, which is a defining characteristic of controller HIL testing. In Figure 4.2, the hardware setup is shown. dSpace was used for implementing the controller. The measured signals from the PLECS RT Box were received in the dSPace I/O Interface Unit with ADC Channels. This interface unit was also used to send PWM signals to the RT Box for switching the VSI.

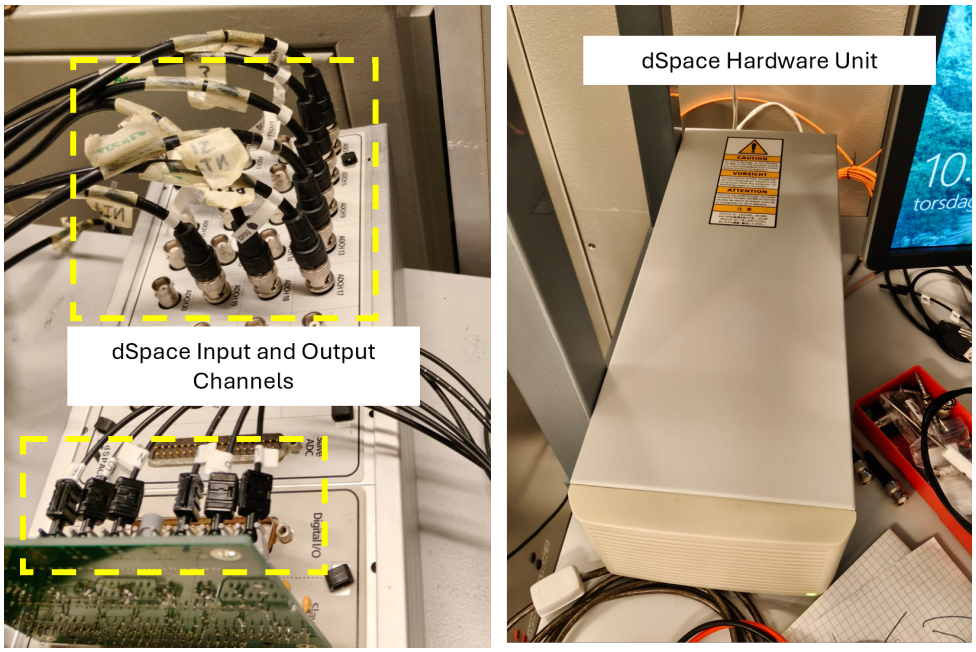

Figure 4.2. Hardware Setup - dSpace Interface and Control Unit

4.3 Plant Model Implementation on PLECS RT Box

The plant model implemented on the PLECS RT Box consists of a two-level, three-phase voltage source inverter connected to the grid through an LCL filter. The filter model explicitly includes parasitic resistances associated with the inductors and capacitors, as well as damping resistors introduced to control resonance effects. At the point of common coupling, balanced three-phase resistive loads are connected in parallel with an ideal three-phase grid voltage source.

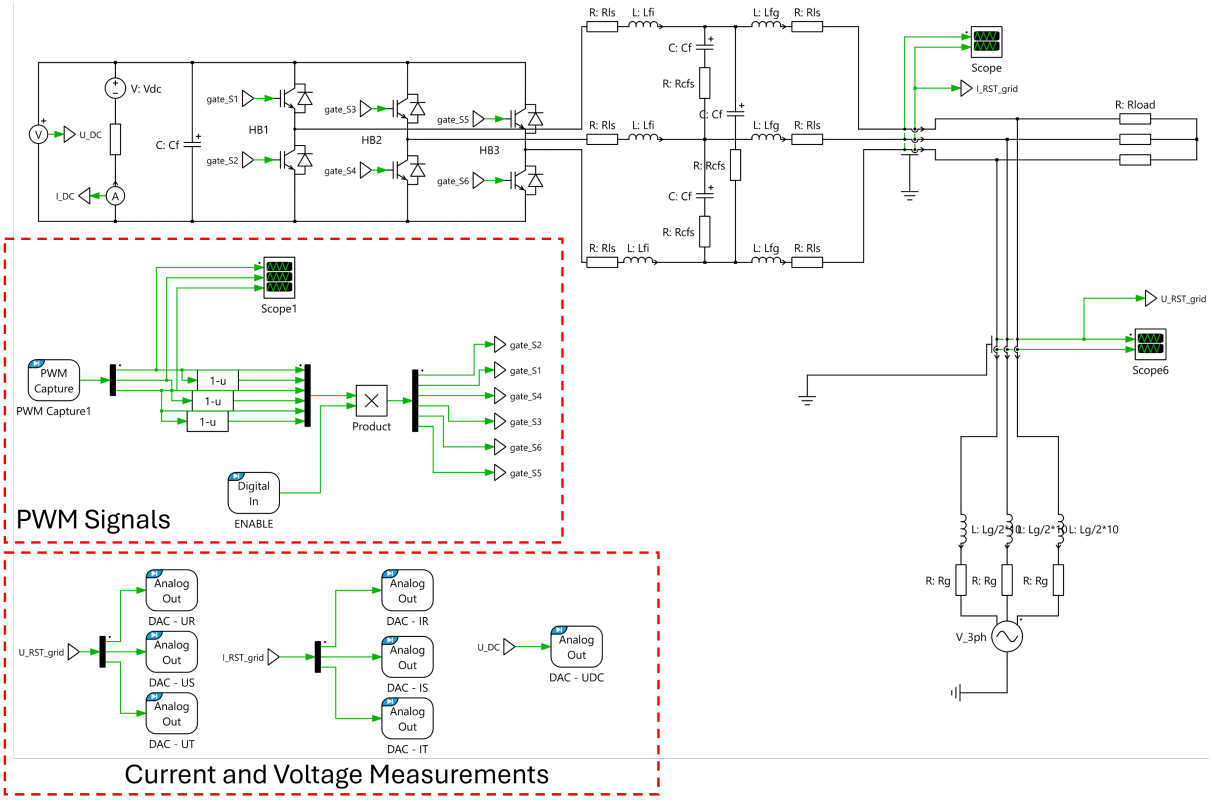

Figure 4.3. Software Setup

Unlike earlier simulation stages, where the plant was executed on a standard computer processor, the entire electrical system is now solved on the PLECS RT Box's real-time processor. This enforces fixed-step execution and deterministic timing, ensuring that the simulated voltages and currents evolve in real time. Figure 4.3 shows how the ADC channels have been used for communicating with the dSPace Controller. Voltage and current measurement signals have been sent out and PWM signals have been received from the dSpace unit. To interface the plant with the external controller, analog output channels are configured within the PLECS model. Six channels are used to transmit the three-phase grid voltages and the three-phase inverter filter currents. These signals are required for grid synchronization and current control, respectively. A seventh channel is

used to transmit the DC-link voltage. All signals are scaled based on the characteristics of the voltage and current sensors mounted on the electronic measurement PCB, ensuring the resulting analog levels are within the input range of the measurement sensors. It is important to note that at this stage, the HIL setup departs from purely numerical simulation, as measured quantities are physically transmitted via control wiring rather than exchanged internally within software.

4.4 Signal Acquisition on the dSpace Controller

The dSPACE RTI1103 controller receives the analog measurement signals from the PLECS RT Box via a dedicated interface card, as shown in Figure 4.5. This card performs the required analog-to-digital conversion and provides the sampled signals to the controller model. Since the control algorithms were initially designed in MATLAB using physical units, a reverse scaling stage is implemented within the controller environment. Each measured signal (grid voltages, inverter currents, and DC-link voltage) is rescaled back to its original physical magnitude using the inverse of the scaling applied in the PLECS RT Box. This ensures the controller operates on quantities consistent with the offline simulation models, thereby preserving controller tuning and design assumptions. Once rescaled, these seven measured signals are fed directly into the nested control structure without modifying the control logic. This approach allows the same controller design to be reused across offline simulation and real-time HIL testing, highlighting the portability of the control architecture. Figure 4.4 shows the dSpace Interface I/O Unit that will receive the voltage and current measurement signals. These signals are scaled back to the original values. Then the controller generates scaled voltage references that are sent to the inverter model on the PLECS RT Box.

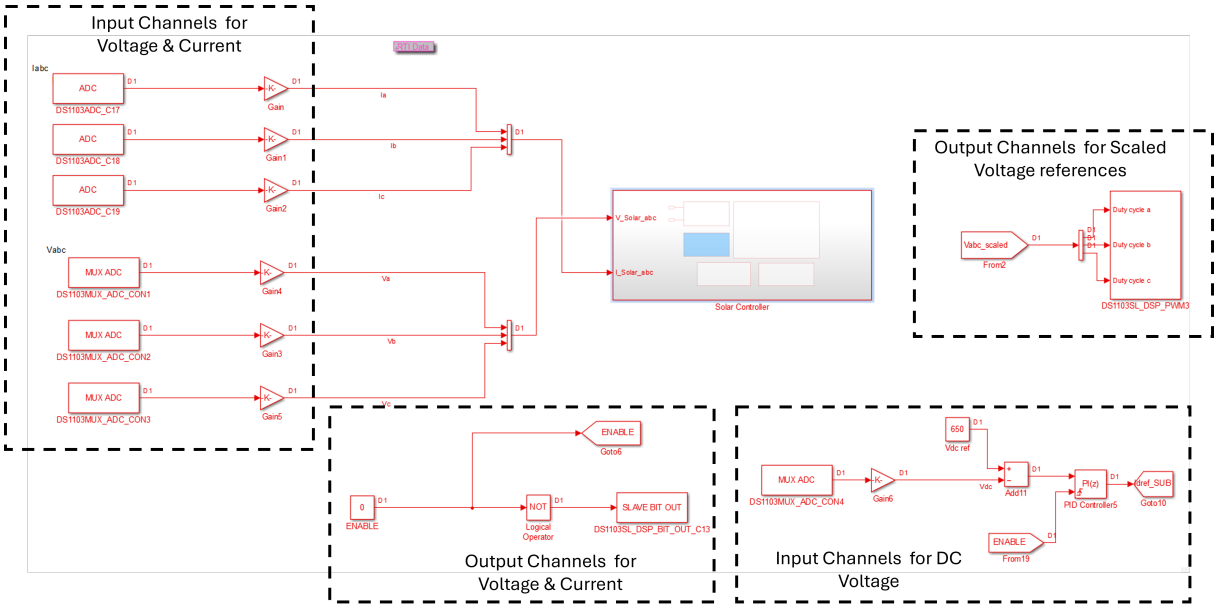

Figure 4.4. Software Setup of the MATLAB Model Implementing dSpace Controller

4.5 Controller PWM Signals to the PLECS RT Box

The controller executed on the dSPACE hardware follows the same nested-loop structure developed during simulation studies. The inner loop regulates the inverter output currents in the synchronous reference frame using PI controllers, while the outer loop regulates active power and generates the corresponding current references. The transformation between the stationary and rotating reference frames is performed using standard dq transformations, with grid synchronization provided by a synchronous reference frame phase-locked loop.

As can be observed in the Figure 4.4, at the controller output, three-phase voltage references are generated. These references must be conditioned to meet the input requirements of the dSPACE PWM generation hardware. On the RTI1103 platform, the internal PWM generator expects normalized modulation signals between 0 and 1. Consequently, the voltage references are scaled and offset using arithmetic blocks to ensure compatibility with the PWM hardware constraints. The PWM block generates sinusoidal PWM gate signals from scaled references and outputs them via a DAC interface. These PWM signals are transmitted via physical links to the PLECS RT Box, thereby completing the control-to-plant signal path.

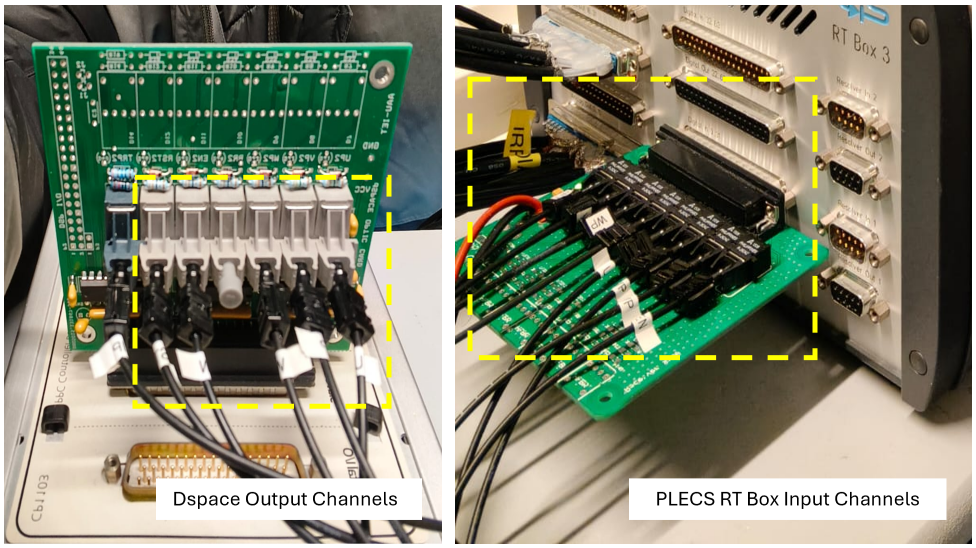

Figure 4.5. PWM Signals generated in the dSpace controller are sent back to the PLECS RT Box.

As shown in Figure 4.3 on the PLECS RT Box side, the incoming PWM signals from the dSPACE controller are accessed using dedicated PWM input blocks. The received signals are de-multiplexed to obtain individual gate commands for the inverter switches. Since the ADC interface in this setup is inverting, an inversion stage is applied to restore the correct logical polarity of the gate signals. The processed PWM signals are then applied directly to the inverter model's gates within the PLECS plant. At this point, the HIL loop

is fully closed: measured plant signals are sent to the controller, the controller computes control actions in real time, and the resulting gate signals are fed back to the simulated inverter.

4.6 Experimental Results using Control Desk GUI Interface

To enable real-time monitoring and interaction, the controller model is deployed in a format compatible with Control Desk, the software used to interact with the dSPACE Hardware Unit.

A graphical user interface is developed to allow user interaction with the control system during operation. Through this interface, proportional and integral gains of the current controllers have been adjusted while the system is running. This feature enables evaluation of controller stability under different operating conditions. During specific tests, the outer power control loop is disabled, and direct d-axis and q-axis current references are injected through the GUI. This operating mode allows isolated validation of the closed-loop current controller in both grid-connected and islanded conditions. In the final configuration, the complete control structure is enabled, allowing the user to specify active and reactive power references, which are internally converted into current references for the inner controller to act on.

4.6.1 Validation of Simulation results through Experiments

The HIL system operated reliably across a wide range of operating conditions and reference values.

Experiment 1 - Grid Connected Inverter with only Current Control Loop

For the first experiment, the power loop was disconnected and specific step responses ranging from 0.5 A to 8 A were given to the current controller to check if the inner control loop was working as desired. As can be seen in Figure 4.6, the hardware implementation worked robustly for the range of setpoints. The Kp and Ki gains of the PI controller that was used in the hardware implementation are the same as in the converter model from Equation 3.70. There are two images of the Graphical User Interface in Control desk for experiment 1, which have been attached in Figure 4.6 and Figure 4.7. The first figure shows the response of the controller to a setpoint of 2A and the second one shows the jump of the setpoint to 5A. The PLL is shown to be synchronized with the grid Voltage.

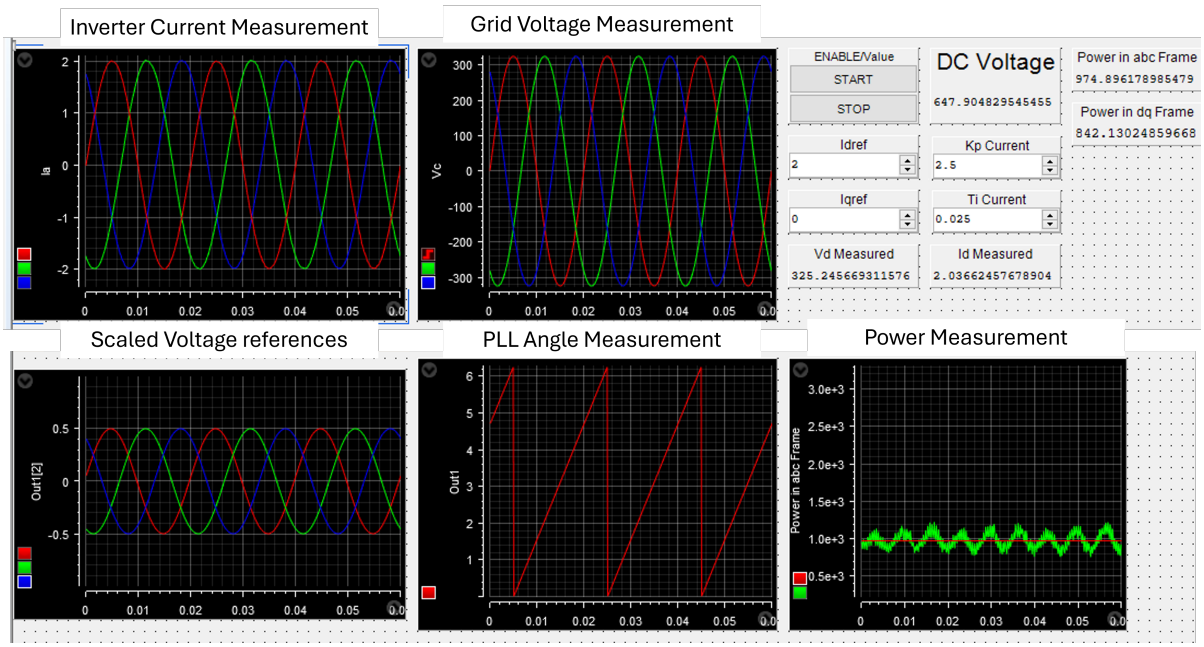

Figure 4.6. Controldesk GUI for Isolated Current Controller at Id=2A

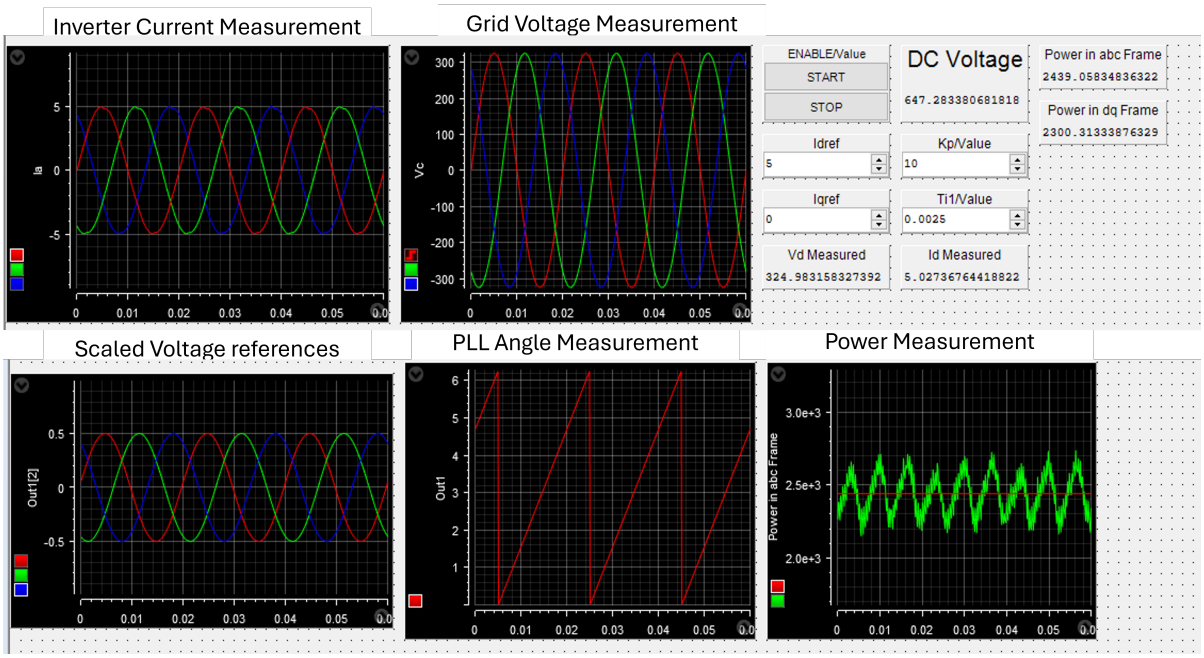

Figure 4.7. Controldesk GUI for Isolated Current Controller at Id=5A

Experiment 2 - Grid Connected Inverter with Nested Power and Current Control Loops

In the second experiment, the power controller was connected to the current controller. The active power reference for the power controller was derived from the Energy Model, which has already been discussed in chapter 2. The provided power references were used to calculate the references for the d-axis and q-axis current used in the current controller

to generate voltage references for the inverter model. In Figure 4.8, it can be observed how the calculated power is at par with the power reference at 1500W. The PI Controller gains used for the Power controller are the same as those used in the simulation and mentioned in Equation 3.76. It is also observed that the current reference is no longer required, like in Experiment 1, as it is being generated internally by the controller.

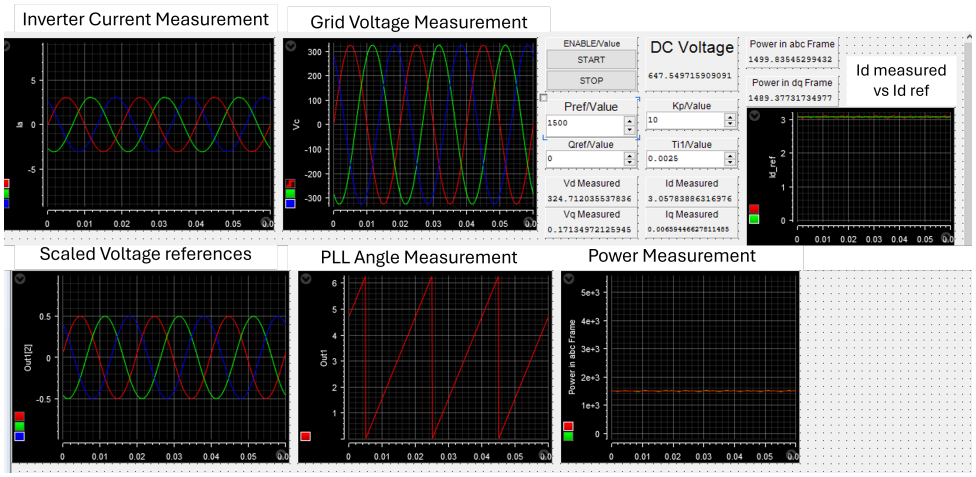

Figure 4.8. GUI for Integrated Power and Current Controller with Power reference at 1500W

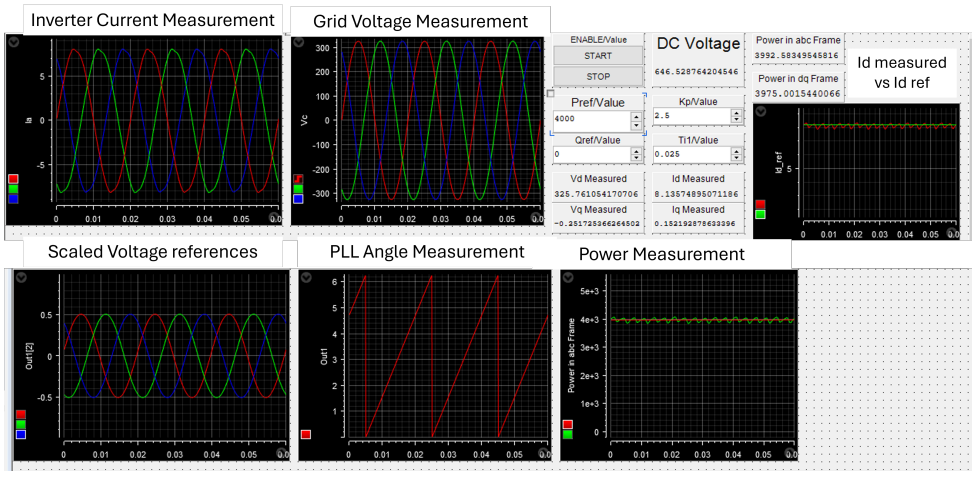

Figure 4.9. GUI for Integrated Power and Current Controller with Power reference at 4000W

The second figure, i.e., Figure 4.9, enunciates how the controller for the inverter in HIL follows the power reference for a large change in the power reference to 4000W. Real-time execution of the power and current setpoints in the controller confirmed the stability and robustness of the nested control architecture previously validated in simulation. The ability to modify controller gains and Operating Power Setpoints through the Control Desk GUI proved particularly useful.

4.7 Summary of HIL Testing

This chapter presented the implementation and validation of a Hardware-in-the-Loop testing framework developed to assess the proposed inverter control strategy under real-time conditions experimentally. By implementing the electrical plant in PLECS RT Box and deploying the controller on a dSPACE RTI1103 platform, the study established a clear separation between the plant and controller domains while preserving realistic signal exchange via physical analog and PWM interfaces.

The HIL setup enabled direct evaluation of the nested current–power control structure without altering the original controller design used in offline simulations. There was real-time acquisition of grid voltages, inverter currents, and DC-link voltage, combined with physical transmission of PWM gate signals. In addition, the Control Desk enabled GUI-based testing of several controller setpoints. The results from HIL testing demonstrated that the control strategy maintains stable, predictable behavior when executed on real-time hardware, closely matching the performance observed in simulation.

5 Discussion

5.1 Energy Level Modeling

The energy model was used to study the relationship between the load demand of the B-WTP and the energy supplied by the PV, WT, and BESS. The system was simulated with an hourly time step over one year. This allowed the mismatch between renewable generation and load demand to be identified, particularly the strong dependence on PV production and the relatively small contribution from WT.

The simulation results showed that configurations without a BESS result in high levels of energy import from and export to the grid. This indicates that renewable generation alone is not sufficient to supply a critical load reliably. When a BESS is included, the power balance improves, grid interaction is reduced, and both self-consumption and self-sufficiency increase.

Seventeen different configurations were analysed to determine suitable sizes for the PV plant, WT plant, and BESS. The results indicate that a hybrid PV-WT system with a 10 MWh battery provides a good compromise between technical performance and cost. Among the analysed cases, case 12 (7225 MWh of PV, 1076 MWh of WT, and a 10 MWh battery) offers the most favourable outcome.

The energy model also provides the power reference profiles used in the converter-level simulations presented in the next chapter. In this way, it links the annual energy balance of the microgrid with the dynamic behaviour analysed at the converter level.

5.2 Converter Modeling

The work carried out in this project begins with an average-model and its controller design, which is later on changed to a switching model in an inverter in a microgrid integrated with a battery energy storage system. The inverter is also connected to the primary grid in the event of loss of self-sufficiency or excess power production. The overall modeling approach was based on a nested controller in the synchronous reference frame for both the current and power loops. The discussion that follows talks about the modeling approach that has been used and interprets the simulation results obtained from the simulation results and the HIL validation.

5.2.1 Reflection on Modeling Approach

As mentioned earlier, the converter modeling was performed in two steps: the first controller was designed using an average model of the two-level voltage-source inverter connected to a simplified L-filter. As a result of this simplification, it was operated with no switching ripple using controlled voltage sources. A linear relation between the dq-voltages and the resulting filter currents was achieved due to having three-phase balanced resistive loads. Such a representation was well-suited for deriving loop transfer functions, analyzing the importance of feedforward and cross-coupling terms in the controller design, and defining the current and power loop bandwidths to determine the parameters that determine the tuning of the power and control loops.

However, this simplification omits the nonlinearities that include real switching behaviour and the design challenges that accompany a switched model of an inverter. There are additional delays in the simulation loop, like a discretization delay, switching and sampling delay, which are to be included while determining the new closed-loop transfer function of the switched model. Another major change is the introduction of switching harmonics that accompany a switched model, which led to the simplified L filter being replaced by a more complex LCL filter. The filter resonance frequency was calculated and ensured not to coincide with the switching frequency. This detailed switching model is therefore very important for validating that the control design obtained from the average model, before proceeding to the HIL testing.

5.2.2 Controller Performance Evaluation

The cascaded control structure was evaluated through a set of simulations that talk about how the inverters respond to changes in power demand and loading conditions, without dependence on the grid for power delivery to meet changing load requirements. The power references were derived from the Energy Model. The fast-acting inner current controllers were tuned to track the d-axis current reference supplied by the outer power loop while keeping the q-axis current bound to zero under unity power factor as the load was purely resistive. The outer power loop, which was tuned hierarchically to operate much more slowly using manual tuning methods, had a lower bandwidth and allowed the current controller sufficient time to allow the d-axis to reach its new reference point, resulting in the active power error converging to zero for every step change in power reference.

The results show that the d-axis current i_d closely follows its reference over the considered operating range. During step changes in the active power, i_d exhibits a well-damped transient with an overshoot less than 10 percent and a settling time within one or two power frequency cycles. The q-axis current remains smalland bound to zero, indicating that the controller effectively maintains the desired power factor. The use of transfer-

function-based tuning in the MATLAB control system block SISOTool is also worth mentioning, as it provides options to edit and tune the control loops, along with Bode and root-locus plots to illustrate pole-zero placement and overall system stability.

In the outer Power controller loop, the calculated active power from the measured three-phase voltage and currents ahead of the inverter filter tracks the reference power with rise time, settling time, and overshoot percentage is as expected. The mismatch between the demanded load power and the power supplied by the inverters goes hand in hand, which is the most important objective of the inverter mode,l i.e., to support the load connected. There are minimal transients in voltage and currents at the load. The time scope alignment of the two curves presented in the results section confirms that the outer loop is capable of regulating power flow. Deviations during transients are mostly due to energy stored in the LCL filters and the finite speed of the current loop, but they are short-lived and do not compromise the controller's overall stability or functionality.

For each inverter, the simulated three-phase voltages and currents at the grid-side terminals exhibit the expected sinusoidal shape and phase relationships. An interesting but necessary addition to the results and simulation section was the effect of adding an LCL filter to the switching model, which reduced inverter current harmonic distortion to less than 5 percent, ensuring compliance with EN 50160 grid standards.

5.2.3 Microgrid Power-Balance Considerations

One of the primary purposes of the model is to study how several inverters share the supply of a typical three-phase load and how power is redistributed when different units change their operating setpoint. The simulation results indicate that the control strategy can match the aggregate inverter output to the time-varying load demand. The graph comparing the commanded load power with the measured power across the load shows a close overlap once transients have decayed, implying that the total power injected by the inverters is well coordinated with consumption.

Within this framework, the individual inverters play distinct roles. The inverters connected to renewable energy sources like PV and Wind Turbine operate in generation mode, contributing positive active power to the system. In contrast, the battery inverter acts as a balancing unit that can either inject or absorb power depending on the overall power balance. When the generation exceeds the load demand, the battery inverter shifts to charging mode. This is cemented by the measurement of negative power and the associated phase reversal between current and voltage. The current changes phase by approximately 180° relative to the terminal voltage, resulting in negative instantaneous and average active power. This inversion of the phase relation has been presented in the

power plots of the battery inverter. It demonstrates that the same control structure can accommodate both typical BESS functions in a microgrid, such as load following and surplus energy absorption, without loss of stability.

Although the grid is represented as an ideal voltage source, the dynamics inside the microgrid which refere to redistribution of instantaneous currents, alignment of voltage vectors using the SRF PLL technique, and the shaping of the load and inverter power profile, follow the same principles that govern larger mocirogrid models. These results establish a baseline for future studies involving non-ideal grids, grid events or varied feeder impedance.

5.2.4 Limitations of the Current Implementation

Despite the encouraging performance, several limitations of the current implementation must be acknowledged. First, the grid is represented as an ideal, stiff voltage source, neglecting line impedance, frequency deviations, and harmonics. As a consequence, effects related to weak-grid operation, resonances with feeder inductances and capacitances. These assumptions include grid events and faults, although the analysis has been restricted to balanced three-phase conditions. Unbalanced faults, asymmetrical loads, and harmonic distortion on the grid side were not considered in the present work. Under such conditions, the behavior of the PLL and the *dq* transformations becomes more complex, and the controller may require additional compensation to maintain accurate synchronization and acceptable current quality.

Second, the current project work has not yet explored the different control schemes that are possible in different reference frames, the usage of nonlinear controllers, or the usage of varying inverter topologies like three-level NPC or multilevel inverters, which could reduce the harmonic distortion in the inverter voltage and current, resulting in a reduction of filter size.

The possibilities for overcoming these design challenges are discussed in detail in the next chapter, which addresses the project's future scope.

5.2.5 Discussion of HIL Tests

HIL testing has been identified as a desirable step towards experimental validation of the proposed control strategy. In the current project, the HIL experiments were conducted on dSpace RTI1103, which hosted the Control algorithm, and a PLECS RT Box, which hosted the main inverter plant model. The measurement signals from the inverter currents and the grid voltages were physically sent out using ADC blocks and received by the dSPACE Hardware Interface Unit. The control algorithm was made compatible with the Control

Desk Software, and the received signals were fed into the controller. The generated PWM signals were sent back to the PLECS RT Box and fed to the inverter as gate signals for the switches. This arrangement has enabled investigation of implementation aspects such as real sampling and computational delays, measurement noise, scaling errors when dealing with current and voltage measurement sensors as well as interaction with actual measurement hardware, without the need to operate a full-scale power laboratory setup.

The entire experiment was implemented using a controldesk GUI where multiple experiments were performed on the Control Desk with the Current Controller, first, operating independently of the power controller to assess its stability across different setpoints for the Id and Iq currents. The Power controller was then connected to the overall system, with the nested controllers online, while the inverter was connected to the balanced three-phase load and the grid. This setup was tested at multiple power reference setpoints, which the controller successfully tracked in closed-loop. These experiments demonstrated the overall system's ability to quickly track power and current references provided to the inverter and controller model, providing evidence of the controller's stability. As a result, the HIL framework served as a robust intermediate validation stage, proving the practical feasibility of the proposed control system and establishing a solid foundation for future hardware-based experimentation.

6 Conclusion

The purpose of the project was to design and analyze the working of a renewable energy-based microgrid capable of supplying reliable electrical power to the B-WTP which has a weak grid connection to the Ghanaian grid. By combining energy-level modelling, converter-level simulation, and control design, the study successfully demonstrates that a properly sized microgrid integrating PV, WT, and BESS can significantly improve supply reliability while reducing dependence on the national grid.

The ideal load profile of the B-WTP showed that approximately 7.7 GWh of energy is required annually, with a peak daily demand of 1.35 MWh. The energy model was developed using measured 2024 irradiance and wind-speed data. Seventeen system-sizing scenarios were simulated to determine the best combination of renewable generation and battery energy storage. The results show that a microgrid consisting of 1.7MW PV Farm, a 250-kW WT, and a 10 MWh battery offers the most technically and economically balanced solution. This configuration achieved 92% self-sufficiency, 94% self-consumption, and has reduced grid dependency by a lot, while avoiding the under-utilisation of the installed renewable energy sources seen with larger (15 MWh) storage systems.

Both average and switching models of the inverter were developed at the converter level using dq-frame transformations, an LCL-filter design, and current and power control loops. When the controller, which was designed for the average model, was implemented along with the detailed switching model, it continued to operate as expected, with the inner current loop responding smoothly to reference changes. The decoupling and feed-forward terms helped to decouple the d and q currents. The outer power loop produces accurate active-power regulation, and the measured load power closely follows the power reference profile. Switched Model simulations confirm that the controller remains effective when the inverter operates with sinusoidal PWM, finite sampling delay, and LCL filtering, and the battery inverter accurately reverses its power flow, as seen from the 180° phase shift between voltage and current. The combined output of the three inverters matches the load demand, which is one of the most important objectives for our project. The switched model has been implemented in the HIL using physical control wiring, which helps us understand the effect of control and switching delay, scaling errors and measurement noise.

Overall, the simulation results show that the microgrid model can meet most of the plant's energy needs on its own, reducing imports drastically, and only exporting power when

there is more generated energy than the system can store and use. This balanced import and export behaviour means the plant makes full use of the energy it produces, instead of wasting excess renewable power. These findings show that a well-sized hybrid microgrid with battery storage can significantly improve power reliability for B-WTP while also supporting Ghana's broader move toward a cleaner and more resilient energy future.

7 Future Scope

This project has explored the modeling and control of multiple grid-connected two-level inverters using cascaded power and current control in the synchronous dq reference frame. Although the proposed control strategy performs well under ideal operating conditions, real-world microgrids rarely operate in these environments. To reflect how microgrids actually operate, several meaningful extensions to this project are both relevant and necessary. Incorporating these aspects would allow the system to be evaluated under more demanding conditions and enhance the overall realism of the model. The main areas for future investigation are discussed below.

7.1 Response to Grid Disturbances and Load Unbalance

An extension of this work is to evaluate the inverter system under various grid disturbances and unbalanced load conditions. In current microgrids, events such as phase faults, short circuits within connected loads, and voltage sags at the PCC occur intermittently and cannot be neglected. Such disturbances introduce negative-sequence components and harmonic distortion into the grid voltage, directly affecting the assumptions underlying synchronous-frame control.

Under these conditions, the performance of the PLL becomes significant. Since the PLL determines the reference angle used in the dq transformation, inaccuracies in the estimated angle $\hat{\theta}$ goes throughthe control variables and may affect current tracking or even cause instability of the control loops. Conventional PLL designs do not often work well with unbalanced or distorted voltages and may exhibit oscillatory behavior or angle drift.

Future work could therefore focus on evaluating more advanced synchronization techniques. Examples include PLLs combined with repetitive control to mitigate periodic disturbances, SOGI-based structures that enable improved sequence separation, or PLLs incorporating FIR filters for selective harmonic attenuation. Comparing these approaches would provide valuable insight into their robustness and suitability for faulted or unbalanced grid conditions.

7.2 Alternative Control Frames and Control Strategies

Another possible extension of this work is to compare the current dq-frame PI control approach with other control strategies implemented in different reference frames. Some controllers are designed in the stationary reference frame or directly in the natural frame. Each approach operates with its own principle.

Proportional–resonant (PR) controllers in the stationary reference frame are a commonly used alternative. These controllers provide high gain at the fundamental frequency when the resonant frequency term coincides with the nominal frequency term. These controllers enable accurate tracking of sinusoidal currents without the need for a rotating reference frame, which serves as a reduction in the computation power required by the processor on which these are implemented in real time.

In the natural reference frame, deadbeat and hysteresis current controllers represent further alternatives, which aims to achieve exact current tracking within a single sampling period, while hysteresis control dynamically adjusts the switching instants to keep the current within predefined bounds. Both methods offer fast transient response, but differ significantly in switching behavior, computational demands, and robustness to parameter uncertainty.

A systematic comparison of these control strategies with the synchronous-frame approach used in this project would clarify how total harmonic distortion, transient response, and control effort are affected by the chosen control framework. The performances of these controllers have been extensively studied in earlier publications, but the possibility remains that we can explore a combination of controllers.

7.3 Incorporation of Renewable Energy Sources

In the current model, the DC side of each inverter is simplified an ideal constant source. In real microgrids, several renewable energy sources are used and each have their own dynamics and control.

For PV systems, maximum power point tracking (MPPT) is used to adjust the operating voltage as the irradiance and temperature changes. Wind energy systems also use MPPT to maintain an optimal tip-speed ratio. Once such source-level controllers are included, the active power reference supplied to the inverter is no longer fixed and becomes dependent on the available renewable power. This would enable the model to capture interactions among multiple intermittent sources connected to the same grid, thus providing a more

realistic representation of microgrid operation.

7.4 Concluding Remarks

Overall, extending the present work to address grid disturbances, explore alternative control strategies, and integrate realistic renewable energy sources represents a logical and meaningful progression of the study. These directions would provide a more complete understanding of inverter-dominated microgrids and contribute to the development of control schemes capable of maintaining stable and reliable operation under real-world conditions.

Bibliography

[1] https://www.iea.org/news/growth-in-global-electricity-demand-is-set-to-accelerate [Accessed 30-09-2025].

[2] Energy for Africa — commission.europa.eu. https://commission.europa.eu/topics/international-partnerships/global-gateway/energy-africa_en?utm_source=dailybrief&utm_content=20250929&utm_medium=email&utm_campaign=DailyNewsBrief2025Sept29&utm_term=DailyNewsBrief. [Accessed 30-09-2025].

[3] World Bank Open Data — data.worldbank.org. https://data.worldbank.org/indicator/EG.ELC.ACCS.ZS?locations=GH. [Accessed 30-09-2025].

[4] Energy Commission of Ghana. National energy statistics 2024, 2024.

[5] Global Legal Insights. Energy laws and regulations – ghana. https://www.globallegalinsights.com/practice-areas/energy-laws-and-regulations/ghana/, 2024. Accessed 1 October 2025.

[6] Africa Centre for Energy Policy. From generation to distribution: Investigating ghana's power sector's value chain and its implications for reliable, affordable and clean energy supply. https://acep.africa, 2024. Accessed 1 October 2025.

[7] MyJoyOnline. Minority cites 500mw deficit, warns of return of load shedding. https://www.myjoyonline.com, 2024. Accessed 1 October 2025.

[8] GBC Ghana Online. Energy minister john jinapor reports 700mw deficit. https://www.gbcghanaonline.com, 2025. Accessed 1 October 2025.

[9] GWL &x2013; Welcome &x2013; World Class Utility Company — gwcl.com.gh. https://www.gwcl.com.gh/. [Accessed 30-09-2025].

[10] Ghana Grid Company Limited (GRIDCo). System disturbance affecting the regions of the north (press statement). Press Statement, February 2024. Accessed: Sep. 30, 2025.

[11] Ghana Grid Company Limited (GRIDCo). System disturbance (press statement). Press Statement, March 2024. Accessed: Sep. 30, 2025.

[12] Ghana Grid Company Limited (GRIDCo) and Electricity Company of Ghana (ECG). Power supply issues: Gas challenge from nigeria (joint press statement). Joint Press Statement, June 2024. Accessed: Sep. 30, 2025.

[13] Africa Centre for Energy Policy (ACEP). From generation to distribution: Investigating ghana's power sector's value chain and its implications for reliable, affordable, and clean energy supply. Technical report, Africa Centre for Energy Policy (ACEP), 2024. Accessed: Sep. 30, 2025.

[14] IEEE Standards Association. Ieee recommended practice for monitoring electric power quality (ieee std 1159-2019), 2019. Accessed: Sep. 30, 2025.

[15] Xiongfei Wang and Frede Blaabjerg. Harmonic stability in power electronic-based power systems: Concept, modeling, and analysis. *IEEE Transactions on Power Electronics*, 31(4):3071–3084, 2015. Accessed: Sep. 30, 2025.

[16] International Electrotechnical Commission (IEC). Iec 61000-4-11/-34: Voltage dips, short interruptions and voltage variations immunity tests, 2017. Accessed: Sep. 30, 2025.

[17] Amirnaser Yazdani and Reza Iravani. *Voltage-Sourced Converters in Power Systems: Modeling, Control, and Applications*. Wiley-IEEE Press, 2010. Accessed: Sep. 30, 2025.

[18] B. Kroposki, B. Johnson, Y. Zhang, V. Gevorgian, P. Denholm, B. Hodge, and M. H. Adkins. Achieving a 100% renewable grid. *IEEE Power & Energy Magazine*, 15(2):61–73, 2017. Accessed: Sep. 30, 2025.

[19] IEEE Standards Association. Ieee std c37.102 and ieee std c57.12 series: Protection and transformer over-fluxing guidance, 2018. Accessed: Sep. 30, 2025.

[20] Qing-Chang Zhong and Georg Weiss. Synchronverters: Inverters that mimic synchronous generators. *IEEE Transactions on Industrial Electronics*, 58(4):1259–1267, 2011. Accessed: Sep. 30, 2025.

[21] Iec 60034-1: Rotating electrical machines – rating and performance, 2022.

[22] Iec 60034-26: Rotating electrical machines – effects of unbalanced voltages on the performance of three-phase cage induction motors, 2019.

[23] Iec 61800-5-1: Adjustable speed electrical power drive systems – part 5-1: Safety requirements – electrical, thermal and energy, 2016.

[24] Iec 61800-2: Adjustable speed electrical power drive systems – part 2: General requirements – rating specifications, 2015.

[25] World Health Organization (WHO). Water safety plans: Managing drinking-water quality from catchment to consumer. Guidelines, latest edition, 2023. Accessed: Sep. 30, 2025.

[26] American Water Works Association (AWWA). *M19: Emergency Planning for Water Utilities*. American Water Works Association, latest edition edition, 2022. Accessed: Sep. 30, 2025.

[27] IEEE Standards Association. Ieee recommended practice for the design of reliable industrial and commercial power systems (ieee std 493-2007, gold book), 2007. Accessed: Sep. 30, 2025.

[28] European Committee for Electrotechnical Standardization (CENELEC). En 50160: Voltage characteristics of electricity supplied by public distribution systems, 2019. Accessed: Sep. 30, 2025.

[29] Microgrid Overview. https://www.energy.gov/sites/default/files/2024-02/46060_DOE_GDO_Microgrid_Overview_Fact_Sheet_RELEASE_508.pdf. [Accessed 27-09-2025].

[30] Ebenezer Nyarko Kumi. The Electricity Situation in Ghana: Challenges and Opportunities. https://www.cgdev.org/sites/default/files/electricity-situation-ghana-challenges-and-opportunities.pdf. [Accessed 27-09-2025].

[31] Development of new reliability metrics for microgrids: Integrating renewable energy sources and battery energy storage system — sciencedirect.com. https://www.sciencedirect.com/science/article/pii/S2352484723012763. [Accessed 28-09-2025].

[32] Optimal sizing of battery energy storage systems and reliability analysis under diverse regulatory frameworks in microgrids — sciencedirect.com. https://www.sciencedirect.com/science/article/pii/S2211467X23002055. [Accessed 28-09-2025].

[33] Techno-economic analysis of a microgrid design for a commercial health facility in Ghana- Case study of Zipline Sefwi-Wiawso — sciencedirect.com. https://www.sciencedirect.com/science/article/pii/S246822762300011X. [Accessed 28-09-2025].

[34] How microgrids can facilitate energy access and electrify rural Africa — theigc.org. https://www.theigc.org/blogs/climate-priorities-developing-countries/how-microgrids-can-facilitate-energy-access-and. [Accessed 28-09-2025].

[35] Stochastic Operation of Energy Constrained Microgrids Considering Battery Degradation — arxiv.org. https://arxiv.org/abs/2111.03313. [Accessed 28-09-2025].

[36] A Multi-timescale Two-stage Robust Grid-friendly Dispatch Model for Microgrid Operation — arxiv.org. https://arxiv.org/abs/1912.06587. [Accessed 28-09-2025].

[37] Integrating Renewable Energy with Grid Stability: Challenges and Solutions. https://episensor.com/knowledge-base/integrating-renewable-energy-with-grid-stability-challenges-and-solutions/. [Accessed 28-09-2025].

[38] Funding Microgrids: CAPEX versus OPEX. https://www.microgridknowledge.com/resources/microgrid-perspectives/article/11429006/funding-microgrids-capex-versus-opex. [Accessed 28-09-2025].

[39] Ryley Baird. Microgrids: Pioneering the Path to Energy Independence in the UK. https://www.dbsne.com/post/microgrids-pioneering-the-path-to-energy-independence-in-the-uk. [Accessed 28-09-2025].

[40] Josep M. Guerrero, Juan C. Vasquez, Jose Matas, Luis G. de Vicuña, and Miguel Castilla. Hierarchical control of droop-controlled ac and dc microgrids – a general approach toward standardization. *IEEE Transactions on Industrial Electronics*, 58(1):158–172, 2011. Accessed: Sep. 30, 2025.

[41] Renewable capacity statistics 2025 — irena.org. https://www.irena.org/Publications/2025/Mar/Renewable-capacity-statistics-2025. [Accessed 11-12-2025].

[42] Jrc photovoltaic geographical information system (pvgis) - european commission — re.jrc.ec.europa.eu. https://re.jrc.ec.europa.eu/pvg_tools/en/. [Accessed 18-12-2025].

[43] Historical Forecast API — Open-Meteo.com — open-meteo.com. https://open-meteo.com/en/docs/historical-forecast-api?start_date=2024-01-01&end_date=2024-01-31&hourly=wind_speed_80m,wind_speed_120m&timezone=GMT&latitude=6.25&longitude=-0.1167&wind_speed_unit=ms. [Accessed 12-11-2025].

[44] Cost Projections for Utility-Scale Battery Storage: 2025 Update — research-hub.nrel.gov. https://research-hub.nrel.gov/en/publications/cost-projections-for-utility-scale-battery-storage-2025-update/. [Accessed 17-11-2025].

[45] U.S. Utility-Scale Solar, 2025 Data Update — Energy Markets & Policy — emp.lbl.gov. https://emp.lbl.gov/utility-scale-solar. [Accessed 17-11-2025].

[46] Land-Based Wind Market Report: 2024 Edition — Energy Markets & Policy — emp.lbl.gov. https://emp.lbl.gov/publications/land-based-wind-market-report-2024. [Accessed 17-11-2025].

[47] S. D. Sudhoff P. C. Krause, O. Wasynczuk. Analysis of electric machinery and drive systems. https://onlinelibrary.wiley.com/doi/book/10.1002/9780470179634, 2013. [Accessed 17-11-2025].

[48] P. Rodríguez R. Teodorescu, M. Liserre. Grid converters for photovoltaic and wind power systems. https://onlinelibrary.wiley.com/doi/book/10.1002/9780470667056, 2011. [Accessed 17-11-2025].

[49] Clarke transform - implement ab to transformation - simulink. https://https://se.mathworks.com/help/mcb/ref/clarketransform.html. [Accessed 2025-11-19].

[50] Park Transform. https://se.mathworks.com/help/mcb/ref/parktransform.html. [Accessed 19-11-2025].

[51] D. Maksimović R. W. Erickson. Fundamentals of power electronics. https://link.springer.com/book/10.1007/978-1-4757-0554-5, 2001. [Accessed 17-11-2025].

[52] Control of VSC-based HVDC Transmission System for Offshore Wind Power Plants. https://projekter.aau.dk/projekter/files/32291553/Control%20of%20VSC-based%20HVDC%20Transmission%20for%20Offshore%20WPPs.pdf, 2010. [Accessed 19-11-2025].

[53] P. Kundur. Power system stability and control. https://ieeexplore.ieee.org/book/5269951, 1994. [Accessed 17-11-2025].

[54] W. P. Robbins N. Mohan, T. M. Undeland. Power electronics: converters, applications, and design. https://onlinelibrary.wiley.com/doi/book/10.1002/9780470543558, 2003. [Accessed 17-11-2025].

[55] T. A. Lipo D. G. Holmes. Pulse width modulation for power converters. https://onlinelibrary.wiley.com/doi/book/10.1002/9780470546283, 2003. [Accessed 17-11-2025].

[56] S. Hansen M. Liserre, F. Blaabjerg. Design and control of an lcl filter for three-phase active rectifiers. https://ieeexplore.ieee.org/document/963838, 2001. [Accessed 17-11-2025].

[57] IEEE Standards Association. Ieee standard 1547-2018 for interconnection of distributed energy resources. https://standards.ieee.org/standard/1547-2018.html, 2018. [Accessed 17-11-2025].

[58] Transitproject.eu. Modeling and Control of Grid Following Inverters for Renewables. https://transitproject.eu/wp-content/uploads/2025/03/UCY_Modelling-and-Control-of-Grid-Following-Inverter-for-Renewables.pdf. [Accessed 20-11-2025].

[59] R. Iravani A. Yazdani. Voltage-sourced converters in power systems. https://ieeexplore.ieee.org/book/6267439, 2010. [Accessed 17-11-2025].

[60] Ian Collins. Phase-Locked Loop (PLL) Fundamentals. https://www.analog.com/en/resources/analog-dialogue/articles/phase-locked-loop-pll-fundamentals.html. [Accessed 19-11-2025].

[61] M. Karimi-Ghartemani. Phase-locked loops and synchronization methods for power electronics. https://onlinelibrary.wiley.com/doi/book/10.1002/9781119316988, 2014. [Accessed 17-11-2025].

A Appendix A

A.1 Load profile overview

For the load profile presented in Figure 2.1, the operating schedule of equipment at the Bukunor Water Treatment Plant (B-WTP) was analyzed over 24 hours under ideal running conditions. Each piece of equipment on the WTP is represented by its rated power and operating status, with active periods shown in green, as indicated in the key. The purpose of this schedule is to establish an accurate representation of the plant's daily instantaneous power demand and to identify the periods of high demand and low energy usage.

The information in Figure A.1 serves as the basis for sizing and evaluating the hybrid renewable energy system, ensuring that the model reflects the plant's actual operational characteristics. Observation of the load pattern indicates that energy demand varies significantly between daytime and nighttime, corresponding to periods of high pumping and treatment activity. The derived total instantaneous power requirement at each hour serves as the reference for determining the appropriate capacities of the solar PV, wind, and battery energy storage subsystems in subsequent analyses.

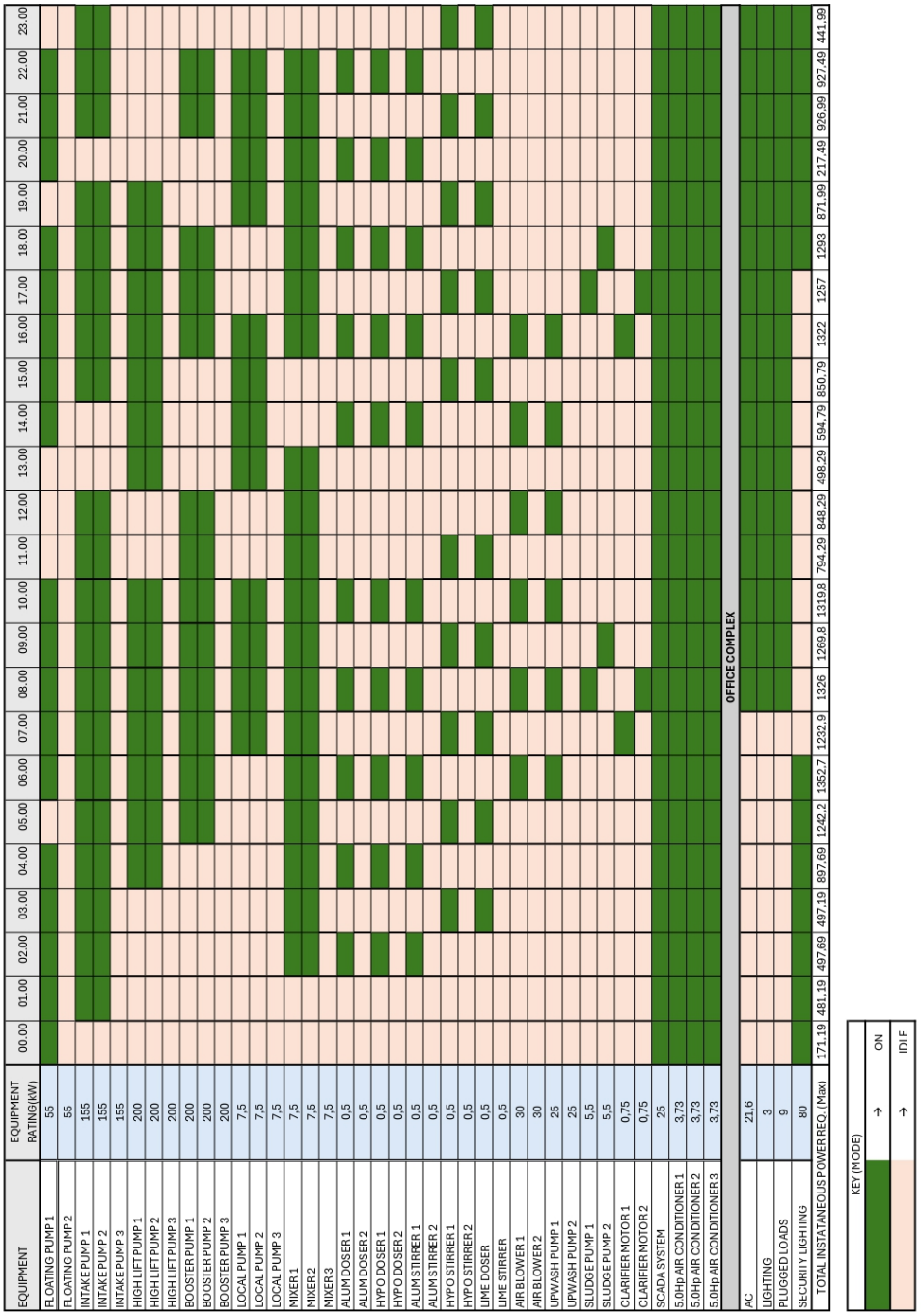

Figure A.1. Detailed Load schedule of the Bukunor Water Treatment Plant under ideal running conditions.